NUMERICAL ANALYSIS OF PLANE CRACKS

IN STRAIN-GRADIENT ELASTIC MATERIALS

By

SREEKANTH AKARAPU

A thesis submitted in partial fulfillment of
the requirements for the degree of

MASTER OF SCIENCE

WASHINGTON STATE UNIVERSITY
Department of Mechanical and Materials Engineering

DECEMBER 2005

To the Faculty of Washington State University:

The members of the Committee appointed to examine the thesis of SREEKANTH AKARAPU find it satisfactory and recommend that it be accepted.

_____
Chair

_____

_____

ACKNOWLEDGMENTS

NUMERICAL ANALYSIS OF PLANE CRACKS IN

STRAIN-GRADIENT ELASTIC MATERIALS

Abstract

by Sreekanth Akarapu , M.S.
Washington State University
December 2005

Chair: Hussein. M. Zbib

The classical linear elastic fracture mechanics is not valid near the crack tip because of the unrealistic singular stress at the tip. The study of the physical nature of the deformation around the crack tip reveals the dominance of long-range atomic interactive forces. Unlike the classical theory which incorporates only short range forces, a higher-order continuum theory which could predict the effect of long range interactions at a macro scale would be appropriate to understand the deformation around the crack tip. A simplified theory of gradient elasticity proposed by Aifantis is one such grade-2 theory. This theory is used in the present work to numerically analyze plane cracks in strain-gradient elastic materials. Towards this end, a 36 DOF C^1 finite element is used to discretise the displacement field. The results show that the crack tip singularity still persists but with a different nature which is physically more reasonable. A smooth closure of the structure of the crack tip is also achieved.

LIST OF FIGURES

TABLE OF CONTENTS

CHAPTER 1

INTRODUCTION

A thorough understanding of the deformation at and around the crack tip is very important to gain an insight into issues like crack nucleation and crack growth. Fracture mechanics developed based on classical linear elasticity is not valid near the crack tip because of the unrealistic singular solutions at the crack tip. Many researchers have devoted a lot of effort towards resolving the crack tip singularity. The reasons why linear elasticity is not appropriate to use in the study of near crack tip behavior and various efforts made by researchers to modify linear elasticity to predict the behavior of cracks are discussed below.

In general, the opening of crack faces is very much small compared to the longitudinal dimensions. Therefore, cracks are considered as surfaces of discontinuity of displacement vector. Cracks having discontinuous normal displacement component are Mode I type and the ones having in-plane tangential component and out-of-plane component are Mode II and Mode III type respectively.

The physical nature of the deformation in the neighborhood of displacement discontinuities in an elastic continuum is different from the rest of the continuum. A comparison is made between the deformation of a crack neighborhood and a cavity neighborhood in an elastic continuum to understand the peculiarity. Upon slight variation of applied load, the variation in shape of crack and cavity is studied [1]. The crack changes shape by an appreciable amount when subjected to even small changes in loads

unlike the very small change of the boundary of a cavity. This violates one of the basic assumptions of classical linear elasticity of smallness of changes in the boundaries which permits to satisfy the boundary conditions at the surface of the unstrained body. Therefore, the classical differential equations of equilibrium and boundary conditions of the theory of linear elasticity cannot in principle solve this problem without the introduction of appropriate additional modifications. The various efforts towards modifying these equations by many researchers are briefly discussed below.

The opposite faces of crack at the tip are so close together that large force of atomic attractions prevails. Barenblatt [1], in his mathematical theory of equilibrium cracks, took the forces of cohesion acting on the crack faces into account along with the applied external loads. The forces of cohesion alone give singular compressive stresses at the crack tip (with no remote tension applied) and the tension alone with traction free crack faces give a singular tensile stresses at the crack tip. The possibility of one canceling with the other, gives rise to a non-singular solution at the crack tip. Goodier and Kanninen [2] used non-linear springs at the extremities of crack to model the locally non-linear behavior of the crack. Atomic lattice models (Gehlen and Kanninen [3], Weiner and sanders [4]) are also used to study the deformation around the crack.

The peculiar non-linearity in the neighborhood of the crack tip can also be interpreted as dominance of micro-structural effects and long-range forces of interaction. The other limitations of classical theory of elasticity can be attributed to local nature of the theory which is based on only nearest neighbor interactions which in turn bereaves it from

having a characteristic length scale. An alternate way of tackling this problem is to employ a continuum theory which could include long-range atomic interactive forces at a macro scale. The effect of long-range atomic interactions is incorporated to an acceptable extent by introducing a characteristic length scale into the continuum theory. Non-local elasticity proposed by Eringen [5] includes a characteristic length and remarkably enough eliminates stress singularity at the crack tip. Apart from non-local elasticity, higher-order strain gradient continuum theories predict the effect of long-range atomic interactions to a great extent by introducing a length scale. The theory of non-local elasticity and higher-order continuum theories like cosserat couple stress theory, Mindlin's theory and gradient elasticity are discussed in the following paragraphs.

The distinction between the local continuum theories and non-local continuum theories can be understood by deriving the local balance laws from the global statements. The classical balance laws consist of the balance of mass, momentum, moment of momentum and energy. To explicate the difference, only the balance law of mass is considered. The global statement of conservation of mass is

$$\frac{D}{Dt} \int_v \rho dv = 0 \qquad \qquad \text{---------- (1.1)}$$

where the operator D/Dt denotes the material time derivate and ρ denotes the mass density. In local continuum mechanics, this integral statement is assumed to be valid not only for the whole body but also at all points of the body which turns an integral

statement to a differential statement. In non-local theory, the validation of the integral

statement is relaxed a bit by assuming it to be valid only for the whole body. This is key

conceptual difference between local and non-local theories. As seen from physical

perspective, this is equivalent to including non-local interactions and as a result long

range interactions. The local statement of conservation of mass in the non-local theory[5]

is

$$\frac{D}{Dt}(\rho dv) = \hat{\rho} dv \qquad \text{-------- (1.2)}$$

where $\hat{\rho}$ is the localization residual which takes into account of the local mass

production and destruction contributing nothing globally. The introduction of localization

residuals is idiosyncratic to non-local theories. The non-local theory of elasticity

proposed by Eringen and co-workers [5] is employed to regularize the crack-tip

singularity to remarkable extent. He proposed that stress at a point is not only dependent

on the strain at that point alone (which is local) but also on all the points in the whole

body. Therefore, the constitutive equations are in the form of an integral equation over

the volume.

$$t_{kl}(x) = \int_v \left[\lambda'(|x - x'|)\varepsilon_{rr}(x')\delta_{kl} + 2\mu'(|x - x'|)\varepsilon_{kl}(x') \right] dv(x') \qquad \text{------------ (1.3)}$$

Where,

$t_{kl}(x)$ is stress at a point x

4

$\varepsilon_{kl}(x')$ are strains at all points in the volume V

λ' and μ' are the non-local modulii which are functions of the distance $|x - x'|$ between the reference point x and any other point x'.

This non-local theory results in a finite stress solution at the crack tip but it is not clear whether the satisfaction of stress-free boundary is ensured at the crack tip and whether the strain distribution remains finite at the tip. The definition of the non-local integral on the external boundary is also not clear [11].

An alternate way of tackling this problem is to employ higher-order continuum theories which could manifest the micro-structural effects at the macroscale. Higher-order continuum theories are developed by incorporating higher-order spatial gradients of strain or displacement into the strain energy density function. Depending on the order of spatial gradient, these theories are classified as grade-n theories. It has been shown that higher-order continuum theories which have an intrinsic characteristic length can incorporate nearest and next nearest neighbor interactions. These generalized continuum theories are developed by various researchers differing by the various degrees of refinement of kinematical description of the continuum with microstructure. An excellent compilation of literature on higher-order continuum theory can be found in the first and third chapter of [6].

In the early sixties, E & F cosserat [7] developed couple stress theory which is one of the first attempts to include a characteristic length scale into the continuum theory. The

cosserat couple stress theory is taken as a motivation to develop physically meaningful and computationally simple theories. One of such theories is the strain gradient theory developed by Mindlin [9]. Gradient elasticity, proposed by Aifantis [11], which is used in the present work, can be derived as a special case of Mindlin's theory. In the following paragraphs, first, the couple stress theory is discussed along with its limitations; secondly, Mindlin's theory is discussed briefly about how some of the limitations of couple stress theory are avoided; and thirdly Aifantis gradient elasticity is presented as a computationally simple theory compared to Mindlin's theory.

Cosseart couple stress theory is based on the assumption that there exists a strain energy density function which is a function of strain as well as rotational gradients. The work conjugates of strain and rotational gradients are stress and couple stress respectively.

The introduction of a new kinematic variable, which is rotational gradient, demanded for an extra modulus connecting couple stress with the rotational gradients. This bending-twisting modulus has a dimension of force and it is through this modulus the characteristic length is introduced into the couple stress theory. The length scale is adopted as the square root of ratio of bending-twisting modulus to shear modulus. The Couple stress theory is also employed to solve for stresses at the crack tip, however, stress singularity persisted (Sternberg and Muki) [8]. The introduction of couple stress made the force stress tensor asymmetric which made the computational implementation difficult.

Mindlin's [9] work on microstructure in linear elasticity is the most pertinent and notable which introduced the idea of unit cell to account for the micro-medium in a continuum. A restricted version of this Mindlin continuum is deduced by making the material micro-homogeneous resulting in a strain energy density function depending on macroscopic strain and strain gradient. In his paper with Eshel [10], the first order strain gradient theory is dealt in detail and all the three possible forms are explored. The three forms are distinguished based on the different groupings of the eighteen components of the additional variable, apart from strain, of the strain energy density function: I, eighteen components of second gradient of displacement gradient; II, eighteen components of strain gradient; III, eight components of rotation gradient and ten components of fully symmetric part of second gradient of displacement or strain gradient. All the three forms lead to the same displacement equations of motion and same traction boundary conditions. But the most noteworthy difference among the three forms is the symmetry of the total stress, which is symmetric only in form II. This symmetry of total stress avoids the problem of non-symmetric stress tensor in cosserat couple stress theory.

Mindlin developed the strain gradient theory for an isotropic material in the most general form which introduced 5 more material constants in addition to the classical elastic constants whose determination is formidable experimental challenge. The computational implementation of Mindlin's theory is very complex. Motivated by the ability of the theory to exhibit the microstructural effects at the macroscale and towards an attempt to reduce the material constants and reduce the computational complexities, Aifantis [11] proposed the gradient elasticity with only one material constant. This simplified theory is

employed in the present work. Before going further, it is worth noting that a correlation between the strain gradient elasticity and the lattice model of a crystal with nearest and next nearest neighbor interactions has been shown (see R.A. Toupin & D.C. Gazis [12]).

The main objectives of this work are to 1) regularize the stress singularities at the crack tip by solving Griffith's problem using the special theory of gradient elasticity proposed by Aifantis, 2) stress analyze the bi-material interface cracks 3) stress analyze the problem of a crack normal to the bi-material interface and 100 microns away from it using this theory.

The thesis is organized as follows: In Chapter 2, theory of gradient elasticity proposed by Aifantis [11] is derived as a special case of Mindlin's [10] form II of his first order strain gradient theories. The moment equilibrium equations are derived which exhibits the symmetry of the total stress tensor. The uniqueness theorem of the boundary value problem of gradient elasticity is presented. The formulations of this theory from the explicit and implicit definitions of non-local strain in terms of local strain are also discussed. In Chapter 3, Finite element formulation of gradient elasticity is discussed. In Chapter 4, results are presented and are discussed in Chapter 5. The thesis is concluded in the final chapter followed by references and appendix.

CHAPTER 2

GRADIENT ELASTICITY FORMULATIONS

Mindlin's [9] work on first order gradient theories is most noteworthy in his effort to manifest the microstructural effects at a macroscale. In his work, he presented in detail all the three possible forms of strain energy density for a grade-2 theory. Unlike the classical linear elasticity, the grade-2 theories are based on an assumption that strain energy density function is dependent not only on six components of strain but also on the eighteen components of strain gradient. He classified the three forms on the basis of different groupings of the eighteen additional arguments of strain energy density function. The strain energy density function having the additional eighteen arguments
Form I: as second gradient of displacement, Form II: as strain gradient and Form III: eight components of rotation gradient and ten components of fully symmetric part of second gradient of displacement or strain gradient. In particular, gradient elasticity which is employed in the present work can be shown as a special case of Form II of Mindlin's theory. In the following paragraphs, Mindlin's theory is discussed and shown how Aifantis theory is a special case.

The grade-2 theory of elasticity is based on an assumption that there exists a strain energy density function which depends not only on six components strain but also on additional eighteen components of strain gradient.

$$W = W(\varepsilon_{ij}, \varepsilon_{ij,k}) \qquad \text{------ (2.1)}$$

where ε_{ij} is symmetric part of displacement field

$$\varepsilon_{ij} = \frac{1}{2}\left(u_{i,j} + u_{j,i}\right) \qquad \text{------ (2.2)}$$

where u_i denotes the component of displacement vector and the indices following the comma denote partial derivatives with respect to the spatial coordinates.

2.1 **Variational equations of motion**:

According to the principle of virtual work, variation of strain energy i.e; internal work is equal to the variation of work done by the external forces i.e; external work.

$$\delta W_I = \delta W_E \qquad \text{-------- (2.3)}$$

where $W_I = \int_V W dv$ and W_E is the work done by the external forces.

For the variation of strain energy, the work conjugates of strain and strain gradient are defined as follows:

$$\sigma_{ij} = \frac{\partial W}{\partial \varepsilon_{ij}} = \sigma_{ji} \qquad \text{------------- (2.4a)}$$

$$\mu_{kji} = \frac{\partial W}{\partial \varepsilon_{ij,k}} = \mu_{kij} \qquad \text{------- (2.4b)}$$

where σ_{ij} , Cauchy stress, is the work conjugate of strain. The first index denotes the plane on which it is acting and the second index denotes the direction of action. μ_{kji} , double stress, is the work conjugate of strain gradient. The first index denotes the plane on which double stress is acting, second index denotes the direction of lever arm and the third index denotes the direction of action. The double stress can be easily appreciated with the help of Fig. 1.

$$\hat{\mu}_{112} \Leftrightarrow u_{2,11}$$

$$\hat{\mu}_{121} \Leftrightarrow u_{1,21}$$

$$\tfrac{1}{2}\left(\hat{\mu}_{112} + \hat{\mu}_{121}\right) \Leftrightarrow \tfrac{1}{2}\left(u_{2,11} + u_{1,21}\right)$$

$$\mu_{121} \Leftrightarrow \varepsilon_{12,1}$$

X_2

X_1
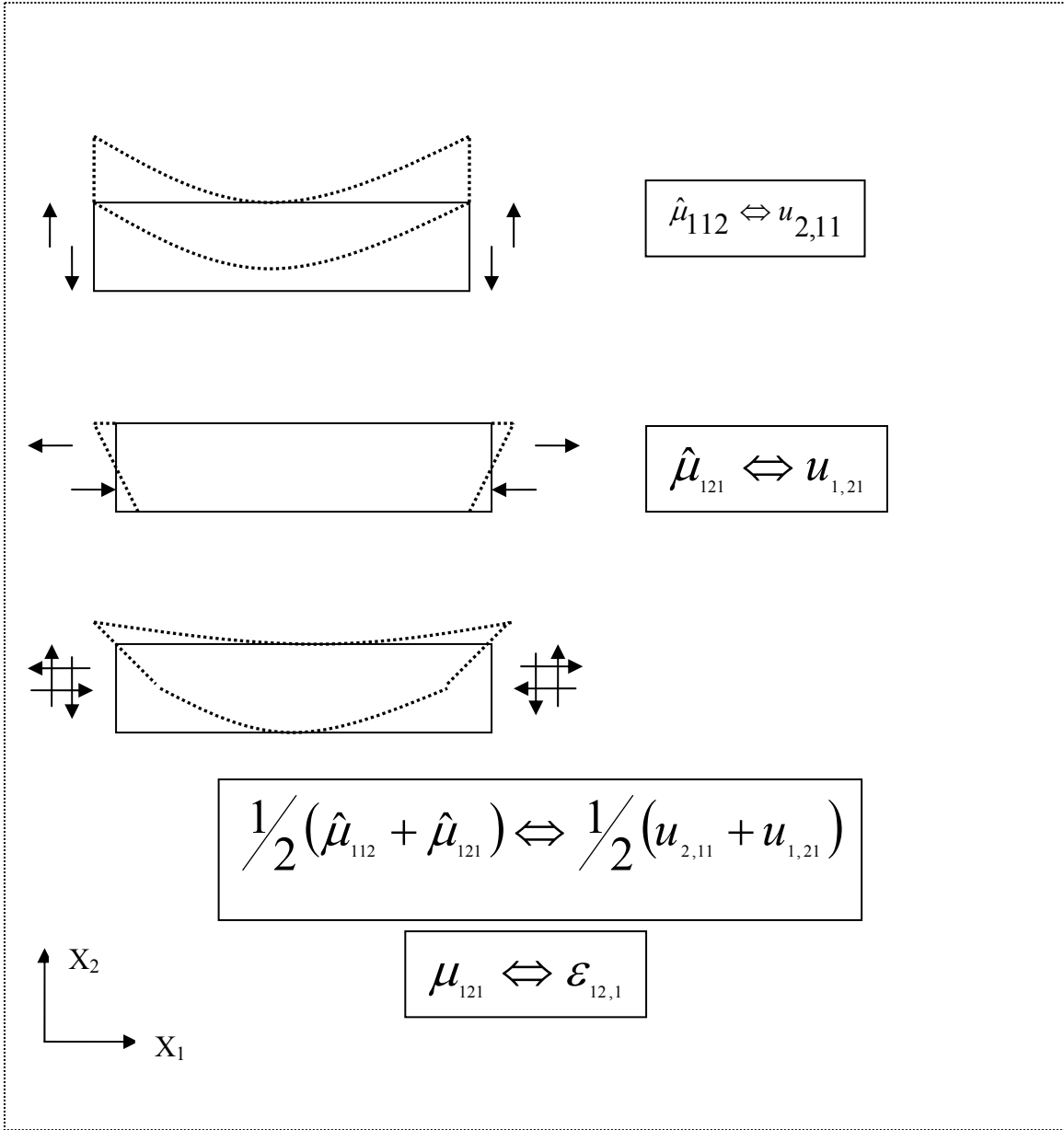
Fig 1: This Fig. is a pictorial representation of one component of double stress. The $\Leftrightarrow$ sign reads as "work conjugate of". As it can be noticed from the figure, double stress is self-equilibrating with no net moment and no net force [9]. The solid line represents the undeformed and dashed line represents the deformed shape.

The variation of strain energy density is

$$\delta W = \frac{\partial W}{\partial \varepsilon_{ij}} \delta \varepsilon_{ij} + \frac{\partial W}{\partial \varepsilon_{ij,k}} \delta \varepsilon_{ij,k}$$

$$= \sigma_{ji} \delta \varepsilon_{ij} + \mu_{kji} \delta \varepsilon_{ij,k} \qquad \text{---------------- (2.5)}$$

Using the definition of strain as the symmetric part of displacement gradient, the above equation can be expressed as

$$\delta W = \sigma_{ji} \left(\delta u_{i,j} - \delta \omega_{ij} \right) + \mu_{kji} \left(\delta u_{i,jk} - \delta \omega_{ij,k} \right) \qquad \text{---------------- (2.6)}$$

As σ_{ji} is symmetric and μ_{kji} is symmetric in indices i and j, we obtain

$$\delta W = \sigma_{ji} \delta u_{i,j} + \mu_{kji} \delta u_{i,jk}$$

$$= \left[\left(\sigma_{ji} \delta u_i \right)_{,j} - \sigma_{ji,j} \delta u_i \right] + \left[\left(\mu_{kji} \delta u_{i,j} \right)_{,k} - \mu_{kji,k} \delta u_{i,j} \right]$$

$$= \left[\left(\sigma_{ji} \delta u_i \right)_{,j} - \sigma_{ji,j} \delta u_i \right] +$$

$$\left[\left(\mu_{kji} \delta u_{i,j} \right)_{,k} - \left(\mu_{kji,k} \delta u_i \right)_{,j} + \mu_{kji,kj} \delta u_i \right]$$

$$\delta W = \left[\left(\sigma_{ji} - \mu_{kji,k}\right)\delta u_i\right]_{,j} - \left(\sigma_{ji,j} - \mu_{kji,kj}\right)\delta u_i + \left(\mu_{kji}\delta u_{i,j}\right)_{,k} \qquad \text{----------- (2.7)}$$

Therefore, the variation of the total strain energy is

$$\delta W_I = \int_V \delta W \, dV \qquad \text{------------ (2.8)}$$

Applying divergence theorem to equation (2.8), we obtain

$$\delta W_I = \int_S n_j \left(\sigma_{ji} - \mu_{kji,k}\right)\delta u_i \, dS - \int_V \left(\sigma_{ji,j} - \mu_{kji,kj}\right)\delta u_i \, dV$$

$$+ \int_S n_k \mu_{kji}\delta u_{i,j} \, dS \qquad \text{------------ (2.9)}$$

In the last surface integral, the variation of $u_{i,j}$ is not independent of variation of u_i on the surface. As the variation normal derivative of displacement $n_j u_{i,j}$ is independent of variation of displacement u_i on the surface, $u_{i,j}$ in the last integral can be resolved on the boundary into surface gradient and a normal gradient as follows:

$$n_k \mu_{kji}\delta u_{i,j} = n_k \mu_{kji} D_j \delta u_i + n_k \mu_{kji} n_j D \delta u_i \qquad \text{----------- (2.10)}$$

where the operators D_j and D are defined as follows:

14

$$D_j \equiv \left(\delta_{jl} - n_j n_l \right) \partial_l \ , \qquad D \equiv n_l \partial_l \qquad\qquad \text{------------ (2.11)}$$

with δ_{jl} being the kroneker delta and ∂_l denotes the spatial partial derivative with respect to the subscript.

The first term on the right hand side of equation (2.10) contains the non-independent variation $D_j \delta u_i$ which can further be expressed as [using the product rule of differentiation (d(u) = d(uv)-d(v))]

$$n_k \mu_{kji} D_j \delta u_i = D_j (n_k \mu_{kji} \delta u_i) - D_j (n_k \mu_{kji}) \delta u_i \qquad\qquad \text{--------- (2.12)}$$

The last term in the above equation (2.12) now contains the independent variation of δu_i.

Using surface divergence theorem, the first term of the equation (2.12) can be written as:

$$D_j (n_k \mu_{kji} \delta u_i) = (D_l n_l) n_j n_k \mu_{kji} \delta u_i \qquad\qquad \text{---------- (2.13)}$$

Assembling all the results from (2.9) to (2.13), equation (2.8) can be written as

$$\delta W_I = \int_S \left[n_j \left(\sigma_{ji} - \mu_{kji,k} \right) - D_j (n_k \mu_{kji}) + (D_l n_l) n_j n_k \mu_{kji} \right] \delta u_i dS$$

$$- \int_V \left[\left(\sigma_{ji,j} - \mu_{kji,kj} \right) \right] \delta u_i dV + \int_S n_k \mu_{kji} n_j D \delta u_i dS$$

$$\text{------------ (2.14)}$$

The variation of work done by the external forces, neglecting the body forces, is

15

$$\delta W_E = \int_S t_i \delta u_i dS + \int_S \tau_i D\delta u_i dS \qquad \text{------------- (2.15)}$$

where t_i and τ_i are traction and double traction applied on the surface respectively.

For any independent variations of u_i and $D\delta u_i$, the principle of virtual work (equation 2.3) results in following stress-equilibrium equations and boundary conditions:

$$\sigma_{ji,j} - \mu_{kji,kj} = 0 \qquad \text{Equilibrium equations} \qquad \text{--------------- (2.16)}$$

Defining

$$\tilde{\sigma}_{ji} = \sigma_{ji} - \mu_{kji,k} \qquad \text{--------------- (2.17)}$$

Equilibrium equations (2.16) becomes

$$\tilde{\sigma}_{ji,j} = 0 \qquad \text{---------------- (2.18)}$$

and boundary conditions are

$$t_i = n_j(\sigma_{ji} - \mu_{kji,k}) - D_j(n_k \mu_{kji}) + (D_l n_l)n_j n_k \mu_{kji} \qquad \text{--------- (2.19)}$$

$$\tau_i = n_j n_k \mu_{kji}$$ ------------- (2.20)

2.2) Constitutive equations:

In Mindlin's work, the strain energy density function is expressed as a function of ε_{ij} and $\varepsilon_{ij,k}$ in the most general form for a linear, isotropic gradient-dependent elastic material as:

$$\widetilde{W} = \frac{1}{2}\lambda\varepsilon_{ii}\varepsilon_{jj} + \mu\varepsilon_{ij}\varepsilon_{ij} + c_1\varepsilon_{ij,k}\varepsilon_{ik,k} + c_2\varepsilon_{ii,k}\varepsilon_{kj,j} + c_3\varepsilon_{ii,k}\varepsilon_{jj,k}$$

$$+ c_4\varepsilon_{ij,k}\varepsilon_{ij,k} + c_5\varepsilon_{ij,k}\varepsilon_{kj,i}$$ ------------ (2.21)

For the special form of gradient elasticity proposed by Aifantis, it is assumed that c_3 and c_4 are the only non-vanishing gradient coefficients. More explicitly, the strain energy density function is taken as [11]:

$$W = \frac{1}{2}\lambda\varepsilon_{ii}\varepsilon_{jj} + \mu\varepsilon_{ij}\varepsilon_{ij} + l^2\left(\frac{1}{2}\lambda\varepsilon_{ii,k}\varepsilon_{jj,k} + \mu\varepsilon_{ij,k}\varepsilon_{ij,k}\right)$$ ------ (2.22)

Using the definitions of work conjugates of strain and strain gradient from equation (2.4) with equation (2.22) as the strain energy density function, we have

$$\sigma_{ij} = \frac{\partial W}{\partial \varepsilon_{ij}} = \lambda \varepsilon_{pp} \delta_{ij} + 2\mu \varepsilon_{ij} \qquad \text{------------------ (2.23)}$$

$$\mu_{kji} = \frac{\partial W}{\partial \varepsilon_{ij,k}} = l^2 \left(\lambda \varepsilon_{pp} \delta_{ij} + 2\mu \varepsilon_{ij} \right)_{,k} \qquad \text{------------------ (2.24)}$$

Using equations (2.23)-(2.24) in equation (2.17),

$$\tilde{\sigma}_{ji} = \lambda \varepsilon_{pp} \delta_{ji} + 2\mu \varepsilon_{ji} - l^2 \left(\lambda \varepsilon_{pp} \delta_{ji} + 2\mu \varepsilon_{ji} \right)_{,kk} \qquad \text{------------------ (2.25)}$$

The above equation is the constitutive relation for the gradient elasticity proposed by Aifantis. The non-classical parameter l has the dimensions of length. This characteristic length is attributed to the micro structure of the material.

A boundary value problem can be formulated in terms of solving for displacement u_i, strain ε_{ij} and stress $\tilde{\sigma}_{ij}$ which satisfies the equilibrium equations (2.18), constitutive law (2.25) and the boundary conditions

$$u_i = \tilde{U}_i \text{ or}$$

$$t_i = n_j (\sigma_{ji} - \mu_{kji,k}) - D_j (n_k \mu_{kji}) + (D_l n_l) n_j n_k \mu_{kji} = \tilde{T}_i \qquad \text{-------------- (2.26a)}$$

and

$$u_{i,j}n_j = \tilde{U}_i^{\,n} \quad \text{or} \quad \tau_i = n_j n_k \mu_{kji} = \tilde{T}_i^{\,D} \qquad \text{-------------- (2.26b)}$$

where $\tilde{U}_i, \tilde{U}_i^{\,n}, \tilde{T}_i$ and $\tilde{T}_i^{\,D}$ are the prescribed values of displacement , normal derivative of displacement, traction and double traction respectively on their appropriate boundary portions [11].

2.3)   Moment Equations:

The incorporation of displacement gradient into strain energy density function only in the symmetric form, i.e; strain, guarantees a priori the invariance of strain energy with the rigid body motion. Variational formulation with such a strain energy density function does not explicitly give the moment equilibrium equations. The moment equilibrium equations are derived from the variational formulation with a strain energy density function, dependent on displacement gradient, with the imposition of its invariance with respect to anti-symmetric part of displacement gradient. The proof presented here is a slight modification of the proof in [10].

The strain energy density function takes the form:

$$W' = W'\left(u_{i,j}, \varepsilon_{ij,k}\right) \qquad \text{-------------- (2.27)}$$

Considering the variation of internal work,

19

$$W_I' = \int_V \delta W' dV \qquad\qquad \text{------------------ (2.28)}$$

Considering the integrand in the above equation, we have

$$\delta W' = \frac{\partial W'}{\partial u_{i,j}} \delta u_{i,j} + \frac{\partial W'}{\partial \varepsilon_{ij,k}} \delta \varepsilon_{ij,k} \qquad\qquad \text{---------------- (2.29)}$$

Defining,

$$\mu_{kji}' = \frac{\partial W'}{\partial \varepsilon_{ij,k}} = \mu_{kij}'$$

The above equation (2.29) can be written as:

$$\delta W' = \frac{\partial W'}{\partial u_{i,j}} \delta u_{i,j} + \mu_{kji}' \delta \varepsilon_{ij,k}$$

$$\delta W' = \frac{\partial W'}{\partial u_{i,j}} \delta u_{i,j} + \mu_{kji}' \left(\delta u_{i,jk} - \delta \varpi_{ij,k} \right)$$

Since $\mu_{kji}' = \mu_{kij}'$,

$$\delta W' = \frac{\partial W'}{\partial u_{i,j}} \delta u_{i,j} + \mu_{kji}' \delta u_{i,jk}$$

$$= \left(\frac{\partial W'}{\partial u_{i,j}} \delta u_i \right)_{,j} - \left(\frac{\partial W'}{\partial u_{i,j}} \right)_{,j} \delta u_i + \left(\mu_{kji}' \delta u_{i,j} \right)_{,k} - \mu_{kji,k}' \delta u_{i,j}$$

$$= \left(\frac{\partial W'}{\partial u_{i,j}} \delta u_i \right)_{,j} - \left(\frac{\partial W'}{\partial u_{i,j}} \right)_{,j} \delta u_i + \left(\mu_{kji}' \delta u_{i,j} \right)_{,k}$$

$$- \left(\mu_{kji,k}' \delta u_i \right)_{,j} + \mu_{kji,kj}' \delta u_i \qquad\qquad \text{------------------ (2.30)}$$

Substituting equation (2.30) in equation (2.28) and applying divergence theorem, we obtain

$$W_I' = \int_S n_j \left[\left(\frac{\partial W'}{\partial u_{i,j}} \right) - \mu'_{kji,k} \right] \delta u_i \, dS - \int_V \left[\left(\frac{\partial W'}{\partial u_{i,j}} \right)_{,j} - \mu'_{kji,kj} \right] \delta u_i \, dV + \int_S n_k \mu'_{kji} \delta u_{i,j} \, dS$$

Now defining,

$$\tilde{\sigma}'_{ji} = \frac{\partial W'}{\partial u_{i,j}} - \mu'_{kji,k} \qquad \text{---------------- (2.31)}$$

And then applying the condition of invariance of strain energy with respect to rigid body rotation, that is

$$\frac{\partial W'}{\partial u_{[i,j]}} = 0 \qquad \text{where [] denotes anti-symmetric part} \qquad \text{---------------- (2.32)}$$

we have,

$W' \to W$, $\tilde{\sigma}' \to \tilde{\sigma}$, $\mu' \to \mu$ and equation (2.31) reduces to:

$$\tilde{\sigma}_{[ji]} + \mu_{k[ji],k} = 0 \qquad \text{Moment Equilibrium equations} \qquad \text{------------------ (2.33)}$$

Since $\mu_{kji} = \mu_{kij}$,

$$\tilde{\sigma}_{[ji]} = 0 \qquad \text{Moment Equilibrium equations} \qquad \text{------------------ (2.34)}$$

The above equation proves that the stress tensor $\tilde{\sigma}$ is symmetric. The symmetry of the stress tensor in this particular form of strain gradient theory reduces the computational effort to a large extent as opposed to the asymmetric stress tensor of Form I, Form III of Mindlin's theory and couple stress theory.

2.4) **The Uniqueness theorem:**

The proof of uniqueness of the solution of equilibrium equations (2.18) with the
constitutive equation (2.25) and the boundary conditions (2.26) is presented below [11].
Assuming, a contradiction of the uniqueness of solution, that there exist two different
solutions $\{u_i^1, \varepsilon_{ij}^1, \tilde{\sigma}_{ij}^1\}$, $\{u_i^2, \varepsilon_{ij}^2, \tilde{\sigma}_{ij}^2\}$ of the same set of equations. It can be easily conceived
that the difference of the two different solutions is also a solution of the set of equations.
Therefore, the difference solution is

$$u_i = u_i^1 - u_i^2 \quad , \quad \varepsilon_{ij} = \varepsilon_{ij}^1 - \varepsilon_{ij}^2 \quad , \quad \tilde{\sigma}_{ij} = \tilde{\sigma}_{ij}^1 - \tilde{\sigma}_{ij}^2 \qquad \text{----(2.35)}$$

will, obviously, satisfy the governing equations

$$\tilde{\sigma}_{ij,j} = 0 \qquad \text{---------- (2.36)}$$

and the homogeneous boundary conditions

$$u_i = 0 \quad \text{or}$$

$$\text{--------- (2.37)}$$

$$t_i = n_j(\sigma_{ji} - \mu_{kji,k}) - D_j(n_k \mu_{kji}) + (D_l n_l) n_j n_k \mu_{kji} = 0$$

and

$$u_{i,j}n_j = 0 \qquad \text{or} \qquad \tau_i = n_j n_k \mu_{kji} = 0 \qquad \text{-------------- (2.38)}$$

Now, multiplying the equilibrium equations (2.36) with u_i and integrating over the volume,

$$\int_V \tilde{\sigma}_{ij,j} u_i dV = 0 \qquad \text{-------------- (2.39)}$$

$$\int_V \tilde{\sigma}_{ij} u_{i,j} dV = \int_V \left(\tilde{\sigma}_{ij} u_i \right)_{,j} dV \qquad \text{-------------- (2.40)}$$

Applying divergence theorem to the integral on the right hand side of equation (2.40) and using the symmetry of $\tilde{\sigma}_{ij}$, we obtain

$$\int_V \tilde{\sigma}_{ij} \varepsilon_{ij} dV = \int_S \tilde{\sigma}_{ij} u_i n_j dS \qquad \text{-------------- (2.41)}$$

Using the homogeneous boundary condition (2.37),

$$\int \tilde{\sigma}_{ij} \varepsilon_{ij} dV = 0 \qquad \text{-------------- (2.42)}$$

Substituting the constitutive equation (2.25) in the above equation, we have

23

$$\int_V \left(\lambda \varepsilon_{pp} \delta_{ij} + 2\mu \varepsilon_{ij} \right) \varepsilon_{ij} dV - l^2 \int_V \left(\lambda \varepsilon_{pp} \delta_{ij} + 2\mu \varepsilon_{ij} \right)_{,mm} \varepsilon_{ij} dV = 0 \qquad \text{------------- (2.43)}$$

Applying divergence theorem to the second integral of equation (2.43) and rearranging the terms, we obtain

$$\int_V \left(\lambda \varepsilon_{pp} \delta_{ij} + 2\mu \varepsilon_{ij} \right) \varepsilon_{ij} dV + l^2 \int_V \left(\lambda \varepsilon_{pp} \delta_{ij} + 2\mu \varepsilon_{ij} \right)_{,m} \varepsilon_{ij,m} dV$$

$$= l^2 \int_S \left(\lambda \varepsilon_{pp} \delta_{ij} + 2\mu \varepsilon_{ij} \right)_{,m} n_m \varepsilon_{ij} dS \qquad \text{--------- (2.44)}$$

Using the boundary condition (2.38), the integral on the right hand side vanishes with

$$\int_V \left(\lambda \varepsilon_{pp} \delta_{ij} + 2\mu \varepsilon_{ij} \right) \varepsilon_{ij} dV + l^2 \int_V \left(\lambda \varepsilon_{pp} \delta_{ij} + 2\mu \varepsilon_{ij} \right)_{,m} \varepsilon_{ij,m} dV = 0 \qquad \text{--------- (2.45)}$$

The above equation is quadratic in strain ε_{ij} and strain gradient $\varepsilon_{ij,k}$. Since the above equation holds true for any arbitrary strain field ε_{ij}, strain gradient field $\varepsilon_{ij,k}$ and over any arbitrary volume, the following inequalities must be true [11a]

$$3\lambda + 2\mu > 0, \quad \mu > 0 \quad \text{and} \quad l^2 > 0 \qquad \text{------------------ (2.46)}$$

The first two inequalities in (2.46) are also the conditions of uniqueness of solution of classical linear elasticity. The non-classical condition for the unique solution is that the gradient parameter must be positive.

To understand this condition from more physical perspective, an analogy is drawn between the linear couple stress theory and the strain gradient theory. In the couple stress theory for an isotropic material, the introduction of rotational gradients demands an additional modulus of elasticity, apart from the classical modulli: shear modulus and Youngs modulus, which relates the couple stress to the curvature or gradient of rotation (i.e.; the ratio of couple stress to rotation gradient) with the dimensions of force. The length parameter is introduced into the theory through this bending-twisting modulus. The material length parameter is adopted as the square root of the ratio of bending-twisting modulus to the shear modulus. The requirement of positive definiteness of strain energy demands a positive bending-twisting modulus. This condition in turn implies that the characteristic length parameter be positive. Analogously, in the strain gradient theory of isotropic materials, an additional modulus which connects the double stress and the strain gradient is introduced with the dimensions of force. The gradient parameter l^2 is introduced through this modulus. The condition of uniqueness that l^2 be positive implies, in other words, that the modulus connecting double stress to strain gradient be positive for the strain energy to be positive definite (that is, energy is stored upon deformation not produced).

2.5) **Gradient Enhanced formulations**

The strain gradient elasticity can also be derived directly from the non-local theory. These formulations are classified as implicit and explicit based on the way non-local strain is expressed in terms of local strain. In these formulations, the higher order terms are directly incorporated in a constitutive framework. (R.H.J.peerlings et al [14])

2.5.1) Implicit Formulation:

The non-local strain is defined as a weighted average of the local strain over a certain volume.

$$\tilde{\varepsilon}(x) = \frac{1}{V}\int g(\xi)\varepsilon(x+\xi)dV \text{ , with } \frac{1}{V}\int g(\xi)dV = 1 \qquad \text{----- (2.47)}$$

where $g(\xi)$ is a weight function and ξ denotes the relative position vector of the infinitesimal volume dV. x is the material point of concern.

In the gradient formulation, the integrand in the definition of non-local strain is approximated with a Taylor series expansion to keep the equations local, purely in mathematical sense.

$$\varepsilon(x+\xi) = \varepsilon(x) + \nabla\varepsilon(x).\xi + \frac{1}{2!}\nabla^{(2)}\varepsilon(x).^{(2)}\xi^{(2)}$$

$$+ \frac{1}{3!} \nabla^{(3)} \cdot^{(3)} \xi^{(3)} + \frac{1}{4!} \nabla^{(4)} \cdot^{(4)} \xi^{(4)} + \dots \qquad \text{-------- (2.48)}$$

where $\nabla^{(n)}$ and $\cdot^{(n)}$ are the n the order gradient operator and nth order inner product. $\xi^{(n)}$ denotes the n factor product. Assuming isotropy and integrating (2.47) with the substitution of (2.48) over a symmetric volume vanishes all the odd functions and results in

$$\tilde{\varepsilon} = \varepsilon + c\nabla^2\varepsilon + d\nabla^4\varepsilon + \dots \qquad \text{--------- (2.49)}$$

where the coefficients c and d are dependent on the weight function $g(\xi)$ and the volume over which averaging is done. Neglecting the higher order terms from (2.49), the non-local strain can expressed as

$$\tilde{\varepsilon} = \varepsilon + c\nabla^2\varepsilon \qquad \text{-------- (2.50)}$$

The coefficient of laplacian of local strain, the non-classical parameter, with dimensions of squared length is introduced. This characteristic length parameter is related to the microstructure of the material. The dependence of the non-local strain on the local strain is explicit in the above equation. Differentiating equation (2.49) twice and rearranging terms gives,

$$\nabla^2\varepsilon = \nabla^2\tilde{\varepsilon} - c\nabla^4\varepsilon - d\nabla^6\varepsilon \qquad \text{-------- (2.51)}$$

27

Using equation (2.50), we have

$$\widetilde{\varepsilon} - c\nabla^2\widetilde{\varepsilon} = \varepsilon + \left(d - c^2\right)\nabla^4\varepsilon \qquad \text{-------- (2.52)}$$

Neglecting the higher-order gradients and replacing c with l^2,

$$\widetilde{\varepsilon} - l^2\nabla^2\widetilde{\varepsilon} = \varepsilon \qquad \text{--------- (2.53)}$$

The dependence of non-local strain on the local strain in the above equation is implicit.
The governing equations of the implicit formulation of gradient elasticity:

$$\nabla.\sigma = 0 \qquad \text{---------- (2.54.1)}$$

$$\widetilde{\varepsilon} - l^2\nabla^2\widetilde{\varepsilon} = \varepsilon \qquad \text{---------- (2.54.2)}$$

Besides solving the classical equilibrium equations of linear elasticity with the classical boundary conditions, the additional PDE (2.54.2) is required to be solved with appropriate additional boundary conditions. In order to solve the additional PDE (2.54.2), boundary conditions of the dirichlet or Neumann type have to be specified. From purely mathematical perspective, it is necessary to specify either $\widetilde{\varepsilon}$ or $\nabla.\widetilde{\varepsilon}.\hat{n}$ on the boundary. The boundary condition usually adopted in the literature is

$$\nabla.\widetilde{\varepsilon}.\hat{n} = 0 \qquad \text{---------- (2.54.3)}$$

There is no reasonable physical explanation given to the above choice of boundary conditions as opposed to the boundary conditions derived from a variational approach.

2.5.2) Explicit Formulation

In Explicit formulation, the dependence of non-local strain on local strain is explicit. In the equation (2.50), the non-local strain is explicitly dependent of the local strain. Rearranging terms in the equation (2.50), we obtain

$$\varepsilon = \widetilde{\varepsilon} - c\nabla^2\varepsilon \qquad \text{------ (2.55)}$$

By approximating the laplacian of local strain to be almost same as the laplacian of non-local strain and replacing c with l^2,

$$\varepsilon = \widetilde{\varepsilon} - l^2\nabla^2\widetilde{\varepsilon} \qquad \text{------- (2.56)}$$

Substituting the above equation in the Hooke's law, the constitutive law of explicitly gradient enhanced elasticity theory is

$$\sigma = D\left(\widetilde{\varepsilon} - l^2\nabla^2\widetilde{\varepsilon}\right) \qquad \text{-------- (2.57)}$$

The governing equations of explicit form of gradient elasticity are

$$\nabla . \sigma = 0 \qquad\qquad \text{-------- (2.58)}$$

A properly formulated boundary problem involves in solving above higher-order partial differential equation with appropriate and sufficient boundary conditions. Argued purely from a mathematical stand point, there is a need for higher-order boundary conditions to solve a higher-order PDE. The higher-order boundary condition used in this case is

$$\nabla \widetilde{\varepsilon} . \hat{n} = 0 \qquad\qquad \text{----------- (2.59)}$$

Any physical reasoning cannot be attached to this choice of boundary condition. It is worth comparing the above boundary condition with the boundary conditions derived from variational formulation. The higher-order boundary conditions derived from variational method are,

$$u_{i,j} n_j = \widetilde{U}_i^{\,n} \qquad \text{or} \qquad \tau_i = n_j n_k \mu_{kji} = \widetilde{T}_i^{\,D} \qquad\qquad \text{------------ (2.60)}$$

With double stress expressed in terms of strain,

$$\tau_i = n_j n_k l^2 \left(\lambda \varepsilon_{pp} \delta_{ij} + 2\mu \varepsilon_{ij} \right)_{,k} = \widetilde{T}_i^{\,D} \qquad\qquad \text{------------ (2.61)}$$

By comparing BC (2.59) with BC (2.61), one can say that imposing BC (2.59) is equivalent to prescribing double traction to zero. The question as to why only zero is still

unanswered. The finite element formulation of gradient elasticity using C^1 interpolation of displacement field is discussed in the following chapter.

CHAPTER 3

Finite element formulation

The finite element formulation of the equilibrium equations (2.18) of the gradient elasticity is presented in this chapter. The continuity requirements of the displacement field for the gradient elasticity, the finite element used and the weak formulation of the governing equations is also discussed below.

3.1) Continuity requirements:

An examination of boundary terms of variational statement of gradient elasticity suggests that the essential boundary conditions involves the specification of displacement and normal surface gradient of displacement, which constitute the primary variables of the problem. Hence, the finite element which could guarantee continuity in displacement and displacement gradient at the nodes and all along the element edge is sufficient. It seems that a cubic interpolation using a 9-DOF element would be sufficient, but it does not serve the purpose. A critical examination of 9-DOF cubic interpolation higher order element is done below.

Triangular element with corner nodes (9 DOF)

A 9-DOF triangular element has displacement and two first partial derivatives of displacement as its degrees of freedom per node. As the finite element has nine degrees

of freedom, an interpolation polynomial with only nine terms is permissible. An immediate difficulty arises as a complete cubic polynomial has ten terms.

$$u = \alpha_1 + \alpha_2 x + \alpha_3 y + \alpha_4 x^2 + \alpha_5 xy + \alpha_6 y^2$$
$$+ \alpha_7 x^3 + \alpha_8 x^2 y + \alpha_9 xy^2 + \alpha_{10} y^3$$

------------- (3.1)

To retain the sense of complete polynomial, all the ten terms in the equation (3.1) could be retained with any two coefficients made equal (for example $\alpha_8 = \alpha_9$) to limit the number of unknowns to nine. Several such possibilities have been investigated but a further, much more serious, problem arises in deriving the shape functions [21].

To ensure the continuity of the displacement and displacement gradient across an element edge, we must have both displacement and displacement gradient uniquely determined by the values of the nodes along that edge. At any constant x, it can be noticed from the equation (3.1) that the function varies as a cubic in y. Along a given side, there are two nodes and two nodal values (displacement and its gradient) to uniquely determine a cubic variation. Hence, the displacement is continuous at the nodes as well as all along the element edge. The normal derivative of displacement (say $u_{,x}$) varies as a quadratic function in y between the nodal points. Since, only two nodal values of normal displacement gradient are available, a unique quadratic variation cannot be defined. This results in an inter-element incompatibility of displacement gradient. In addition, $u_{,xy}$ is not single-valued at the corner points of the element. This non-conforming 9-DOF

33

triangular element is found to have convergence problems and singular behavior for certain meshes [22].

A way out of this difficulty of non-conformity is to use cross derivative of displacement as one of the degrees of freedom. By doing so, displacement gradient is inter-element compatible. Unfortunately, the extension to nodes at which a number of element interfaces meet at different angles is not in general permissible. Here the continuity of cross-derivatives in several sets of orthogonal directions implies in fact a specification of *all second derivatives at a node* [23].

Keeping in mind the non-conforming problems posed by 9-DOF triangular element, we wisely chose an element with displacement, two first partial derivatives and all second partial derivatives of displacement which guarantees continuity of displacement and displacement gradient at nodes and all along the edge.

In addition to the above mentioned conformity requirements, the variational statement of the gradient elasticity consists of strain as well as strain gradient which demand the displacement field to be continuous enough so that the strain gradients exist. The constitutive equation of gradient elasticity has Laplacian of the strain which even imposes the higher continuity on the interpolation function of displacement field. Therefore, the shape functions of displacement should be polynomials of sufficiently higher-order so that they do not vanish when differentiated three times. The extra continuity requirements on the interpolation function leave a very restricted choice of elements [24].

34

3.2) C^1 finite element:

The finite element used in the present work is a higher-order triangular bending element formulated by Dasgupta & Sengupta in the reference [14]. The C^1 finite element is shown in the Fig. 2 below.
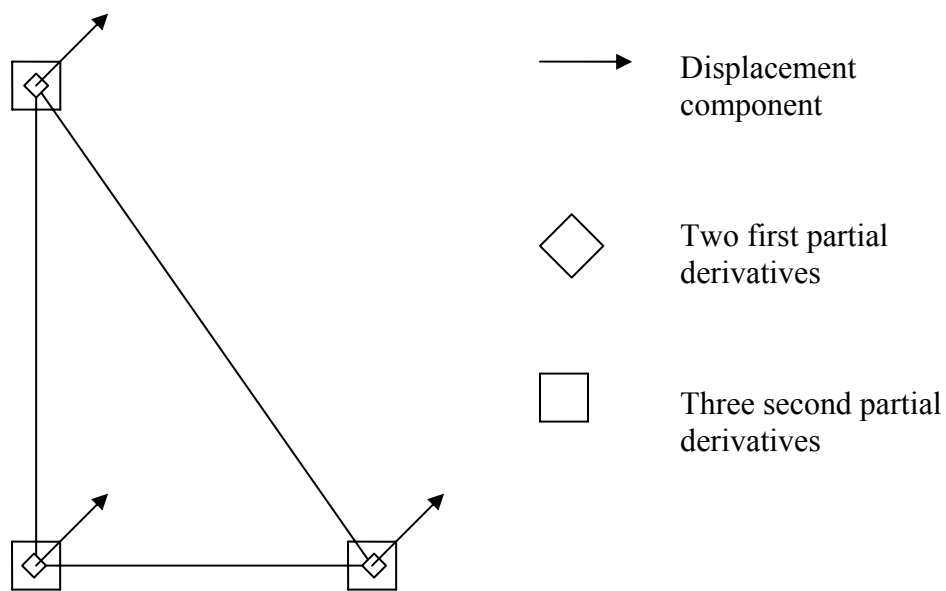
Fig 2: C^1 Finite Element

This element uses a complete quintic polynomial to interpolate displacement field. It has 3 nodes with six degrees of freedom per node for each displacement component. The degrees of freedom are the displacement, its two first derivatives and its three second derivatives at each node. This results in eighteen degrees of freedom for each displacement component per each element. Therefore, for the displacement vector field,

the total number of degrees of freedom per element are thirty six. The normal derivative of displacement along the element edge is constrained to vary as a cubic polynomial. The laplacian of strains vary as quadratic function inside the element.

$$\vec{u} = \begin{Bmatrix} u \\ v \end{Bmatrix} = [N].\{\hat{u}\}$$ -------------- (3.1)

where

$$N = \begin{bmatrix} N_1...N_6 0....0 N_7...N_{12} 0....0 N_{13}...N_{18} 0....0 \\ 0.....0 N_1....N_6 0....0 N_7....N_{12} 0....0 N_{13}...N_{18} \end{bmatrix}$$

$$\hat{u} = \begin{bmatrix} u_1 u_{1,x} u_{1,y} u_{1,xx} u_{1,xy} u_{1,yy} v_1....v_{1,yy} u_2.....u_{2,yy} v_2....v_{2,yy} u_3....v_{3,yy} \end{bmatrix}^T$$

where u is the displacement component along the global x-axis and v is the displacement component along the global y-axis. A comma following each subscript denotes the spatial partial derivative of the displacement component along that direction. N is the matrix of shape functions. The shape functions of this element are given in the appendix.

3.3) Weak formulation of the governing equations:

The weak form of the problem of solving equilibrium equations is the same as solving the variational statement with appropriate boundary conditions. Therefore, the weak form of the boundary value problem can be stated as follows:

Given t_i and τ_i on the traction boundary, find u_i, which satisfies the prescribed displacement conditions on the displacement boundary, such that for any arbitrary variations δu_i and $\delta u_{i,j} n_j$

$$\int_V \sigma_{ij} \delta \varepsilon_{ij} \, dV + l^2 \int_V \mu_{kji} \delta \varepsilon_{ij,k} \, dV = \int_\Gamma t_i \delta u_i \, dS + \int_\Gamma \tau_i \delta u_{i,j} n_j \, dS \qquad \text{--- (3.2)}$$

equation (3.2) is true and, in turn, find $\varepsilon_{ij}, \tilde{\sigma}_{ij}$ using

$$\varepsilon_{ij} = \frac{1}{2}\left(u_{i,j} + u_{j,i}\right) \qquad \text{-------- (3.3)}$$

$$\tilde{\sigma}_{ji} = \lambda \varepsilon_{pp} \delta_{ji} + 2\mu \varepsilon_{ji} - l^2 \left(\lambda \varepsilon_{pp} \delta_{ji} + 2\mu \varepsilon_{ji}\right)_{,kk} \qquad \text{-------- (3.4)}$$

Strain and Strain gradient expressed in vector form:

$$\varepsilon = \begin{Bmatrix} \varepsilon_{11} \\ \varepsilon_{22} \\ \varepsilon_{12} \end{Bmatrix} = B.\hat{u}$$ ------------- (3.5)

$$\varepsilon_{,1} = \begin{Bmatrix} \varepsilon_{11,1} \\ \varepsilon_{22,1} \\ \varepsilon_{12,1} \end{Bmatrix} = B_{xx}\hat{u}$$ ------------- (3.6)

$$\varepsilon_{,2} = \begin{Bmatrix} \varepsilon_{11,2} \\ \varepsilon_{22,2} \\ \varepsilon_{12,2} \end{Bmatrix} = B_{yy}\hat{u}$$ ------------- (3.7)

where B, B_{xx} and B_{yy} are the matrices with first partial derivatives, second partial derivatives w.r.t x and second partial derivatives w.r.t y of shape functions repectively. Stress and double stress expressed in the vector form:

$$\sigma = \begin{Bmatrix} \sigma_{11} \\ \sigma_{22} \\ \sigma_{12} \end{Bmatrix} = D.\varepsilon = D.B.\hat{u}$$ ------------ (3.8)

$$\mu_{1ji} = \begin{Bmatrix} \mu_{111} \\ \mu_{122} \\ \mu_{112} \end{Bmatrix} = l^2.D.\varepsilon_{,1} = l^2.D.B_{xx}\hat{u}$$ ------------ (3.9)

$$\mu_{2ji} = \left\{ \begin{array}{c} \mu_{211} \\ \mu_{222} \\ \mu_{212} \end{array} \right\} = l^2.D.\varepsilon_{,2} = l^2.D.B_{yy}\hat{u} \qquad \text{------------ (3.10)}$$

where l^2 and D are squared characteristic length and isotropic elastic constitutive matrix.

Substituting the equations from (3.5)-(3.10) and using (3.1) in the Variational statement (3.2), Principle of virtual work, we obtain the following system of equations for the nodal degrees of freedom for each element:

$$\left[\int_V \left([B^T][D][B] + l^2 \left\{ [B_{xx}^T][D][B_{xx}] + [B_{yy}^T][D][B_{yy}^T] \right\} \right) dV \right].\hat{u} =$$

$$\int_S \left[[N^T]\hat{t} + \left(n_1[N^T]_1 + n_2[N^T]_2 \right)\hat{\tau} \right] dS \qquad \text{------- (3.11)}$$

where $\hat{t}$ and $\hat{\tau}$ are the applied traction and double traction respectively. The above equation can also be written as:

$$\left\{ K_1 + l^2 \left(K_{xx} + K_{yy} \right) \right\}.\hat{u} = F \qquad \text{---------- (3.12)}$$

$$K.\hat{u} = F \qquad\qquad\text{---------- (3.13)}$$

where K and F are the stiffness and force matrix respectively. It can be observed from the above equations that they reduce to the classical ones when the gradient coefficient l is set to zero.

The integration scheme used to integrate the left hand side of the equation (3.12) is analytical using the formula derived by Eisenberg and Malvern [15]:

$$\int L_1^m L_2^n L_3^p dA = \frac{m!\,n!\,p!}{(m+n+p+2)!} 2\Delta \qquad\qquad\text{------------ (3.14)}$$

where L_1, L_2 and L_3 are the area coordinates

      m, n, p are non-negative integers and

      Δ is the area of the triangle.

CHAPTER 4

RESULTS

In this section, the results of FE analysis of, firstly, a crack in a homogeneous isotropic material upon loading, secondly, an interfacial crack in structurally inhomogeneous bi-material and thirdly, a crack normal to the bi-material interface under loading are presented.

4.1) Crack in a Homogeneous Material:

4.1.1) Material

The material used for the simulation of crack in a homogeneous material is tungsten carbide. Tungsten carbide is a brittle isotropic elastic material with Young's modulus $(E = 680 * 10^9 \, N / m^2)$ and Poisson's ratio $(\nu = 0.25)$.

4.1.2) Geometry and boundary conditions

The geometry and boundary conditions of problem domain are shown in the Fig. 3.
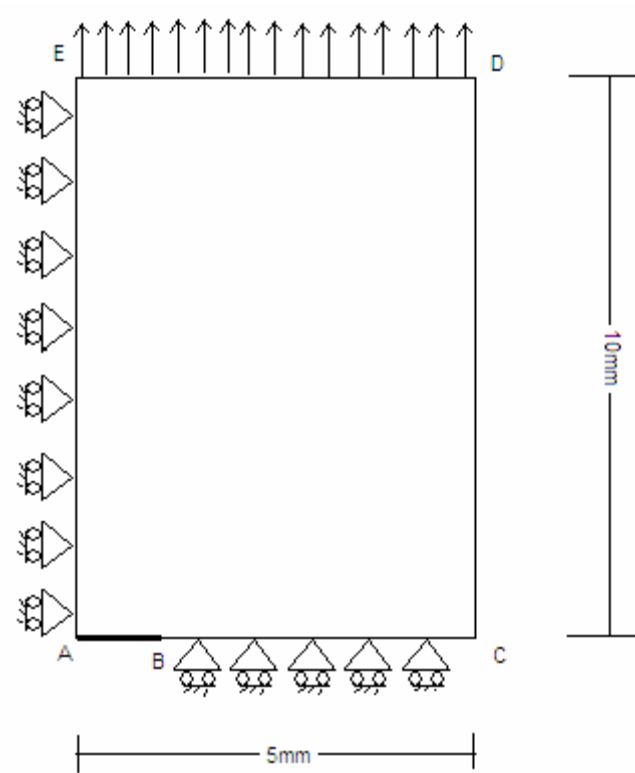
Fig 3: Problem Description: Geometry and boundary conditions

The specimen shown above is one-quarter of a rectangular tensile panel (20x10) with the crack placed in the centre symmetrical both with x and y axes. The specimen is 10mm high, 5mm wide and it is assumed to deform in plane strain conditions. The portion AB of the Fig. 3 represents the crack in the specimen which is traction free. The boundary part BC is the line about which the geometry and loading are symmetric in the Y-direction. BC is prevented from moving in the Y-direction only. The boundary part AE is the line about which the geometry and loading are symmetric in X-direction. AE is prevented from moving in the X-direction only. The specimen is pulled along DE by displacing the surface uniformly by 0.01mm.

In higher-order elements, it is worth paying attention to the way boundary conditions are imposed. In order to prescribe zero vertical displacement all along BC, it is not sufficient

just to prescribe zero displacement at the nodes of the element. As the employed interpolation is not linear, prescribing only at the nodes does not prevent the points between the nodes from moving in the vertical direction. To achieve what is intended, all the derivates of displacement along the element edge must also be prescribed to zero at the nodes, as they are not independent of each other. So, in order to prescribe zero vertical displacement along BC, vertical displacement, its first and second derivatives along BC must be prescribed at all the element nodes.

To apply uniform loading along DE, the vertical displacement is prescribed at all nodes and the first as well as second derivatives along DE are also prescribed as zero. And the horizontal displacement degree of freedom is left free.

In regard to the higher-order boundary conditions, double traction, that is, the gradient of strain normal to the boundary is prescribed as zero on the entire boundary. In order to impose this BC, the second derivatives of displacement normal to the boundary as well as mixed second derivatives are prescribed as zero on the entire boundary.

4.1.3) Mesh Sensitivity Analysis Results

Mesh Sensitivity analysis is a process of refining the mesh to achieve a converged solution. This section presents the results of mesh sensitivity analysis for six different meshes with mesh1 being the coarse and mesh6 being the finest. The results of mesh sensitivity analysis for the structure of crack tip, local stress and Effective stress are presented in the Figs. 4-6.

4.1.3.1) Displacement plots

In Fig. 4(g) below, the vertical displacement of the crack face is plotted against the distance along the crack face. In the Fig. 4(g), the crack tip is at 1mm. The plot lines of the structure of crack tip are shown below for six different meshes as shown in Fig. 4(a)-(f) and compared with the classical solution. As it can be seen from the Fig. the meshes are designed so that it is finer at the crack tip. In this analysis, we use length scale (l) as 100 μ m. As can be seen from the Fig., the response is independent of the mesh size.

(a)   (b)   (c)   (d)

(e)   (f)
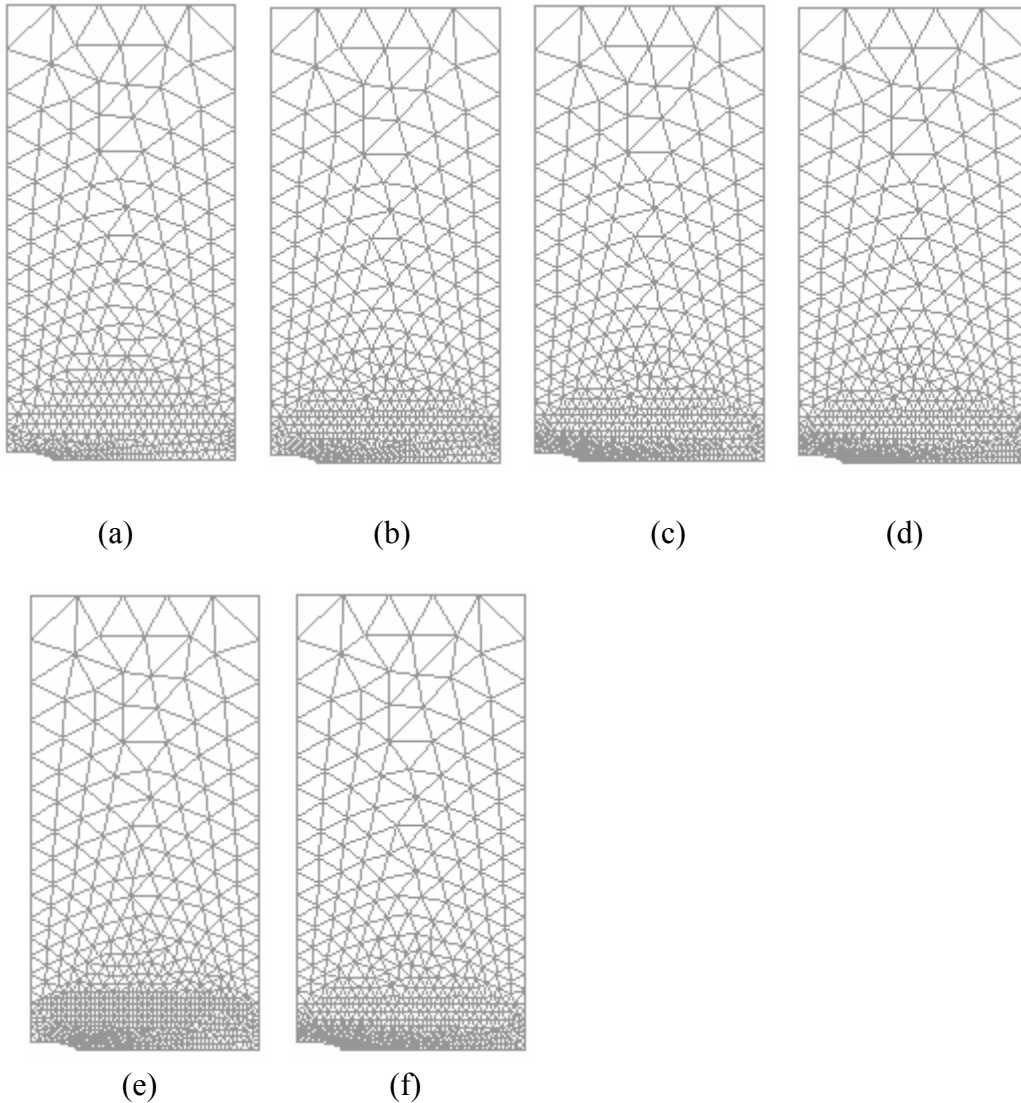
Structure of Crack Tip
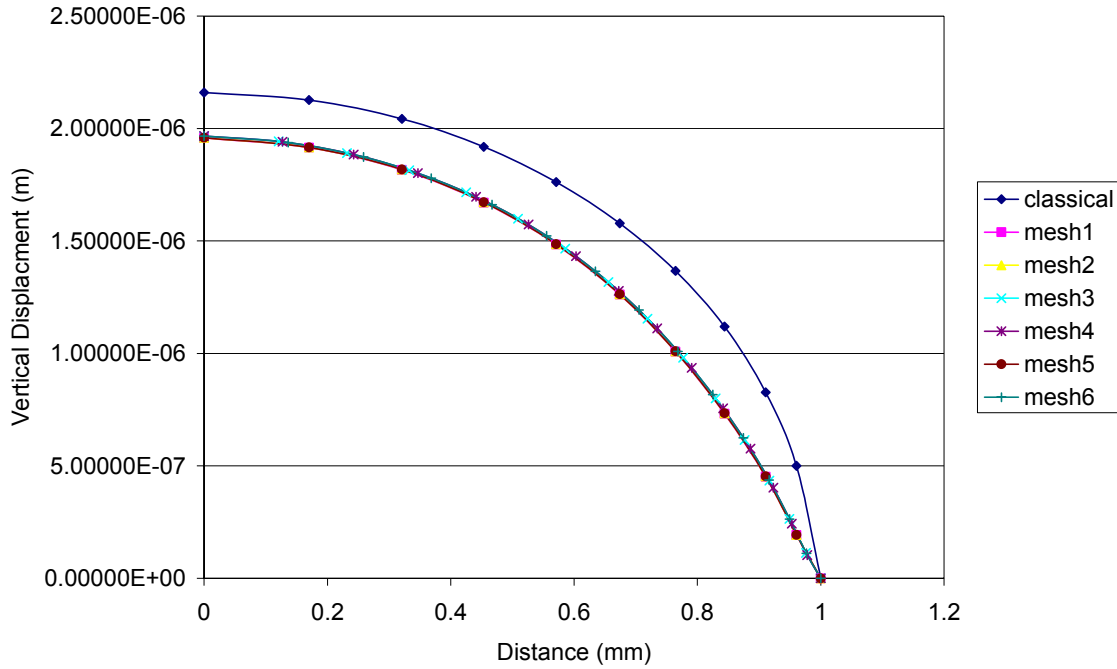
(g)

Fig 4 (a) mesh1 (b) mesh2 (c) mesh3 (d) mesh4 (e) mesh5 (f) mesh6
(g) Mesh Sensitivity of Structure of Crack Tip

4.1.3.2) Stress plots

4.1.3.2.1) Local stress plots

The Constitutive law employed in the present work is

$$\tilde{\sigma}_{ji} = \lambda \varepsilon_{pp} \delta_{ji} + 2\mu \varepsilon_{ji} - l^2 \left(\lambda \varepsilon_{pp} \delta_{ji} + 2\mu \varepsilon_{ji} \right)_{,kk} \quad \text{(Effective stress)} \quad \text{--------- (4.1a)}$$

$$\sigma_{ji} = \lambda \varepsilon_{pp} \delta_{ji} + 2\mu \varepsilon_{ji} \quad \text{(Local)} \quad \text{--------- (4.1b)}$$

where λ, μ and ε are lame's constants and strain respectively. The term local stress represents only the first part of the constitutive law which is given by equation (4.1b).

In the following two graphs, the mesh sensitivity results of the local σ_{22} stress component are presented. The graphs of local σ_{22} stress are plotted for six different meshes as shown in the Fig. 4(a)-(f), with mesh1 being the coarse and mesh 6 being the finest, along the boundary line BC of the specimen (see Fig. 3 above). As can be seen the response is almost independent of the mesh size.

(a)

(b)
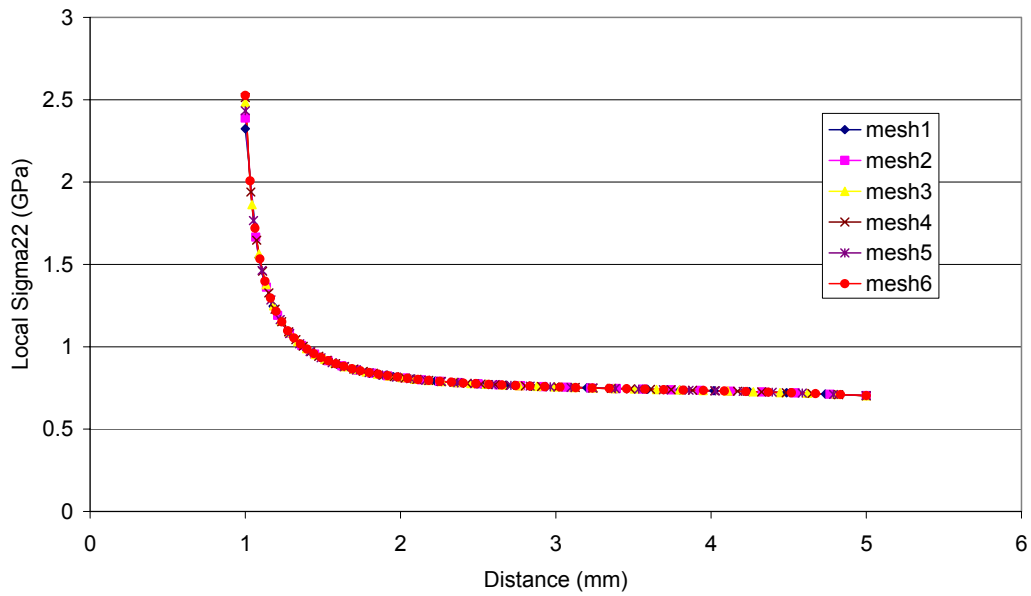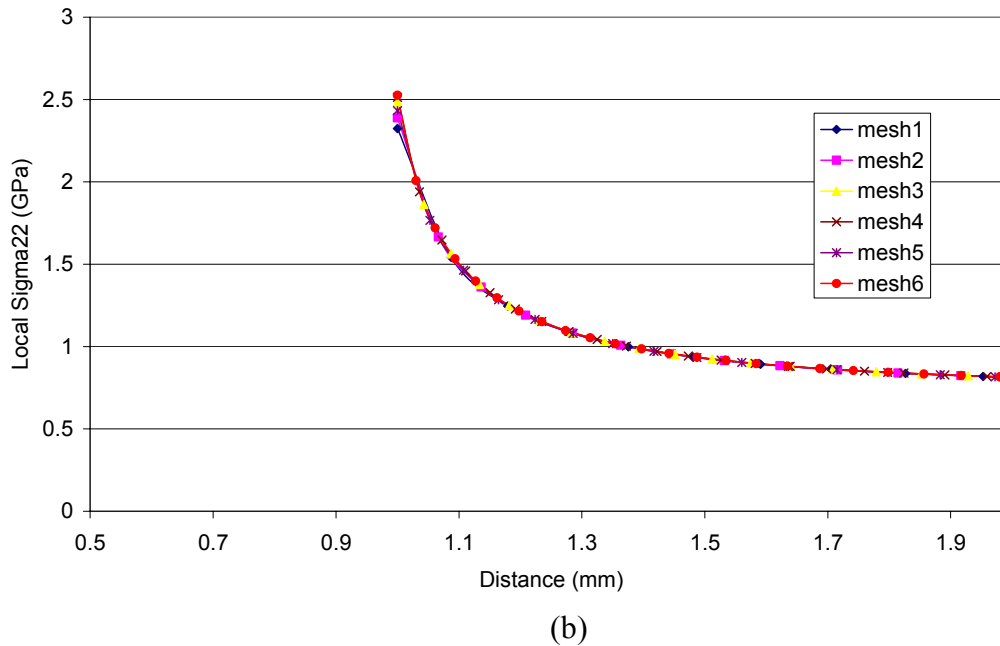
Fig 5 (a) Mesh Sensitivity of Local σ_{22} Stress component
(b) Magnified view of the plot at the crack tip

4.1.3.2.2) Effective stress plots

The term effective stress represents the stress computed from the constitutive equation (4.1a) unlike only the first term of the equation for local stress. In the following two graphs, the plots of the effective σ_{22} stress component are presented for six different meshes as shown in Fig. 4(a)-(f) plotted along the boundary line BC (see Fig. 3 above). It can be seen from the graph that although the solution does not converge completely, the nature of the solution converges to the one shown by the mesh5 & mesh6.

Effective Stress

(a)
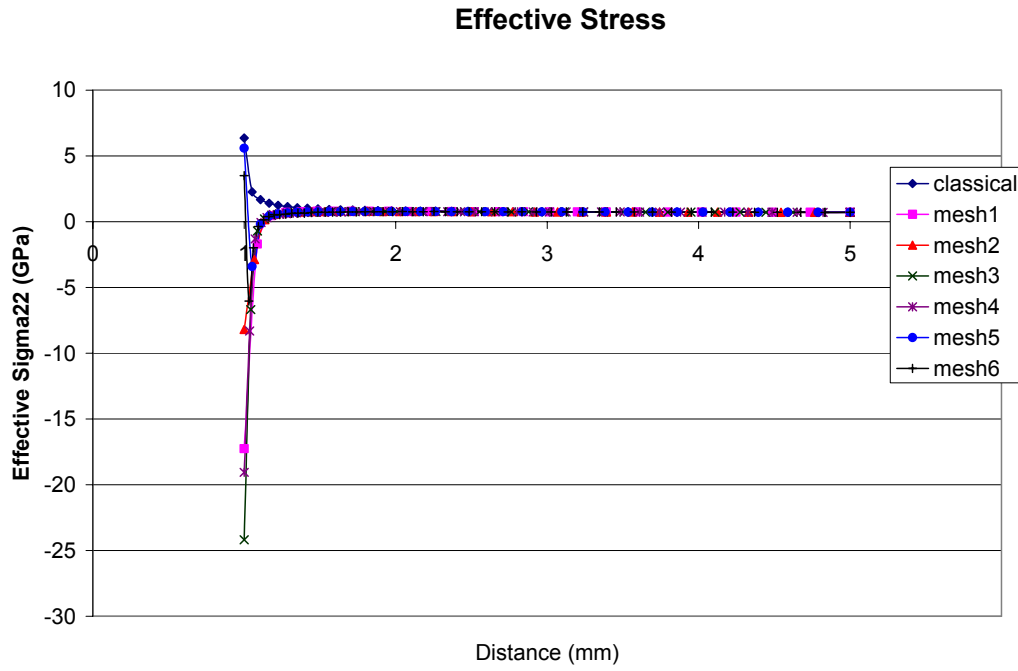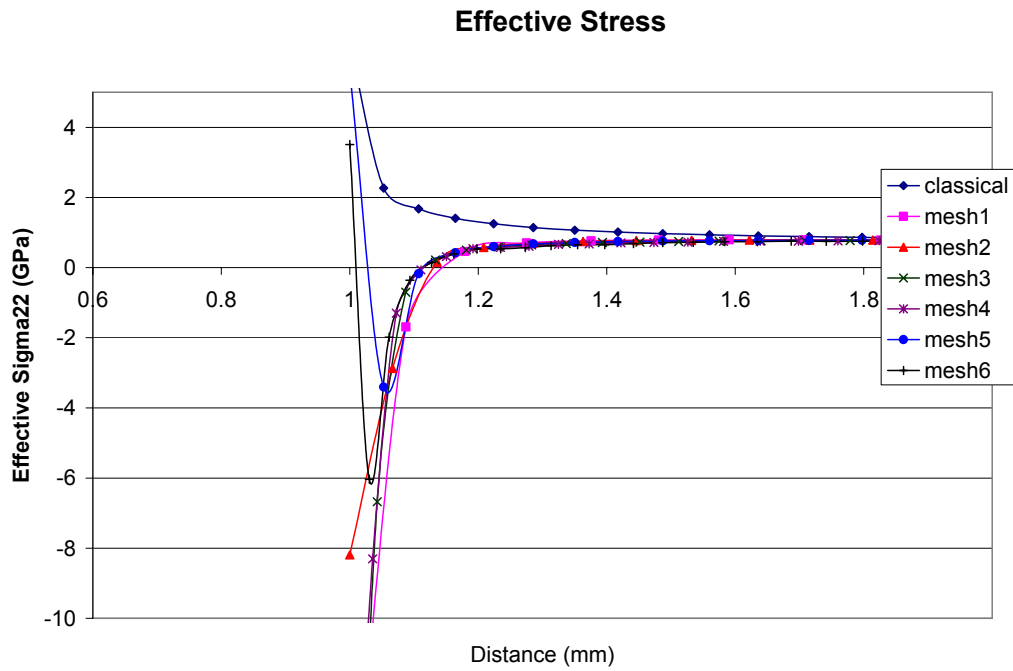
Effective Stress

(b)

Fig 6 (a) Mesh Sensitivity of Effective σ_{22} stress component
(b) Magnified image of the plot near the crack tip

4.1.4) Effect of characteristic length parameter

The length scale (l) is considered as the spatial span over which the non-local mechanical interactions are taken into account. The effect of this length scale on the structure of the crack tip, local stress and effective stress are presented in the Figs. 7-9. The unit of the length scale shown in the legend of the following graphs is micrometers.

4.1.4.1) Displacement plots

The structure of the crack tip is shown for four different characteristic length scales (30, 50, 70&100 micrometers) and compared with the classical solution. Fig. 7(b) shows a closer look at the change in the graph near the crack tip. It can be observed that the closure of the crack tip is smoothened as the length scale is increased.

(a)

(b)
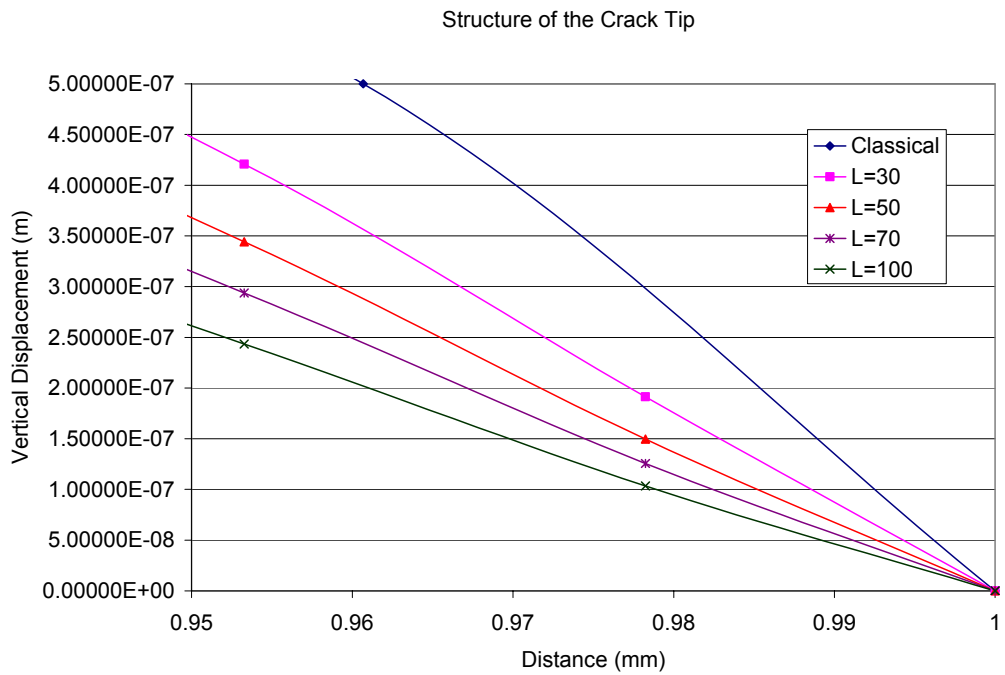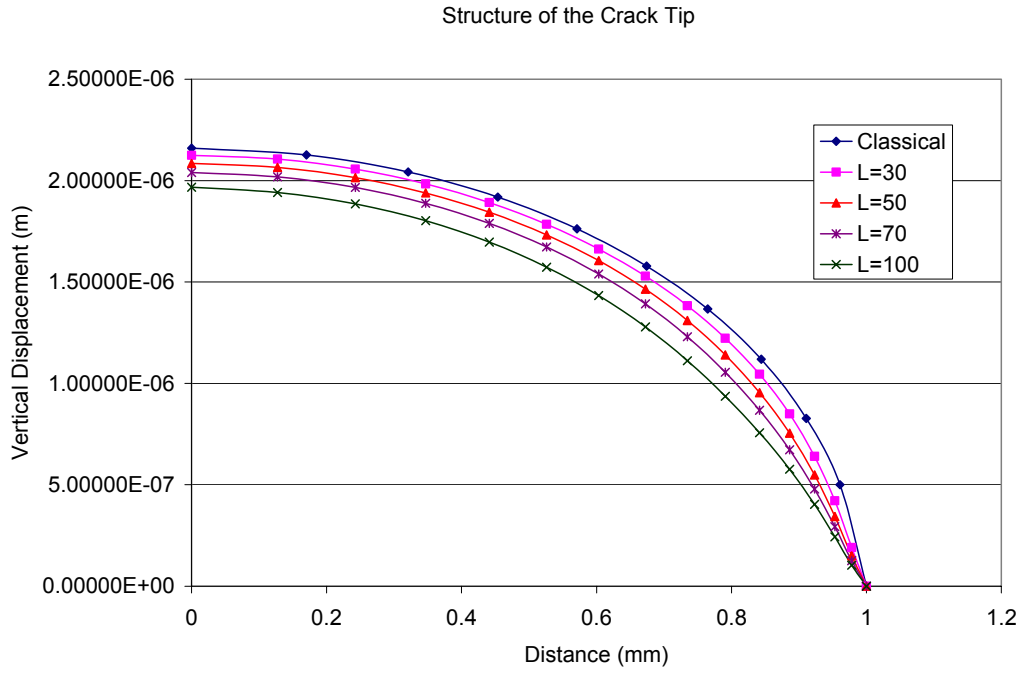
Fig 7 (a) Effect of Characteristic Length Scale (*l*) on the Structure of Crack Tip

(b) Magnified image of the plot at the crack tip

4.1.4.2) Stress plots

4.1.4.2.1) Local stress

The following two graphs present the effect of length scale on the local σ_{22} stress for four different length scales (30, 50, 70&100 micrometers). The stress is plotted along the boundary line BC (see Fig. 3 above). It can be observed that the crack tip stress and the rate at which decays as moved away from the tip are both decreased with increase in length scale. Fig.8 (b) shows the magnified picture of the graph near the crack tip.
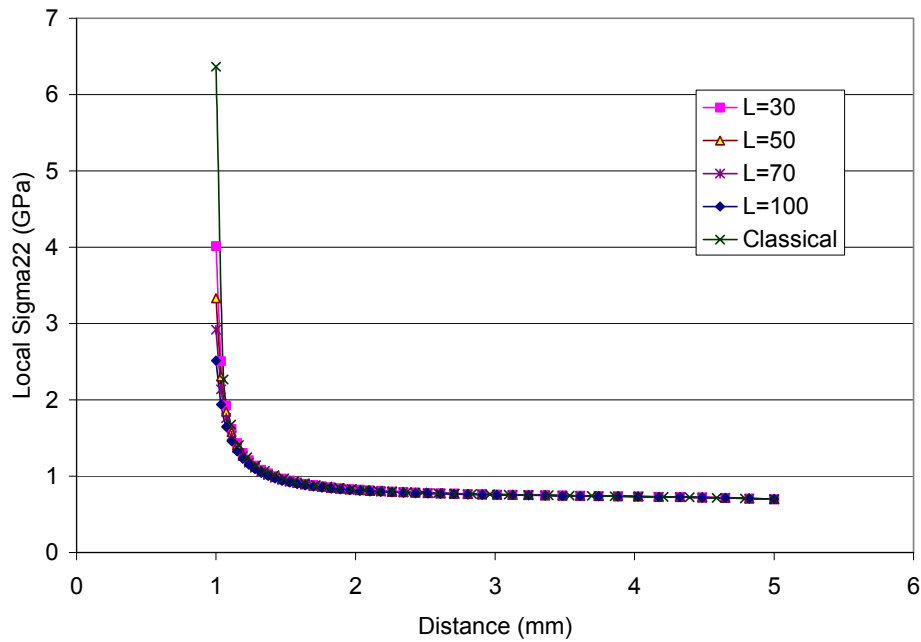
(a)
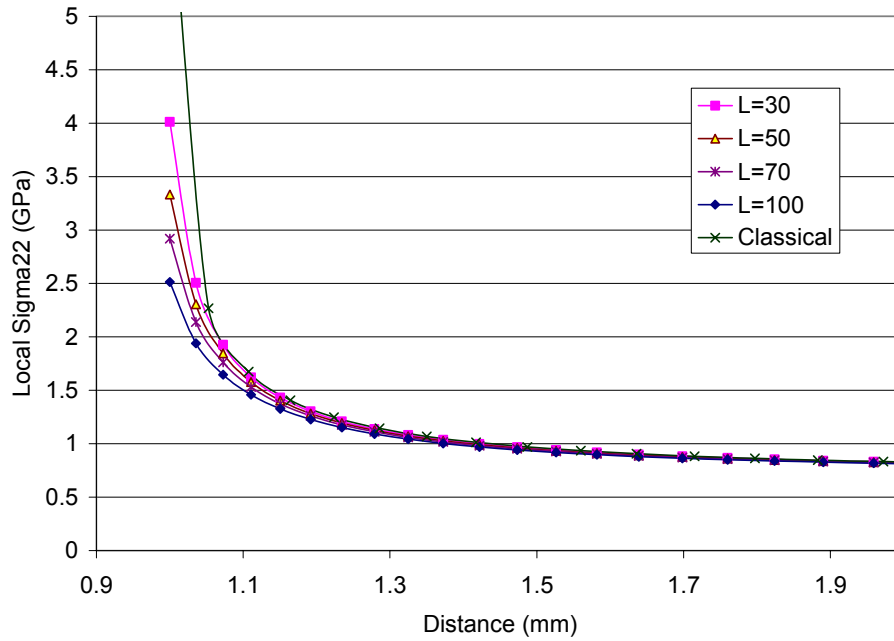
(b)

Fig 8 (a) Effect of Characteristic Length Scale (l) on Local σ_{22} Stress component
(b) Magnified image of the plot near the crack tip

4.1.4.2.2) Effective stress

The graphs below show the effect of length scale on the effective σ_{22} stress component.

The effective σ_{22} stress component is plotted for four different length scales along the

boundary line BC (see Fig. 3 above). Fig. 9(b) is a magnified image of the stress plot near

the crack tip.
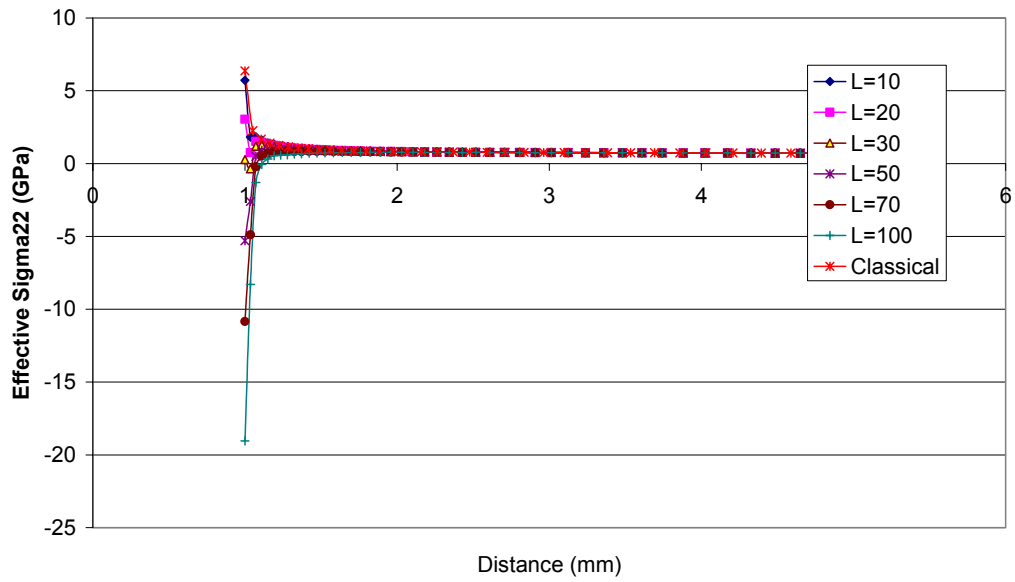
(a)
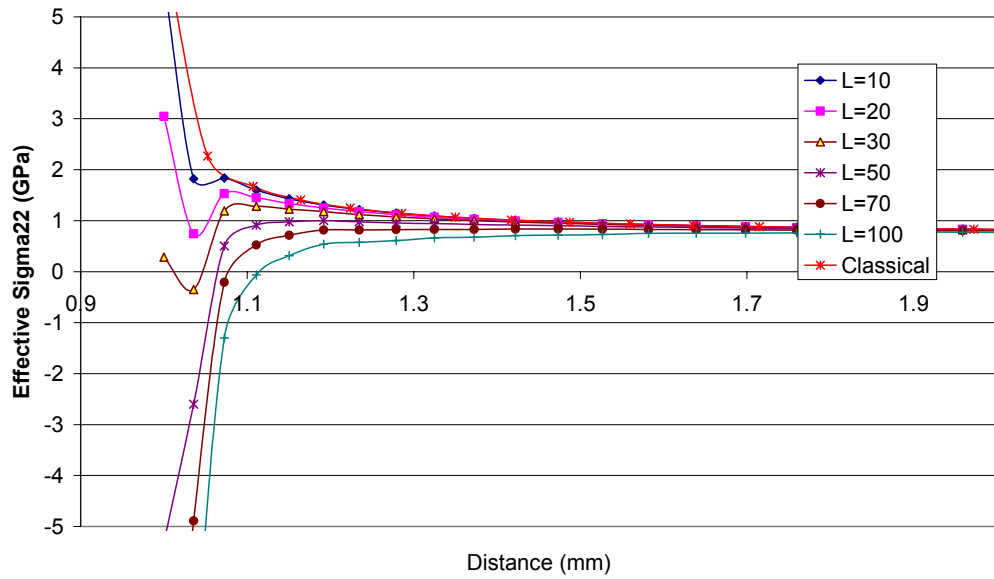
(b)

Fig 9 (a) Effect of Characteristic Length Scale (*l*) on Effective σ_{22} stress component
(b) Magnified image of the plot near the crack tip

4.1.5) Contour Plots:

In this sub-section, the contour plots of local and effective σ_{22} stress for various length scales. The Figs. 10-15 show the contour plots for characteristic length scale10, 20, 30, 50, 70&100 micrometers.

(a)   (b)
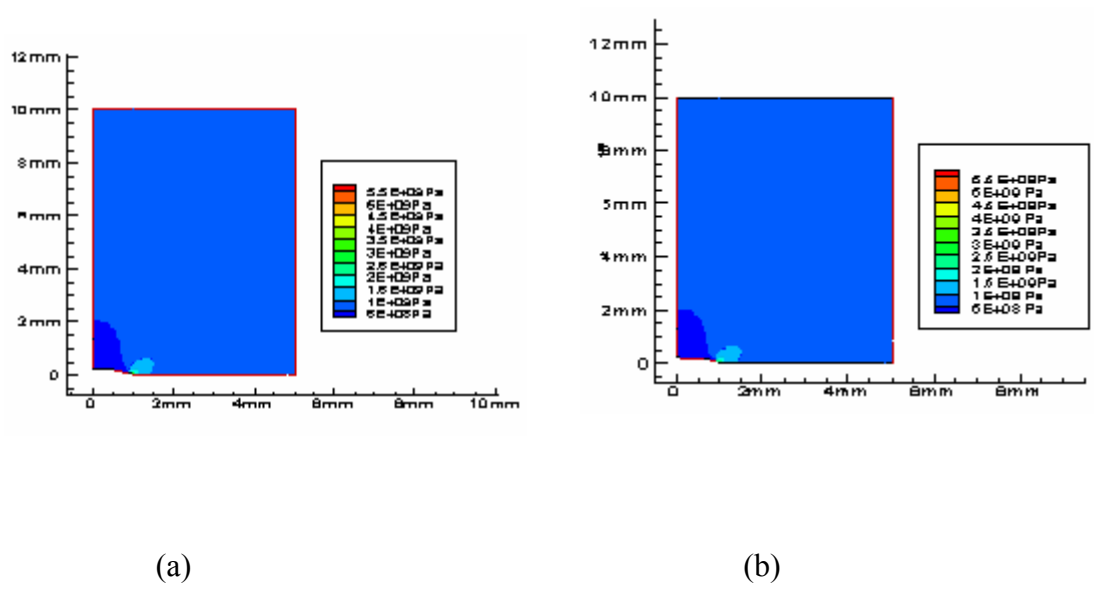
Fig 10: Contour plots of (a) local σ_{22} stress and (b) effective σ_{22} stress for characteristic length scale=10microns.

(a)   (b)
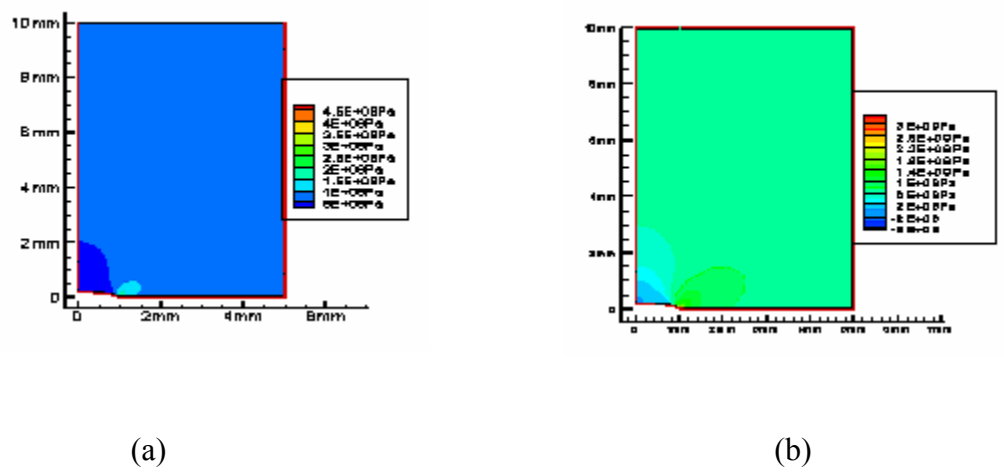
Fig 11: Contour plots of (a) local σ_{22} stress and (b) effective σ_{22} stress for characteristic length scale=20microns.

(a)   (b)
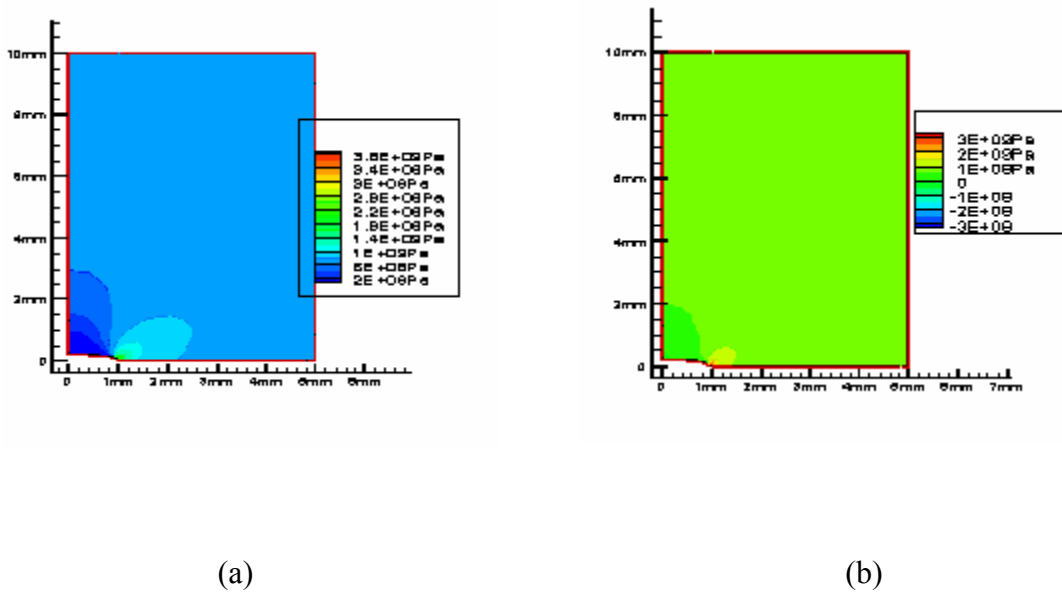
Fig 12: Contour plots of (a) local σ_{22} stress and (b) effective σ_{22} stress for characteristic length scale=30microns.

(a)   (b)
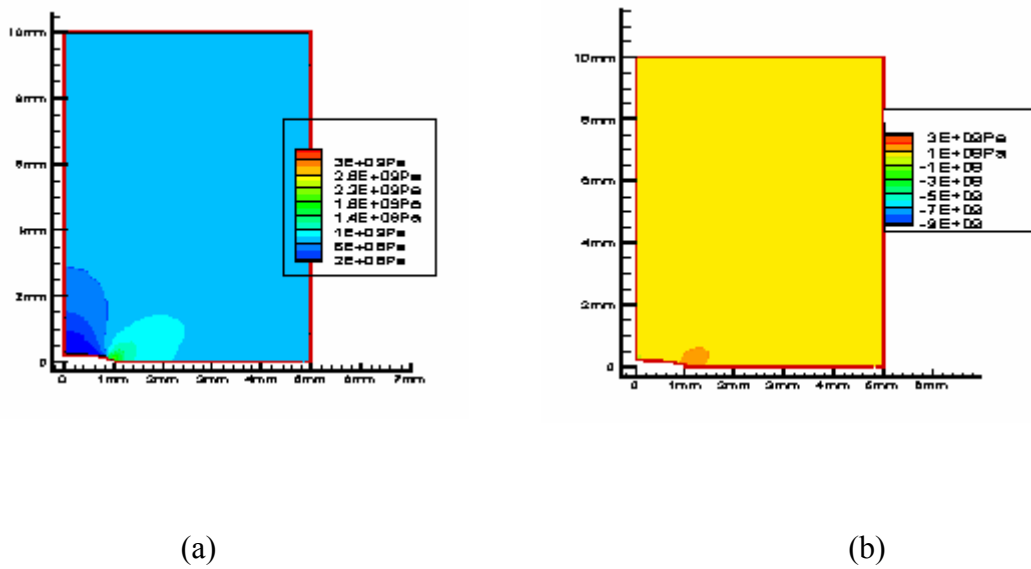
Fig 13: Contour plots of (a) local σ_{22} stress and (b) effective σ_{22} stress for characteristic length scale=50microns.
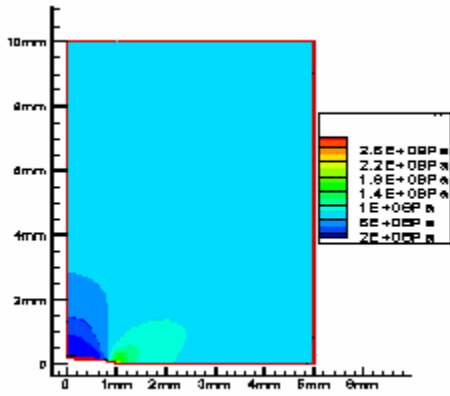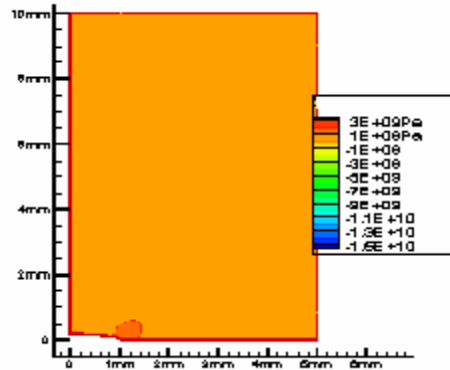
(a)   (b)

Fig 14: Contour plots of (a) local σ_{22} stress and (b) effective σ_{22} stress for characteristic length scale=70microns.
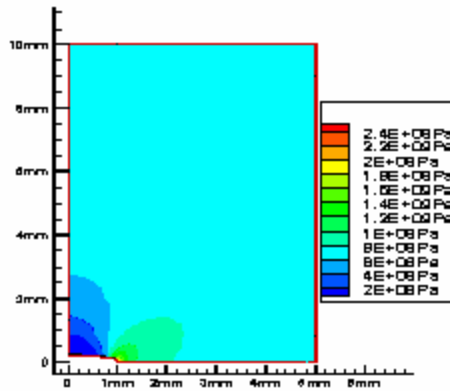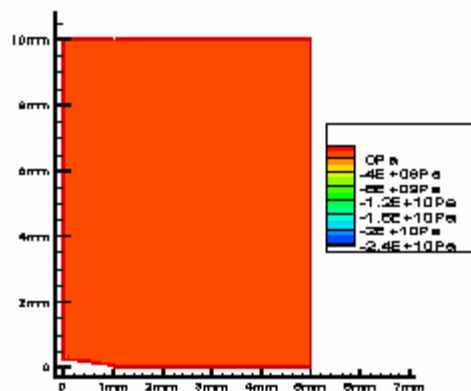
(a)   (b)

Fig 15: Contour plots of (a) local σ_{22} stress and (b) effective σ_{22} stress for characteristic length scale=100microns.

4.2) Bi-material interface crack

Bi-material interface crack is a crack sandwiched between two different materials. A problem of bi-material interface crack under mode-I loading is considered in this section. The geometry and boundary conditions, materials used are discussed in the following two subsections. The results of mesh sensitivity analysis and the effect of characteristic length scale are presented in the following sections. In section (4.3), the problem of crack normal to the bi-material interface and 100 microns away is discussed.

4.2.1) Geometry and Boundary Conditions

The geometry and boundary conditions of the bi-material problem domain are pictorially presented in the Fig.10 below. The Fig. shown below is one-half of a square tensile composite panel (10x10) with a crack at the bi-material interface. As the geometry, BC's and loading are symmetric about the y-axis, only one-half is considered for analysis. The boundary portions AG & DE are prevented from moving in the positive x-direction. The boundary part AB is fixed and the boundary portion GFE is traction free. The specimen is pulled by applying load along DC by displacing the surface uniformly by 0.01mm. With regard to the higher-order boundary conditions, the strain gradient normal to the boundary is prescribed to be zero on the entire boundary.
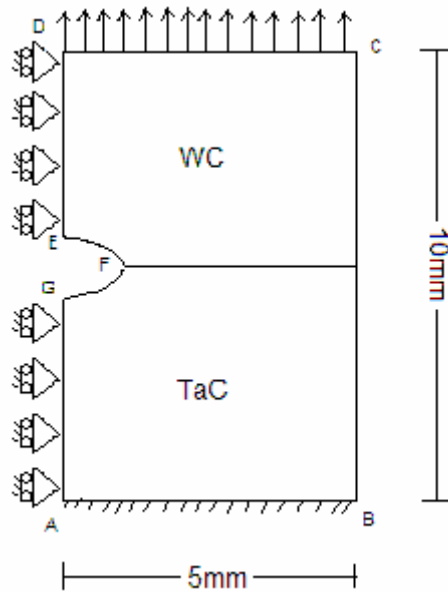
Fig16: Problem Description: Geometry and Boundary conditions

4.2.2) Materials

The materials used for the simulation of Bi-material interface crack are Tungsten carbide

and Tantalum carbide. Tungsten carbide is a brittle isotropic elastic material with

Young's modulus $(E = 680 * 10^9 \, N/m^2)$ and Poisson's ratio $(v = 0.25)$. Tantalum carbide

is also a brittle isotropic material with Young's modulus $\left(E = 480 * 10^9 \, N/m^2\right)$ and

Poisson's ratio $(v = 0.24)$. When a composite body consisting of two isotropic and elastic

materials is loaded by prescribed surface tractions, the stress field depends on three

parameters formed from the combinations of elastic constants. But, when the loading and

geometry is such that the body is in a state of plane deformations, the stress field induced

by the prescribed tractions is dependent on only two parameters formed from the

combinations of elastic constants. These parameters are named after professor J Dundurs

as Dundurs parameters [16]. The Dundurs parameter α is defined as

$$\alpha = \frac{\mu_1(\kappa_2 + 1) - \mu_2(\kappa_1 + 1)}{\mu_1(\kappa_2 + 1) + \mu_2(\kappa_1 + 1)} \qquad \text{-------------------- (4.2)}$$

The parameter α for this particular combination of materials is 0.175. α measures the mismatch in the in plane tensile modulus across the interface.

The Dundurs parameter β is defined as

$$\beta = \frac{\mu_1(\kappa_2 - 1) - \mu_2(\kappa_1 - 1)}{\mu_1(\kappa_2 + 1) + \mu_2(\kappa_1 + 1)} \qquad \text{---------------------- (4.3)}$$

The parameter β for this particular combination of materials is 0.064. β measures the mismatch in the in plane bulk modulus.

4.2.3) Mesh Sensitivity analysis

Mesh Sensitivity analysis is a process of refining the mesh to achieve a converged solution. This section presents the results of mesh sensitivity analysis for four different meshes as shown in the Fig. 17(a)-(d) with mesh1 being the coarse and mesh4 being the finest. As it can be seen, the mesh is designed such that it is fine at the crack tip. The length scale used for this analysis is 100 micrometers. The results of mesh sensitivity analysis for the structure of crack tip, local stress and Effective stress are presented in the Figs. 17-22.

4.2.3.1) Displacement plots

The structure of crack tip is a plot of vertical displacement of the crack face verses distance along the crack face. The following graphs shows the structure of crack tip for four different meshes (see Fig. 17(a)-(d)) with mesh1 being the coarse and mesh4 being the finest. It can be easily observed that the response is independent of the mesh size.
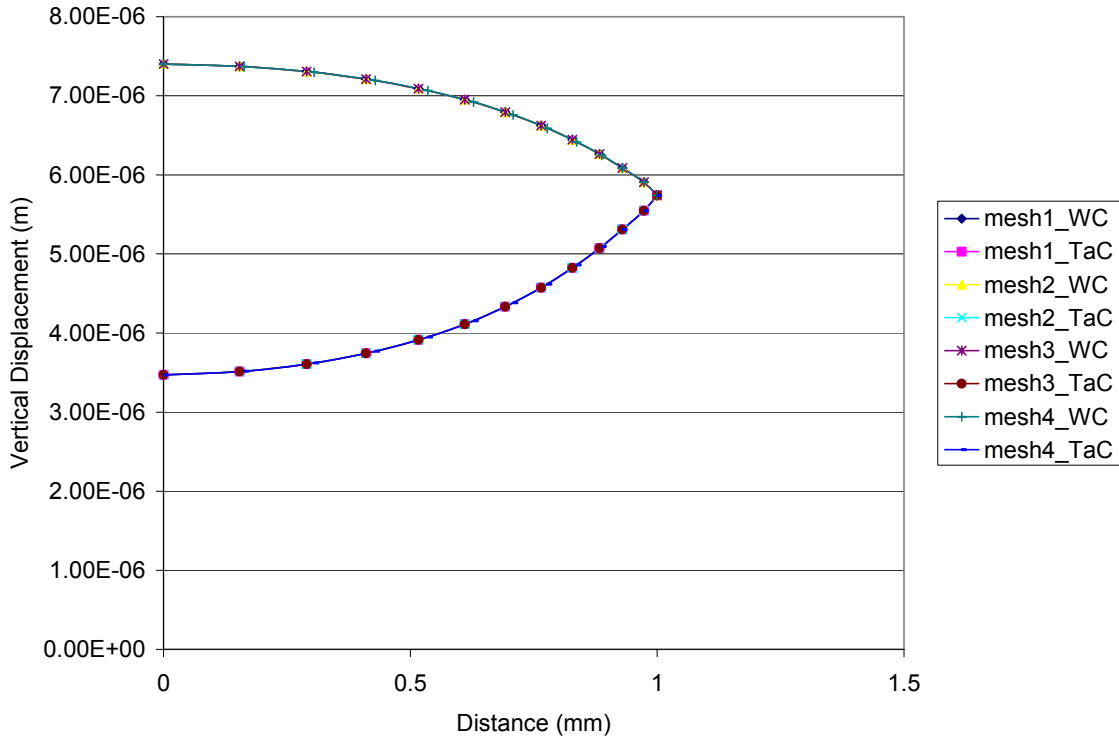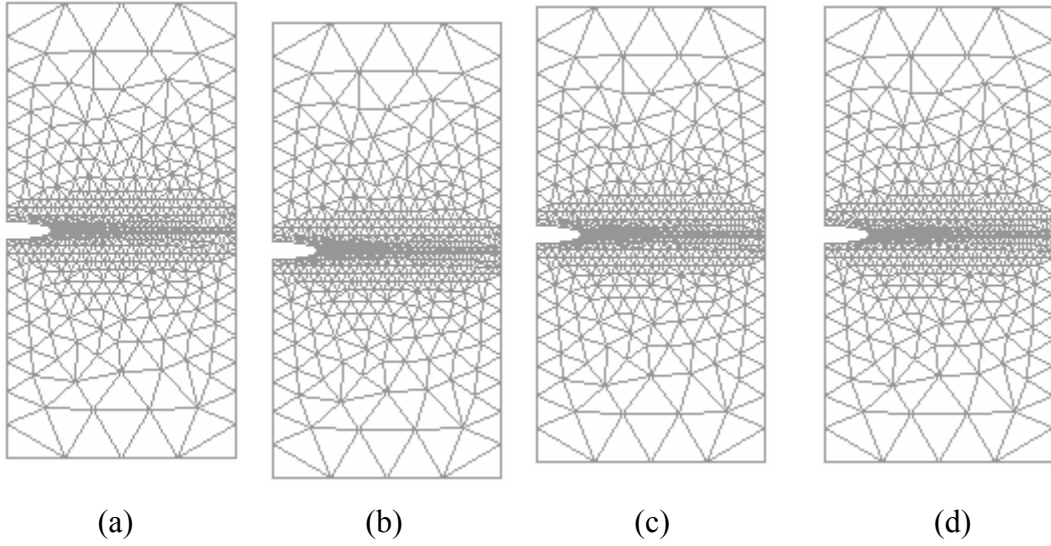
Fig 17 (a) mesh1 (b) mesh2 (c) mesh3 (d) mesh4
(e) Mesh Sensitivity of Structure of Crack tip

4.2.3.2) Stress plots

As the bi-material interface belongs to both materials at the same time, the stresses are plotted along F'H' and F''H'' close to the interface as shown in the Fig. 18.

In this sub-section, the local as well as effective stress plots for four different meshes as shown in the Fig. 17(a)-(d), with mesh1 being the coarse and mesh4 being the finest, are presented in the Figs. 19-22.
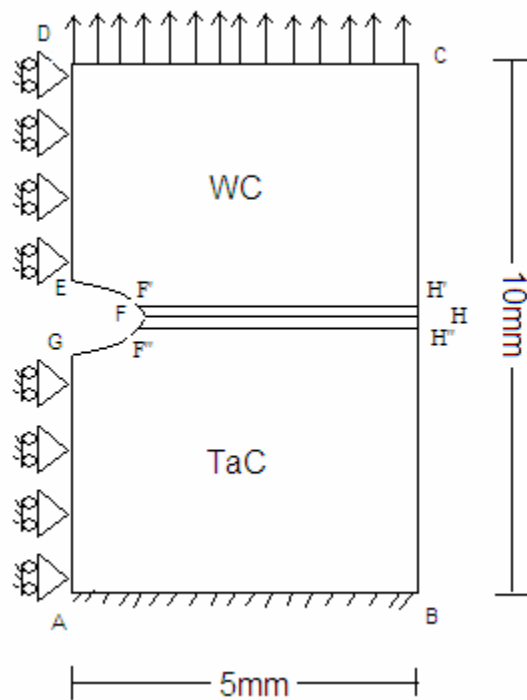
Fig 18: Problem Description

4.2.3.2.1) Local Stress plot

The term local stress represents the stress computed from only the first term of the constitutive law (see equation (4.1b)) as described in the homogeneous case. The following two graphs show the plots of local σ_{22} stress component along the line F'H' in WC material. The graph shows the result for four different meshes as shown in the Fig.

17(a)-(d). It can be easily noticed that the response is independent of the mesh size. Fig. 19(b) is a magnified image of Fig. 19(a) at the crack tip.

WC

(a)

WC
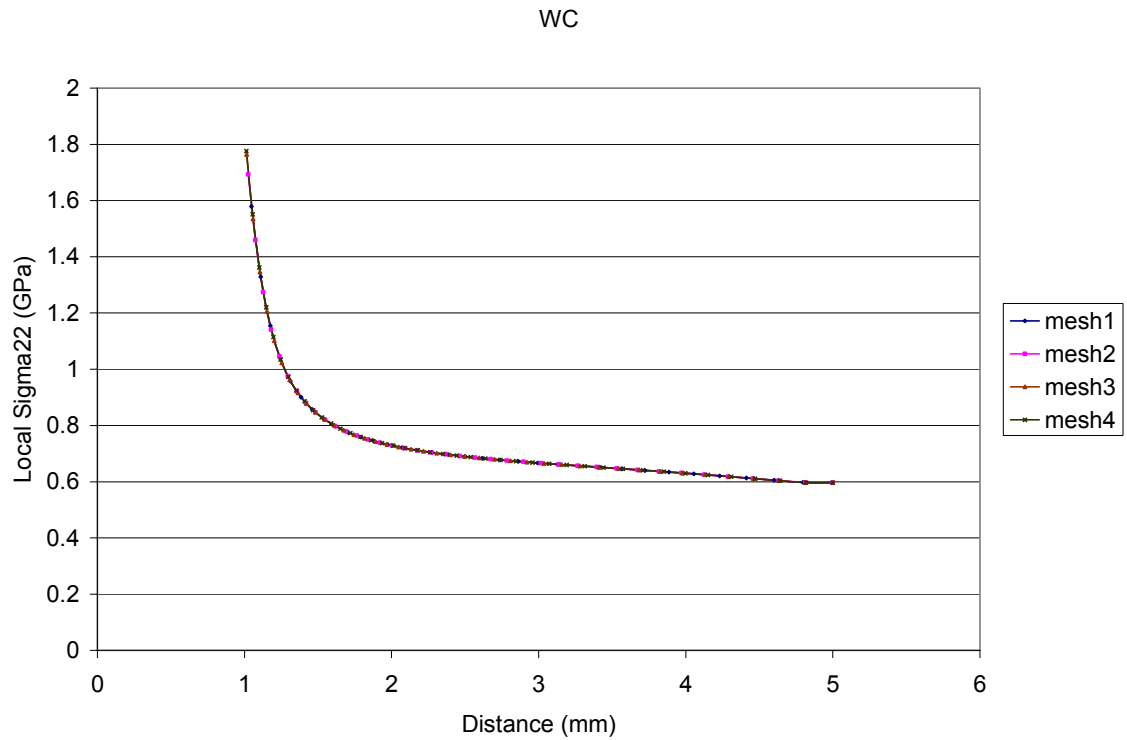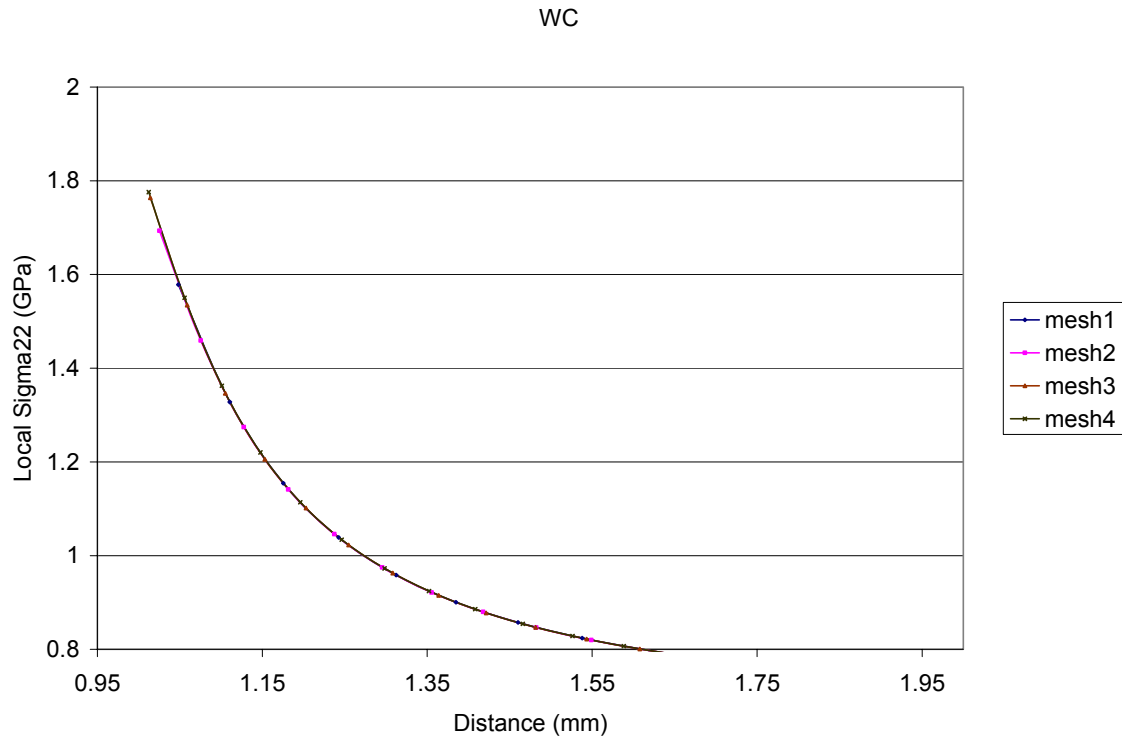
(b)
Fig 19 (a) Mesh Sensitivity of Local σ_{22} stress component
(b) Magnified image of the plot near the crack tip

The following two graphs show the plots of local σ_{22} stress component along the line F''H'' in TaC material. The graph shows the result for four different meshes as shown in the Fig. 17(a)-(d). It can be easily noticed that the response is independent of the mesh size. Fig. 20(b) is a magnified image of Fig. 20(a) at the crack tip.

TaC

(a)

TaC

(b)
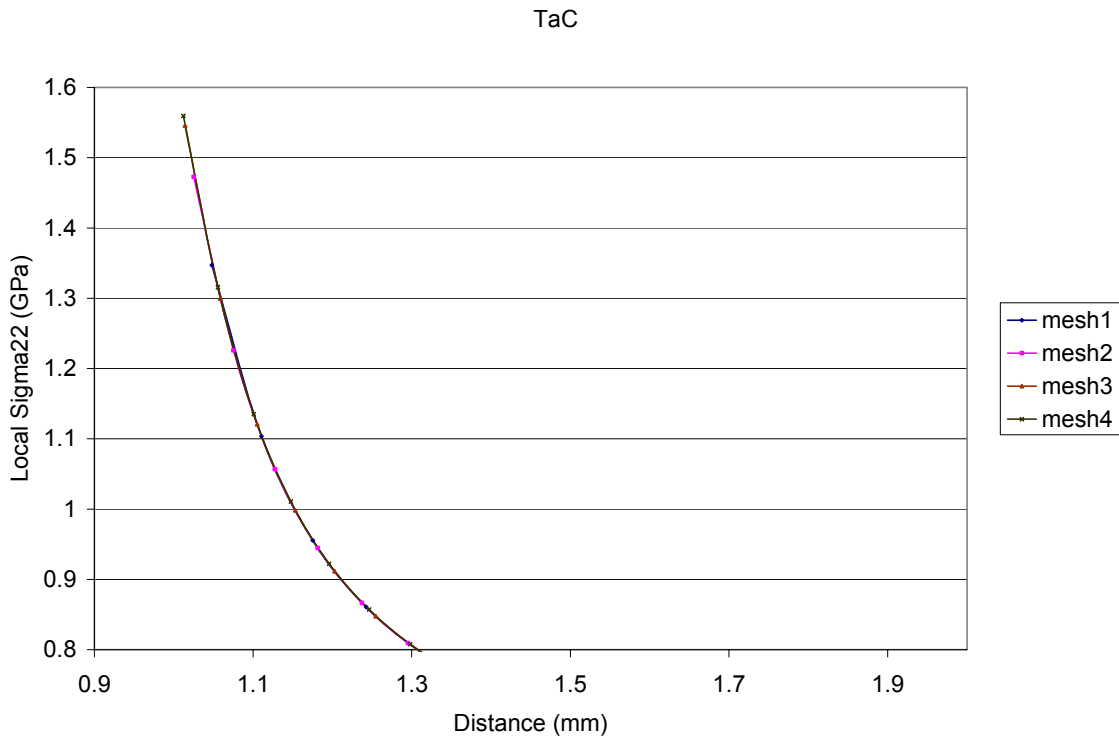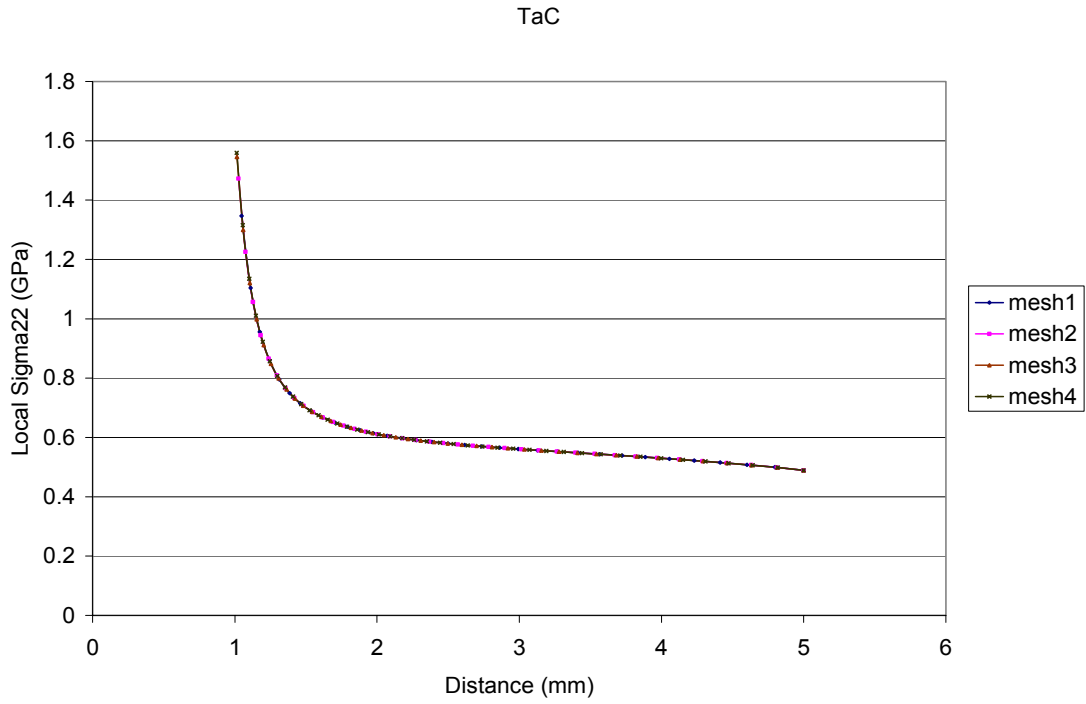
Fig 20 (a) Mesh Sensitivity of Local σ_{22} stress component
(b) Magnified image of the plot near the crack tip

4.2.3.2.2) Effective Stress plot

The term effective stress represents the stress computed from equation (4.1a) as described in the homogeneous case. The following two graphs show the plots of effective σ_{22} stress component along the line F'H' in WC material. The graph shows the result for four different meshes as shown in Fig. 17(a)-(d). It can be easily noticed that the response is independent of the mesh size. Fig. 21(b) is a magnified image of Fig. 21(a) at the crack tip
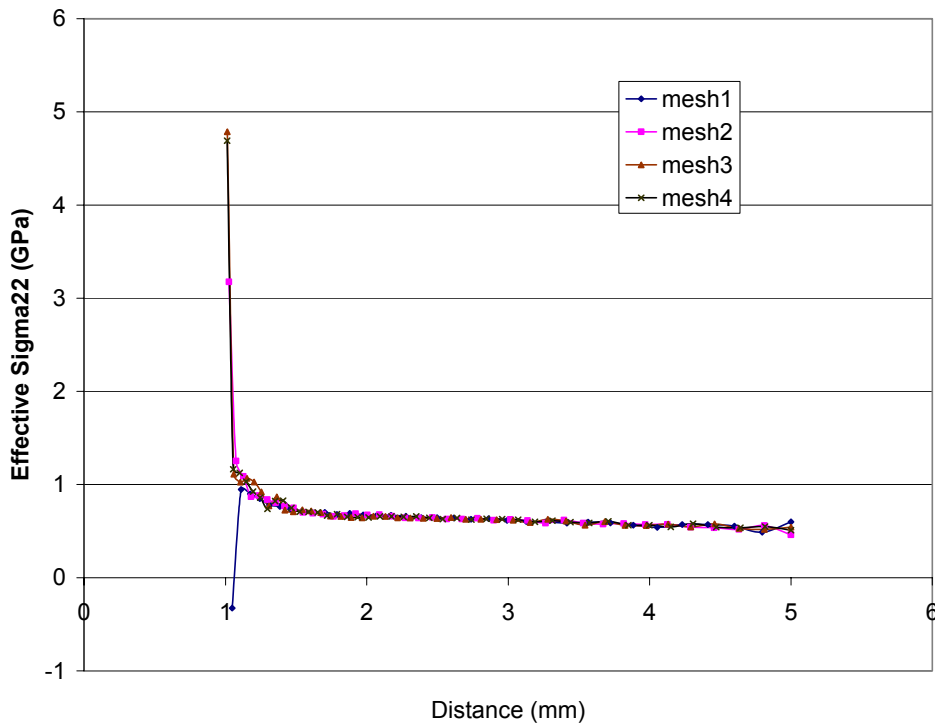
(a)
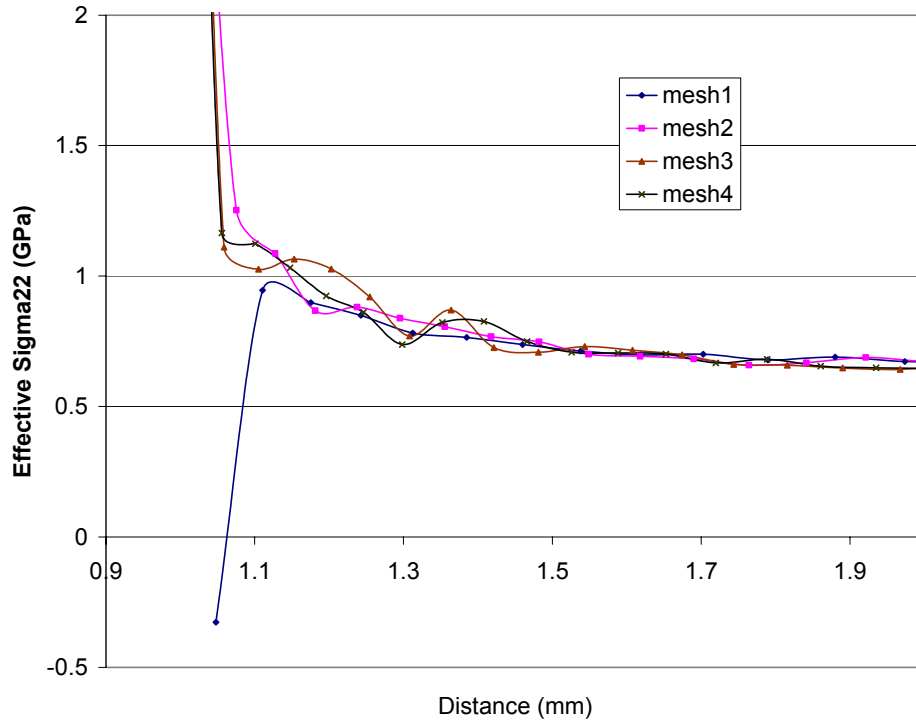
(b)
Fig 21 (a) Mesh Sensitivity of Effective σ_{22} stress component
(b) Magnified image of the plot near the crack tip.

The following two graphs show the plots of effective σ_{22} stress component along the line F''H'' in TaC material. The graph shows the result for four different meshes as shown in Fig. 17(a)-(d). It can be easily noticed that the response is independent of the mesh size. Fig. 22(b) is a magnified image of Fig. 22(a) at the crack tip
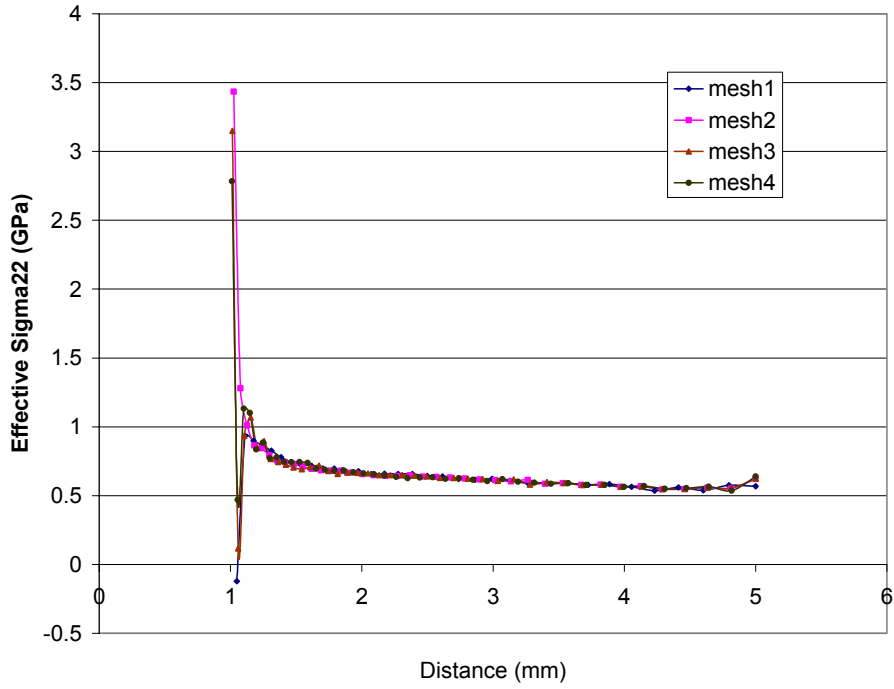
(a)
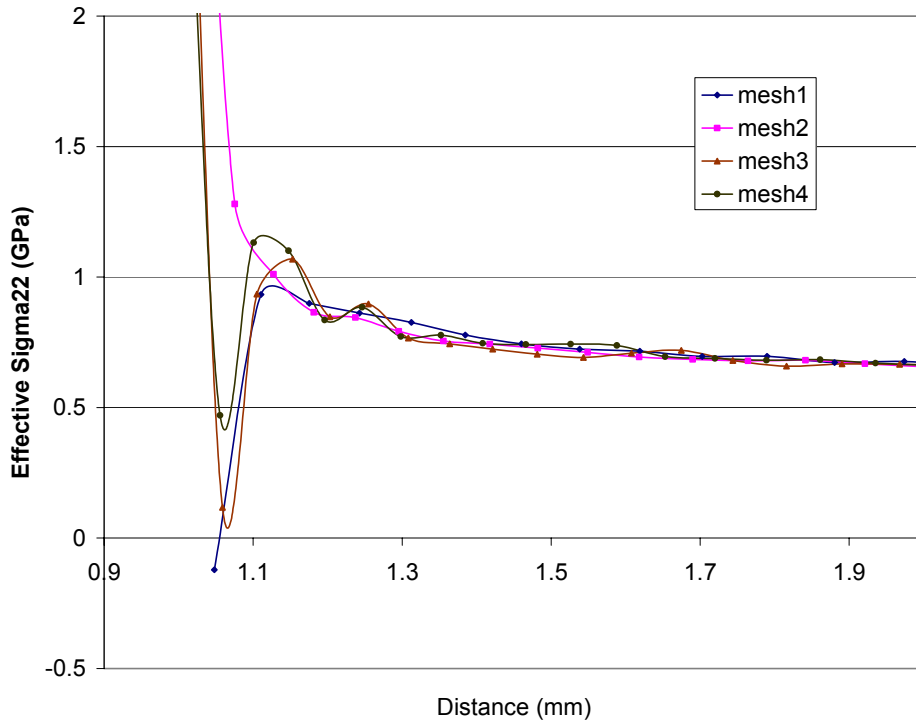
(b)

Fig 22 (a) Mesh Sensitivity of Effective σ_{22} stress component
(b) Magnified image of the plot near the crack tip

4.2.4) Effect of characteristic length scale

The length scale is considered as the spatial span over which the non-local interactions are taken into account. The effect of length scale on the structure of crack tip, local as well as effective stresses are presented in the Figs. 23-31. The unit of the length scale in the legend of the following graphs is micrometers.

4.2.4.1) Displacement plots

The structure of crack tip is a plot of vertical displacement verses distance along crack face. The following two graphs show the effect of length scale on the structure of crack tip for 30, 50, 70&100 micrometers and also compared with classical solution. Fig. 23(b) is a magnified image of the Fig. 23(a) near the crack tip.
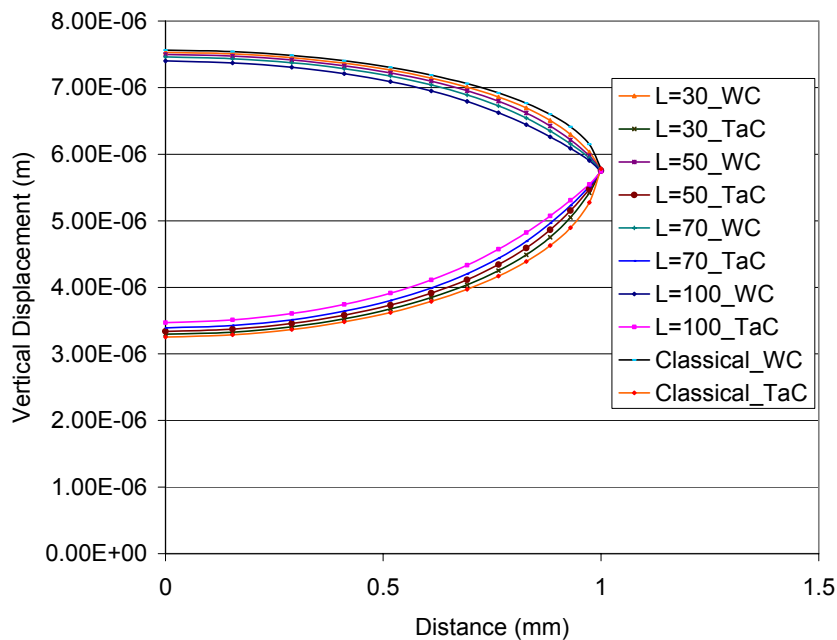

(a)
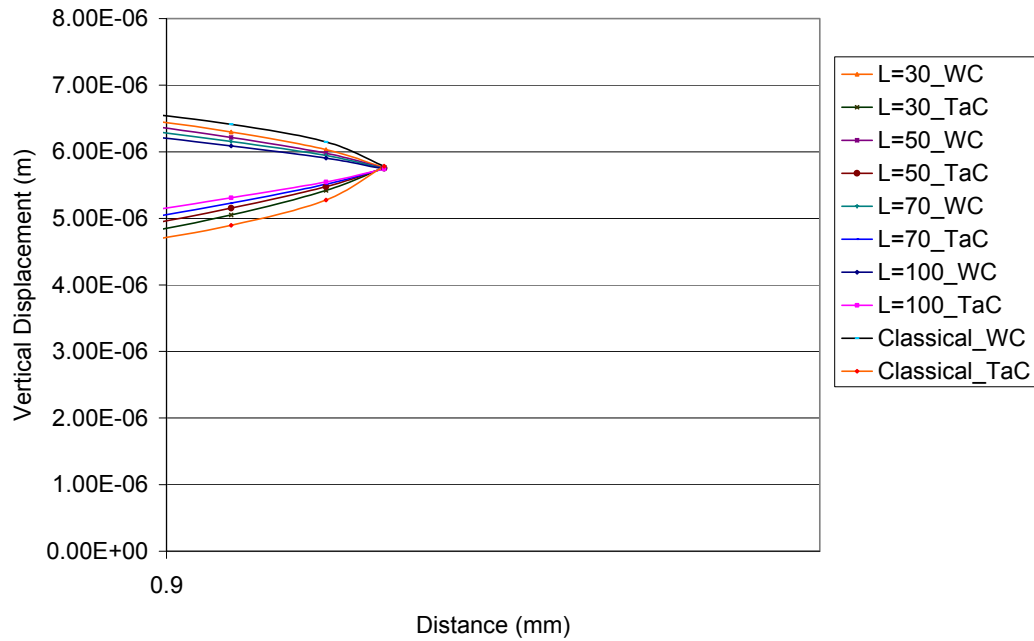
(b)
Fig 23 (a) Effect of characteristic length scale (*l*) on structure of crack tip
(b) Magnified image of the plot near the crack tip

4.2.4.2) Stress plots

4.2.4.2.1) Local Stress plots

The term local stress represents the stress computed from only the first term of the constitutive law (see equation (4.1b)) as described in the homogeneous case. The following two Fig. 24 show the plots of local σ_{22} stress component along the line F'H' in WC material. The graph shows the effect of length scale on the local σ_{22} stress component for 30, 50, 70&100 micrometers and compared with classical solution. As it can be seen, the crack tip stress decreases as the length scale is increased. Fig. 24(b) shows a magnified view of the plots near the crack tip.
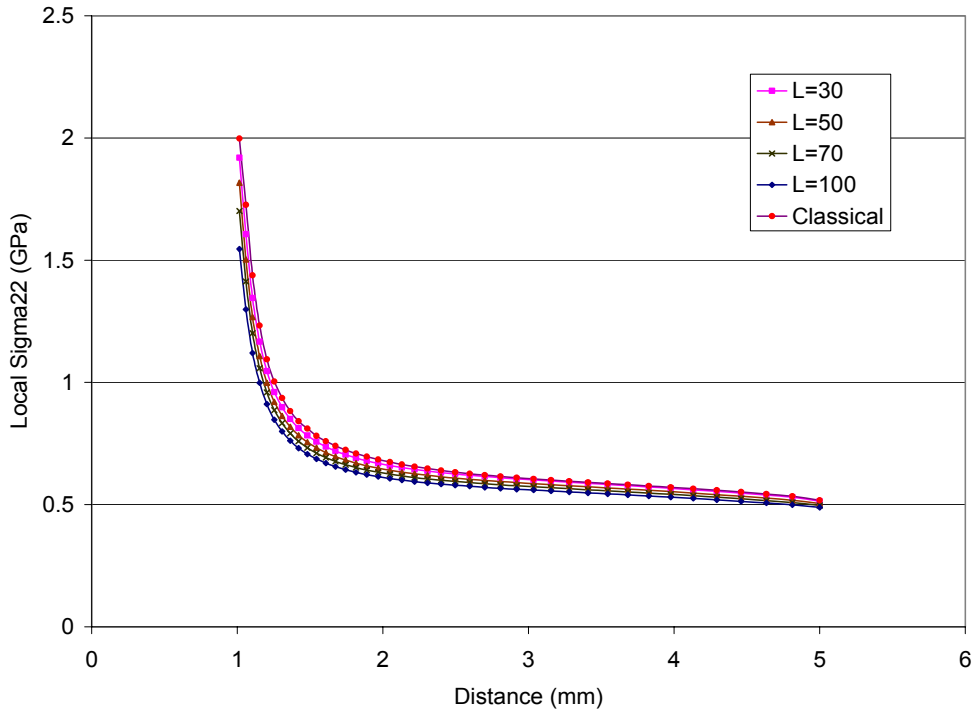
(a)
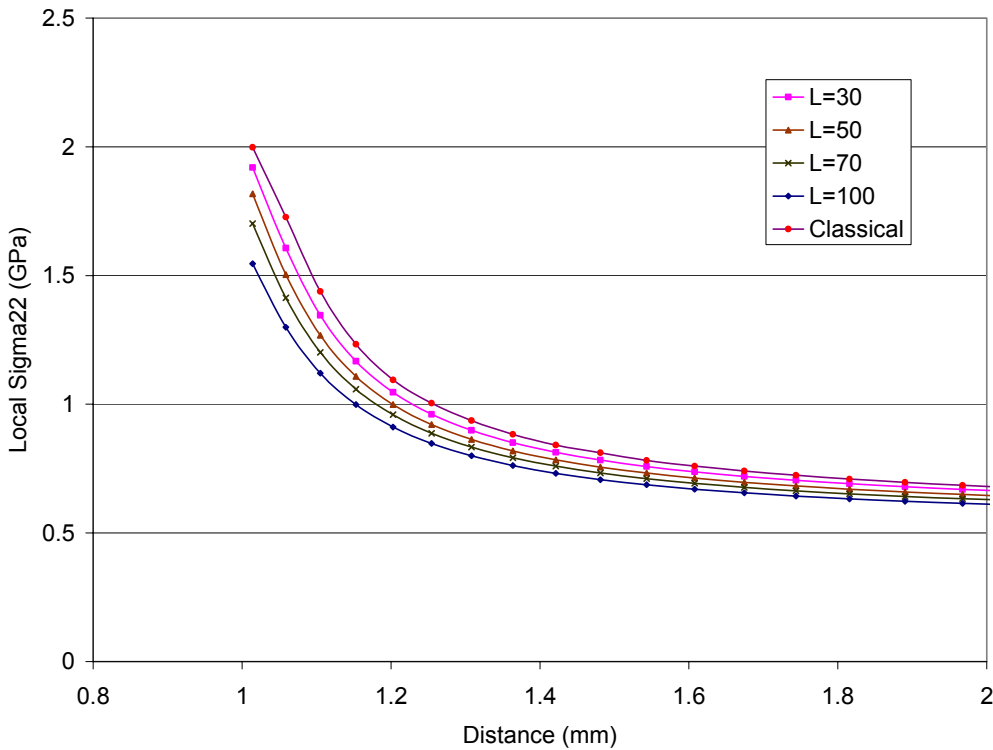
(b)

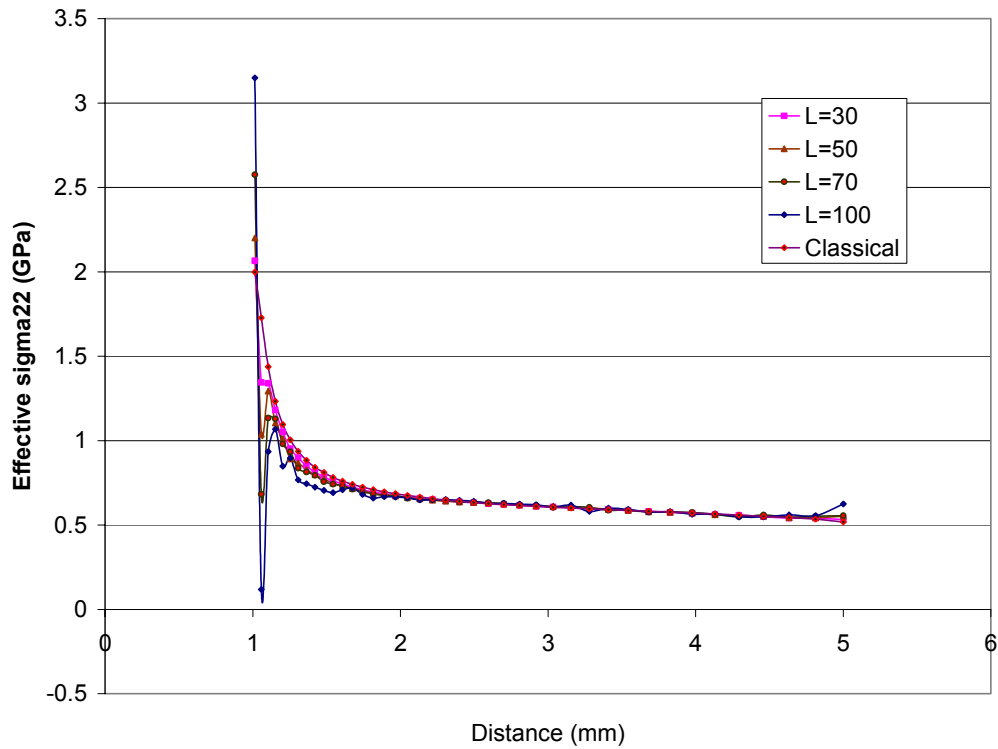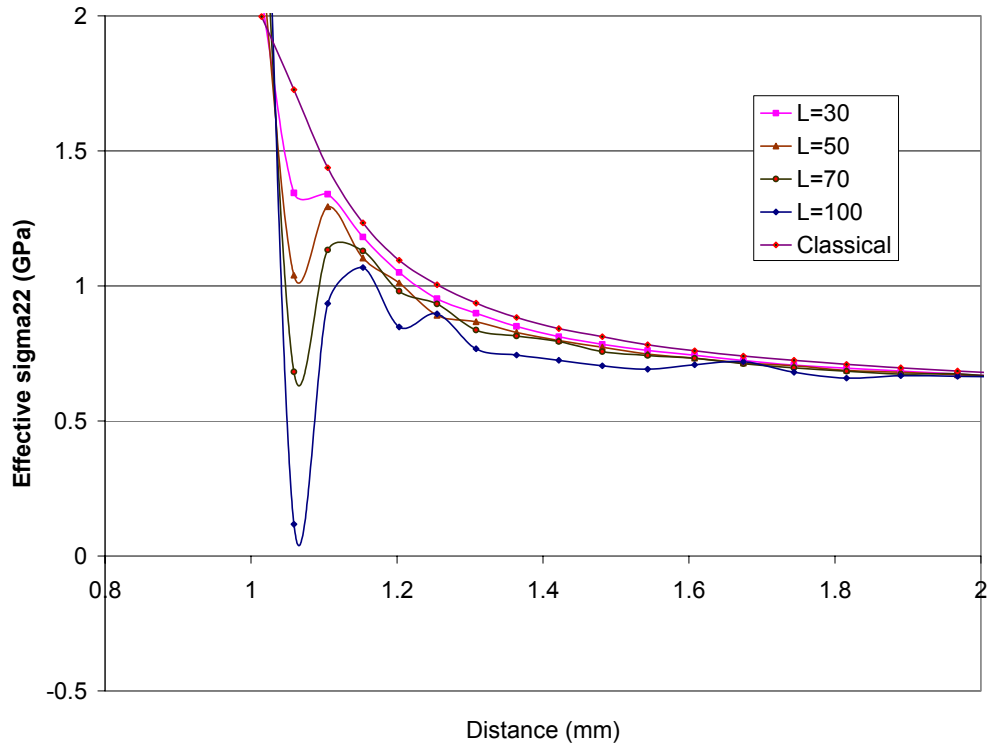Fig 24 (a) Effect of characteristic length scale (*l*) on local σ_{22} stress component
(b) Magnified image of the plot near the crack tip

The term local stress represents the stress computed from only the first term of the constitutive law (see equation 4.1(b)) as described in the homogeneous case. The following two Fig 25 show the plots of local σ_{22} stress component along the line F''H'' in TaC material. The graph shows the effect of length scale on the local σ_{22} stress component for 30, 50, 70&100 micrometers and compared with classical solution. As it can be seen, the crack tip stress decreases as the length scale is increased. Fig. 25(b) shows a magnified view of the plots near the crack tip.
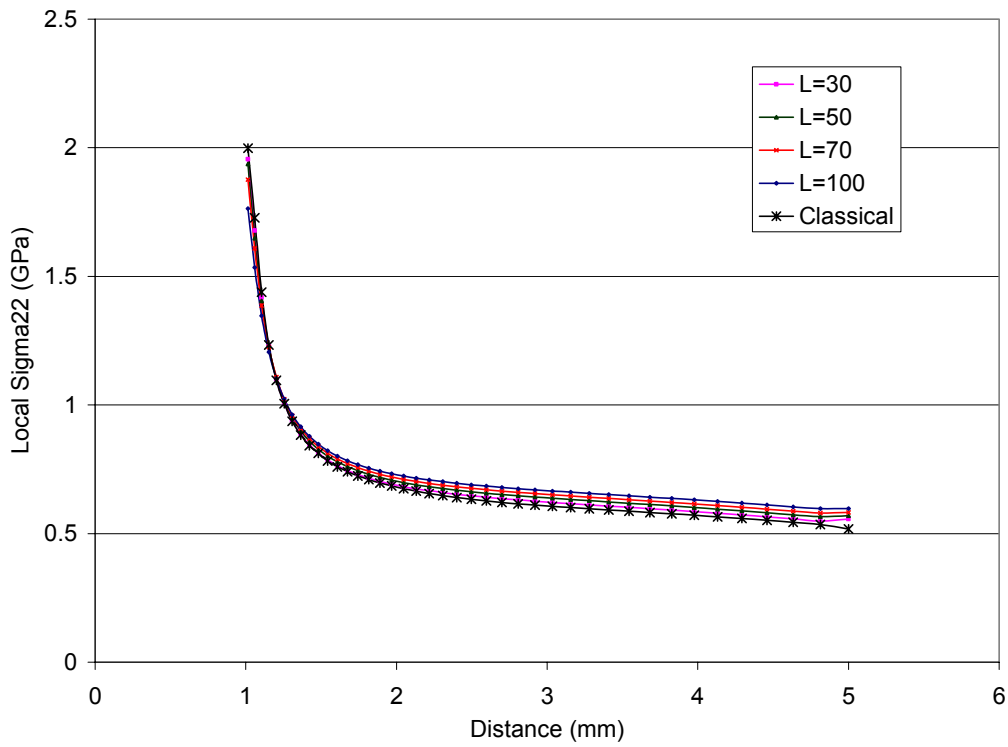
(a)
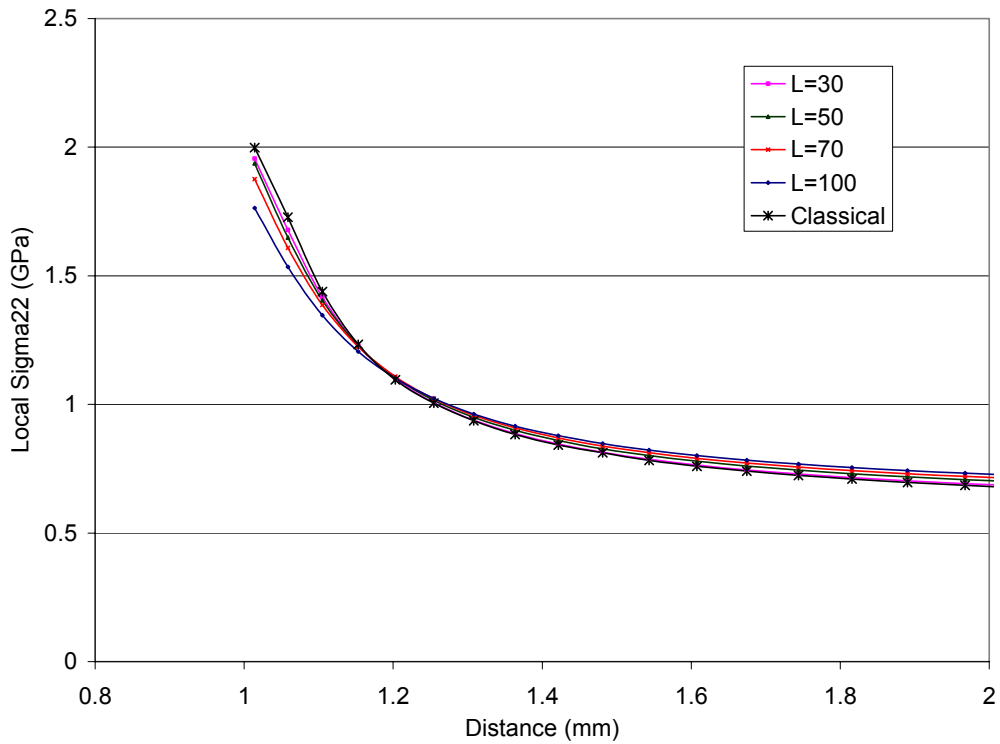
(b)

Fig 25(a) Effect of characteristic length scale (*l*) on local σ_{22} stress component
(b) Magnified image of the plot near the crack tip

4.2.4.2.2) Effective stress plots

The term effective stress represents the stress computed from the equation (4.1a) as described in the homogeneous case. The following Fig 26 show the plots of effective σ_{22} stress component along the line F'H' in WC material. The graph shows the effect of length scale on the local σ_{22} stress component for 30, 50, 70&100 micrometers and compared with classical solution. As it can be seen, there is a hump in the stress near the tip and this hump stress is decreased as the length scale is increased. Fig. 26(b) shows a magnified view of the plots near the crack tip.
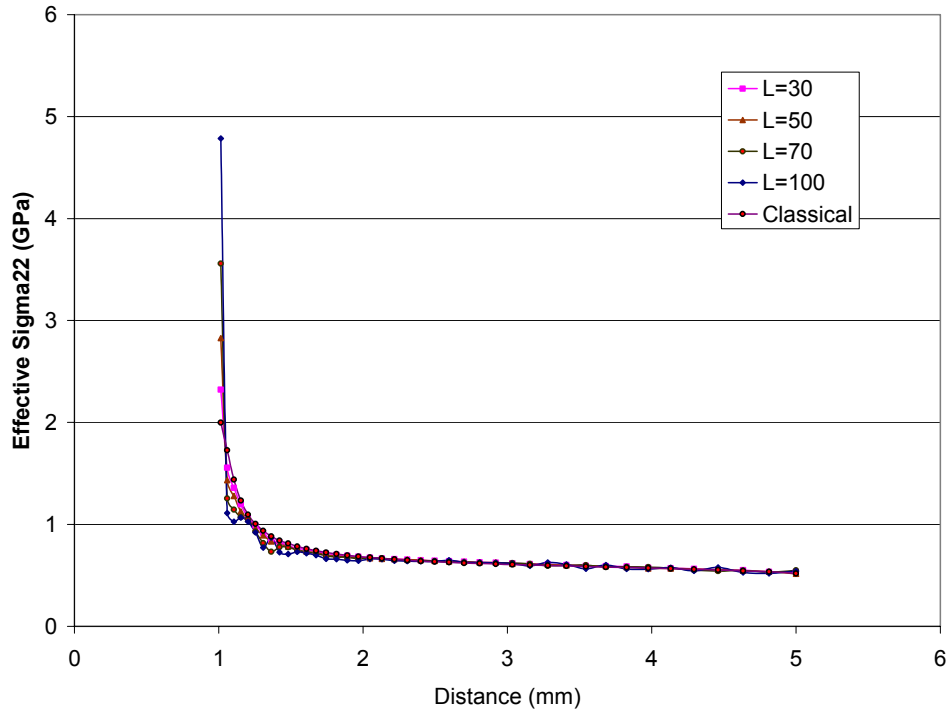
(a)
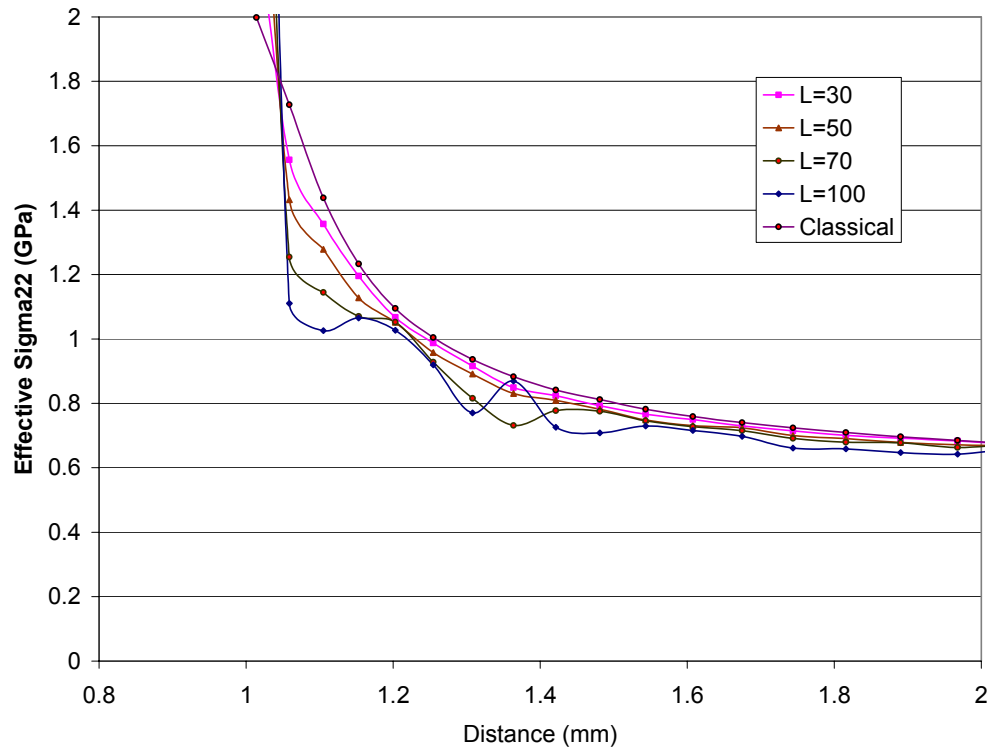
(b)

Fig 26(a) Effect of characteristic length scale (l) on effective σ_{22} stress component
(b) Magnified image of the plot near the crack tip

74

The term effective stress represents the stress computed from the equation (4.1a) as described in the homogeneous case. The following Fig. 27 shows the plots of effective σ_{22} stress component along the line F''H'' in TaC material. The graph shows the effect of length scale on the local σ_{22} stress component for 30, 50, 70&100 micrometers and compared with classical solution. As it can be seen, there is a hump in the stress near the tip and this hump stress is decreased as the length scale is increased. Fig. 27(b) shows a magnified view of the plots near the crack tip.

(a)

(b)

Fig 27 (a) Effect of characteristic length scale (*l*) on Effective σ_{22} stress component
(b) Magnified image of the plot near the crack tip

4.2.4.2.3) Double stress gradient plots

The constitutive law of gradient elasticity can also be written as

$$\tilde{\sigma}_{ji} = \sigma_{ji} - \mu_{kji,k} \qquad \text{------------ (4.2)}$$

where

$\tilde{\sigma}_{ji}$ is the effective stress

σ_{ji} is the local stress which is comparable to classical stress

$\mu_{kji,k}$ is the double stress gradient

The following two Figs. 28 and 29 show the plots of double stress gradients for various length scales plotted along the lines F''H'' and F'H' respectively (see Fig. 18).
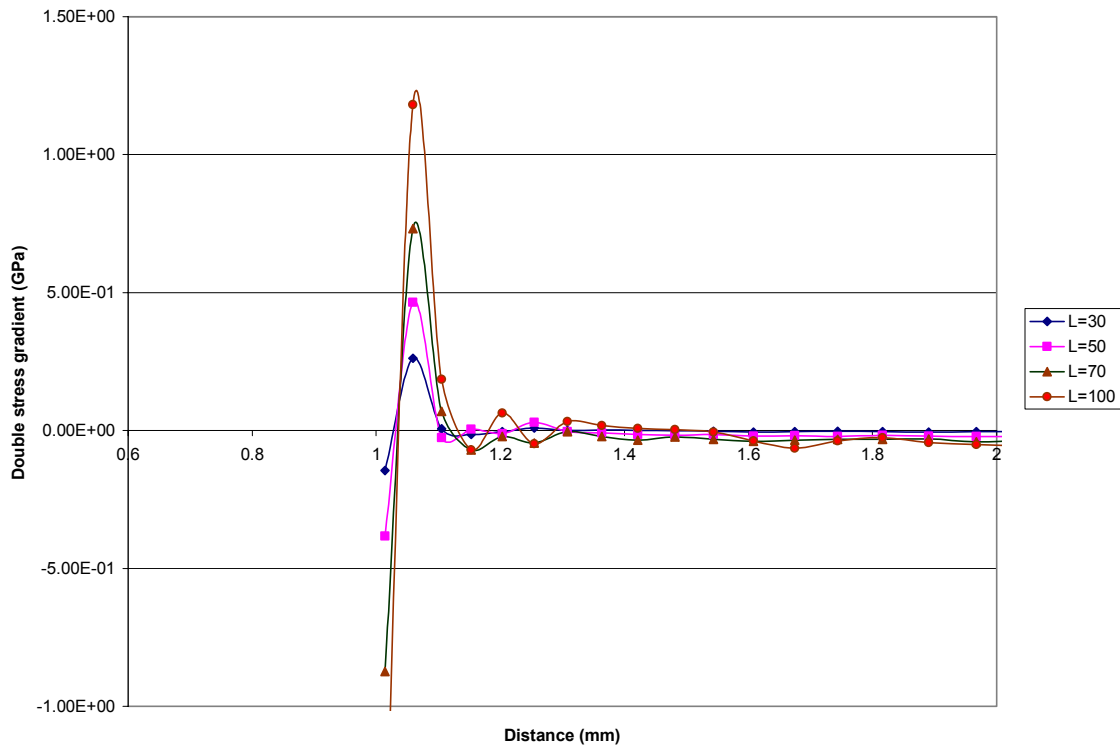
Fig 28: Plot of Double stress gradient for various length scales plotted along F''H''
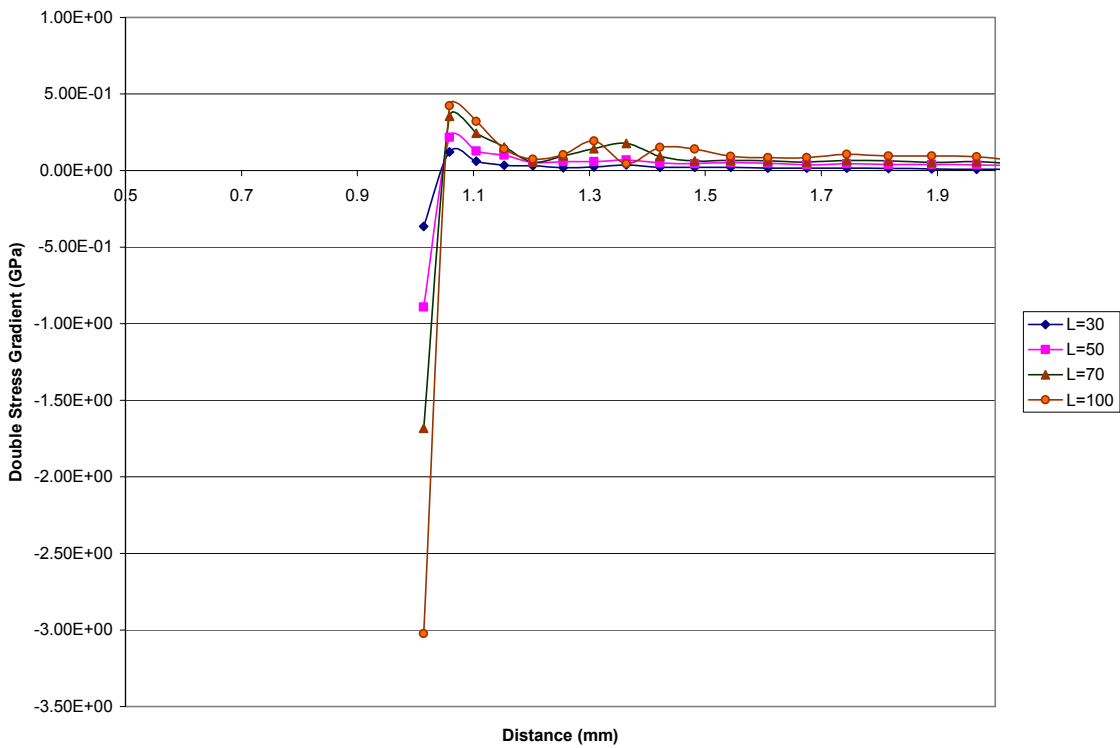
Fig 29: Plot of Double stress gradient for various length scales plotted along F'H'

As it can be seen from the above Figs., the fluctuations in the effective stress are a cause of the double stress gradient. The spatial fluctuations of double stress gradient can be interpreted as moments which are the result of introduction of a new kinematic variable (that is strain gradient). This interpretation is analogous to the couple stress in cosserat couple stress theory which has curl of strain as the additional kinematic variable.

4.2.4.2.4) Local Shear Stress plots

As the specimen is made up of two different materials, there exists a conflict in deformation in the transverse direction which results in shear stress and Mode-II type deformation. The following Fig 30 represent the local shear stress plotted along F'H' in WC material for 30, 50, 70&100 micrometers and are compared with classical solution. Fig. 30(b) shows a magnified view of the plots near the crack tip.
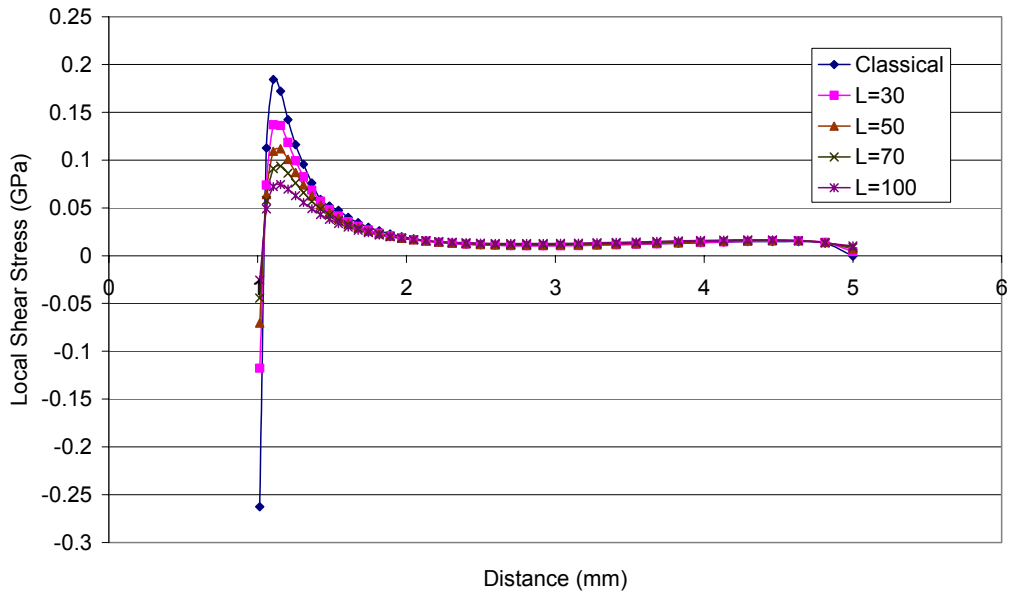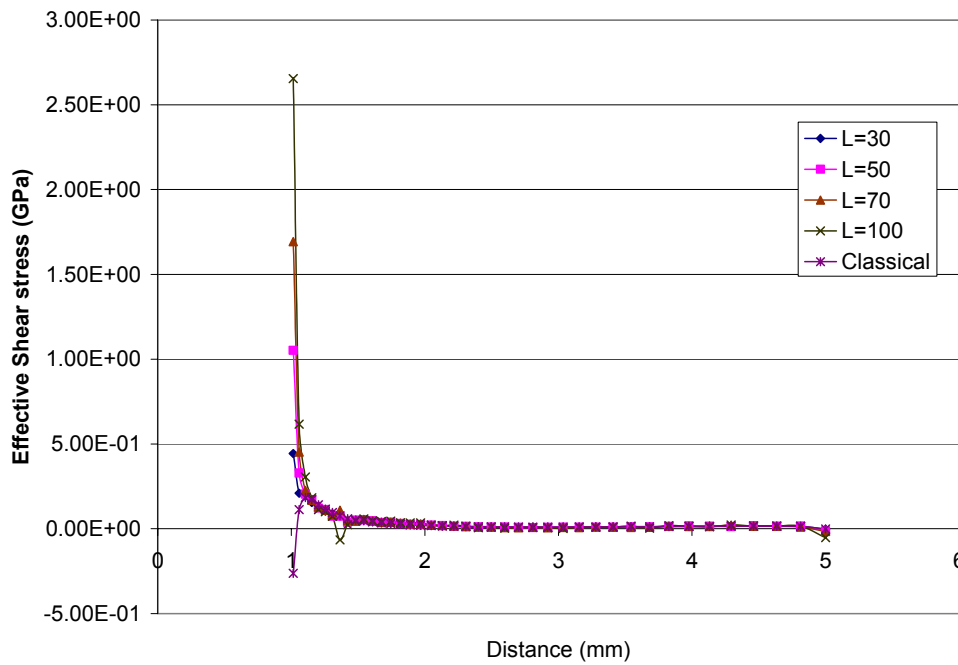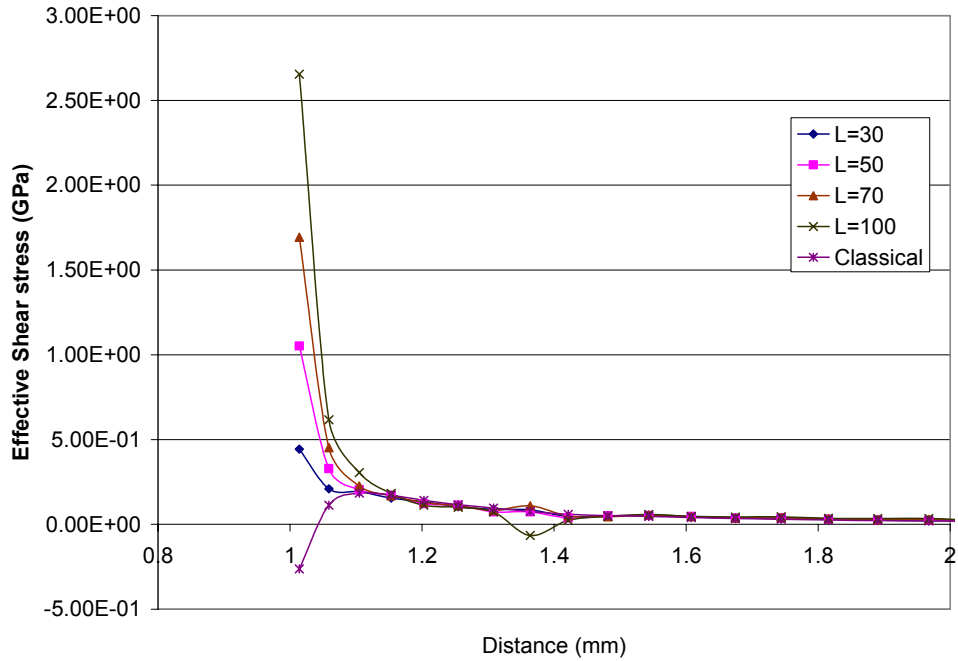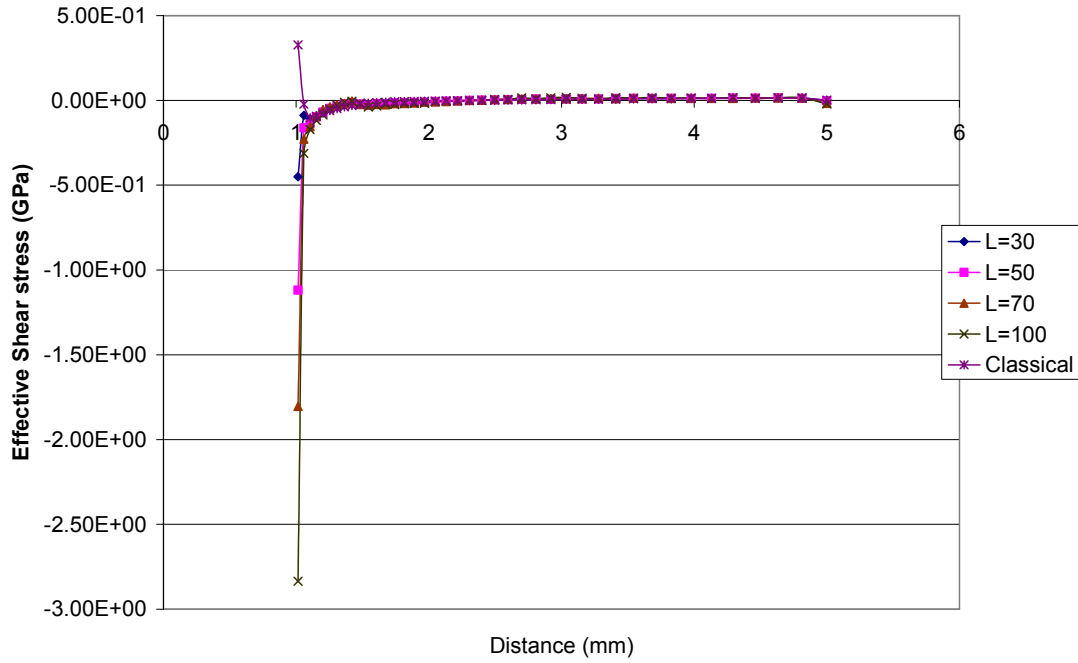
(a)
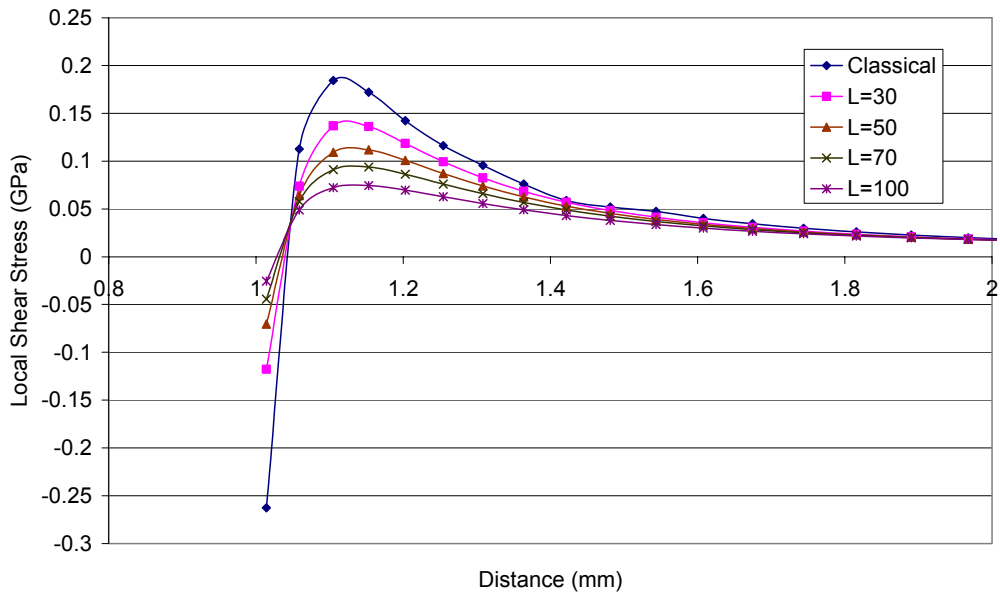
(b)

Fig 30 (a) Effect of length scale (*l*) on local Shear Stress plots
(b) Magnified image of the plot near the crack tip

The following Fig 31 represents the local shear stress plotted along F''H'' in TaC material for 30, 50, 70&100 micrometers and are compared with classical solution. Fig. 31(b) shows a magnified view of the plots near the crack tip
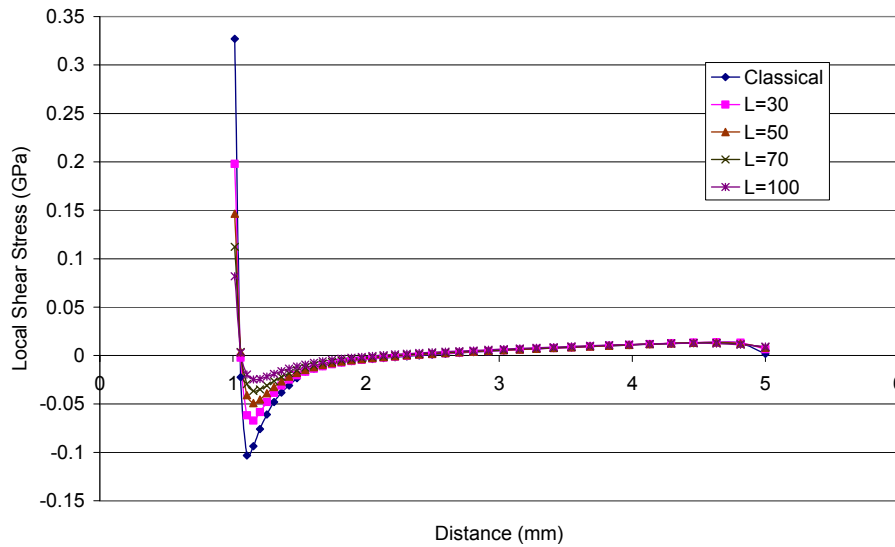
(a)
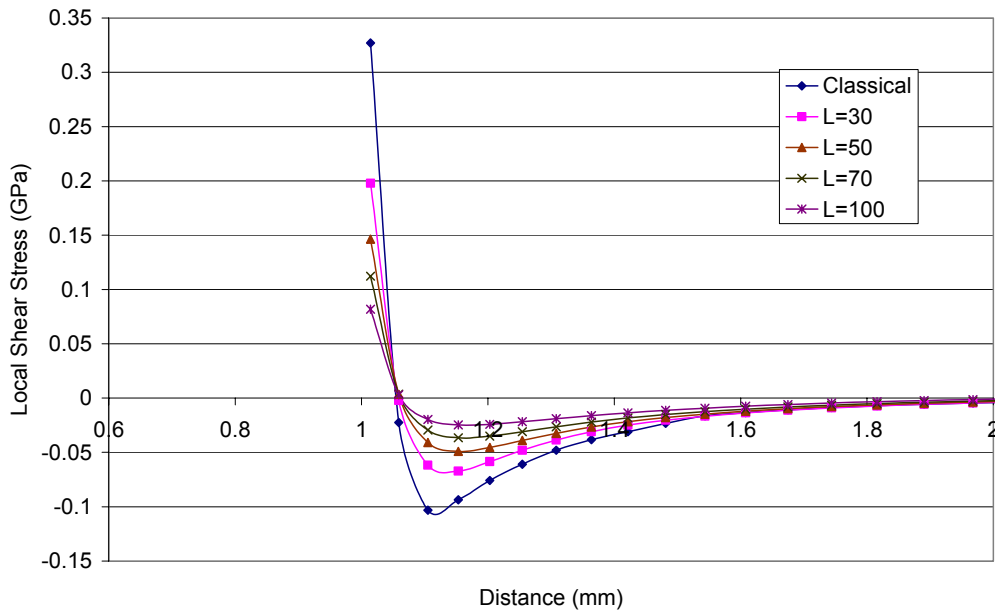
(b)

Fig 31(a) Effect of length scale (*l*) on local Shear Stress plots
(b) Magnified image of the plot near the crack tip

4.2.4.2.4) Effective Stress plots:

The following Fig. 32 represent the plots of effective shear stress along the line F'H' in WC material for 30, 50, 70&100 micrometers length scales. Fig. 32(b) is a magnified view of the plot at the tip
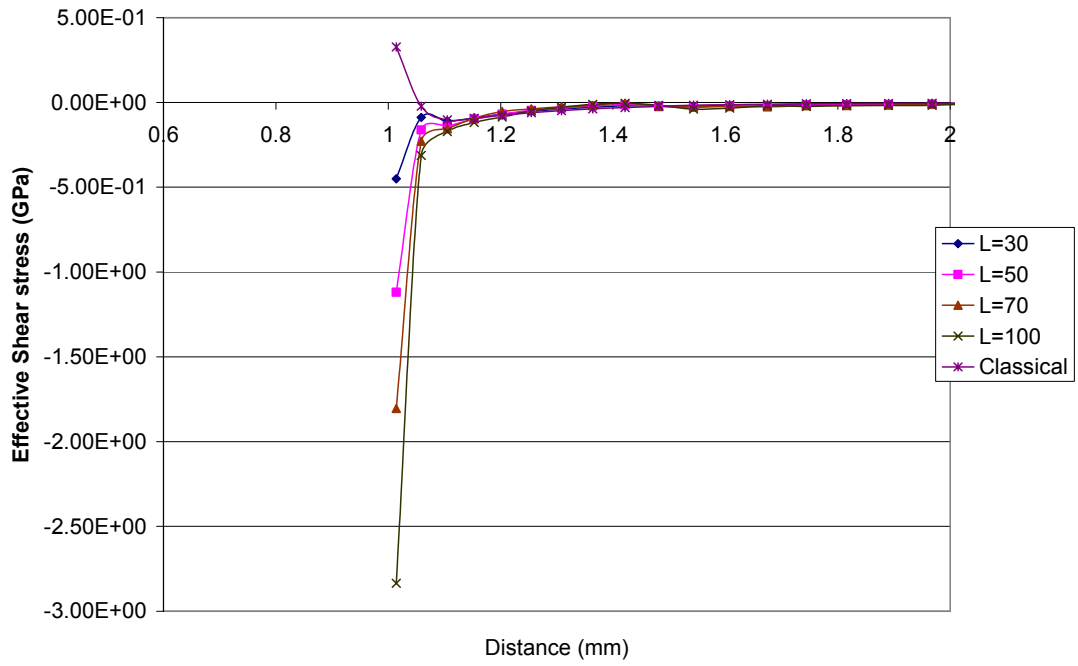

(a)

(b)

Fig 32 (a) Effect of length scale (*l*) on effective Shear Stress plots
(b) Magnified image of the plot near the crack tip

The following Fig. 33 represent the plots of effective shear stress along the line F''H'' in

TaC material for 30, 50, 70&100 micrometers length scales. Fig. 33(b) is a magnified

view of the plot at the tip.

(a)

(b)

Fig 33(a) Effect of length scale (*l*) on effective Shear Stress plots
(b) Magnified image of the plot near the crack tip

4.2.4.3) Contour Plots

In this sub-section, the contour plots of local and effective σ_{22} stress for various length scales. The Figs. 34-37 show the contour plots for characteristic length scale 30, 50, 70&100 micrometers.
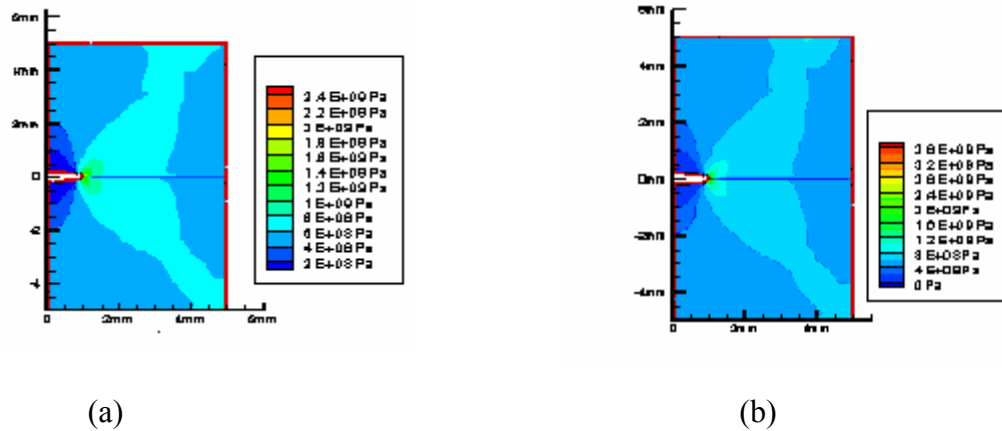

(a)   (b)

Fig 34: Contour plots of (a) local σ_{22} stress and (b) effective σ_{22} stress for characteristic length scale=30microns.
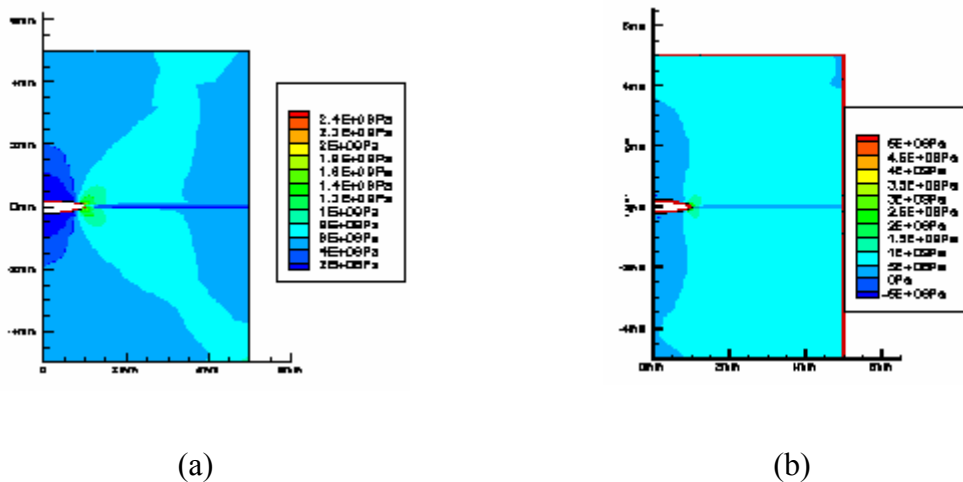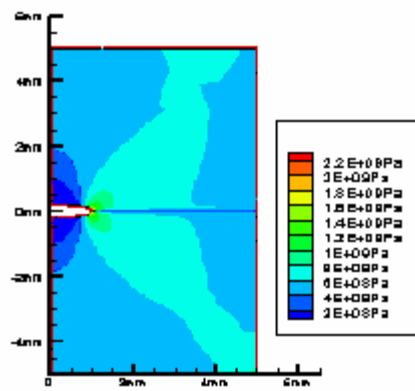

(a)   (b)

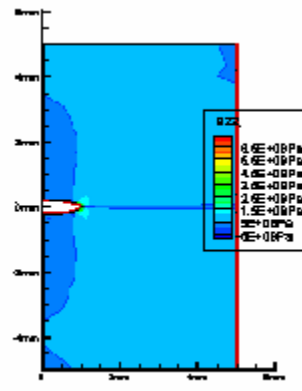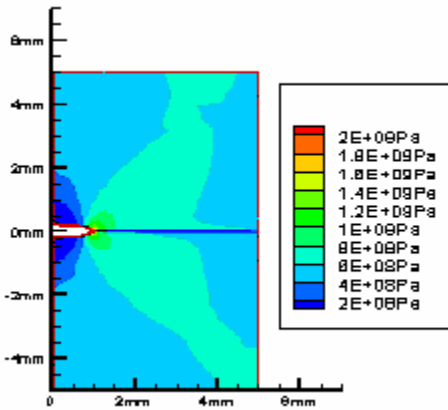Fig 35: Contour plots of (a) local σ_{22} stress and (b) effective σ_{22} stress for characteristic length scale=50microns

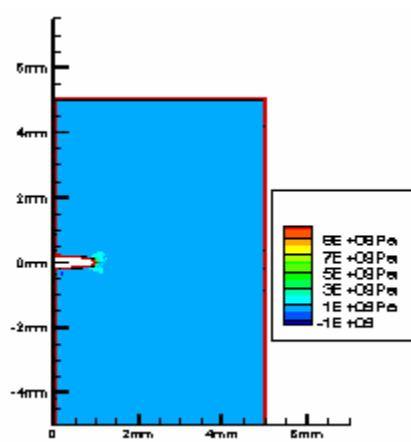(a)   (b)

Fig 36: Contour plots of (a) local σ_{22} stress and (b) effective σ_{22} stress for characteristic length scale=70microns

(a)   (b)

Fig 37: Contour plots of (a) local σ_{22} stress and (b) effective σ_{22} stress for characteristic length scale=100microns

4.3) Crack Normal to Bi-material Interface and 100 microns away:

The problem of a crack normal to the interface of a structurally non-homogeneous ceramic bi-material specimen is solved and results are presented in this section. The materials used are the same as in the case of a bi-material interface crack problem. The geometry and loading of the specimen are shown in the Fig. 38 below.
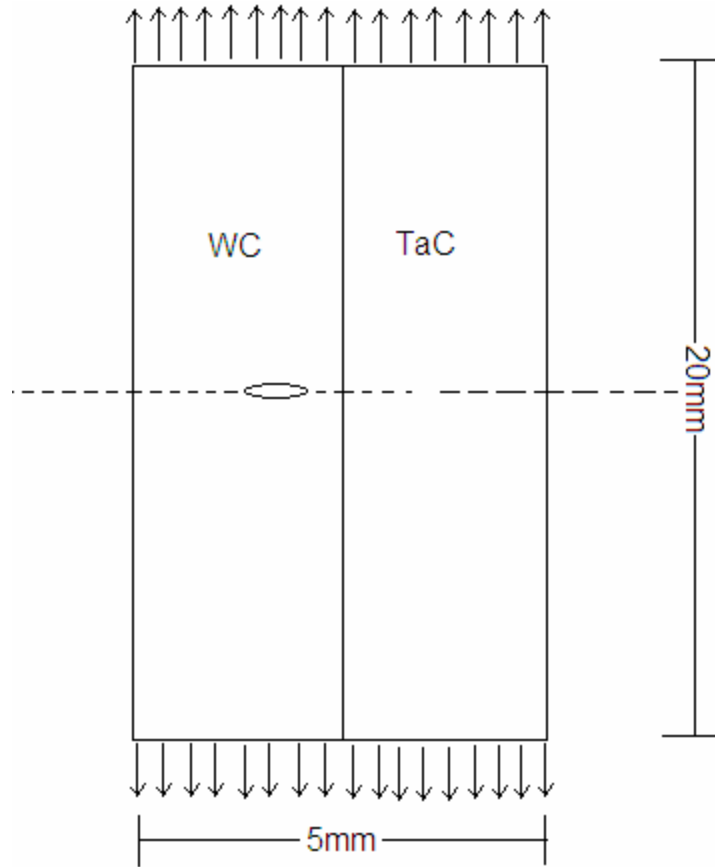

Fig 38: Problem Description

It can be easily observed that the geometry of the specimen and loading are both symmetrical about the dashed line. It is for this reason only half of the above specimen is wisely chosen for simulation. The geometry and boundary conditions of the simulation domain is shown in Fig. 39.
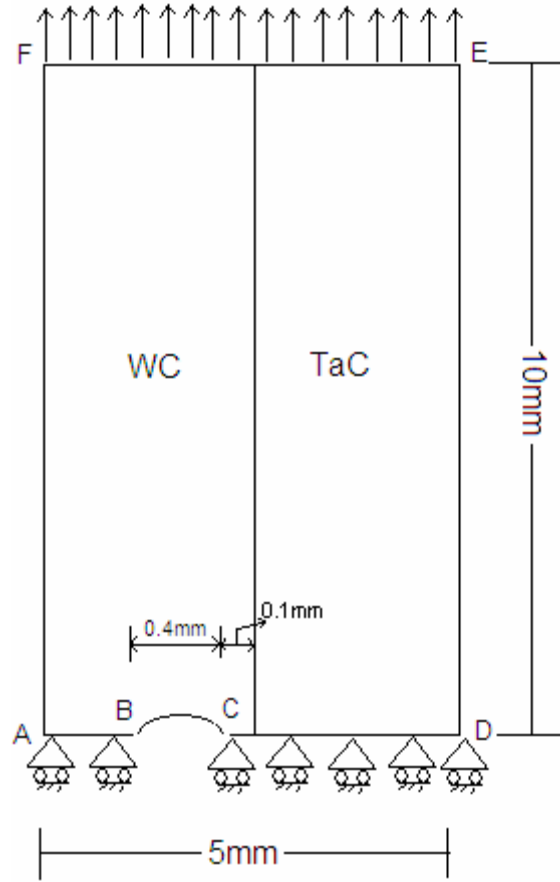
Fig 39: Problem Description: Geometry and boundary conditions

The BC is a crack normal to the bi-material interface and 100 microns away from it under Mode-I loading conditions. The domain is 5mm wide and 10mm in length with a 0.4mm crack normal to the interface. The portions AB & CD are subjected to symmetrical boundary conditions restricting movement in the vertical direction. The specimen is pulled along the boundary FE by displacing the surface uniformly by 0.01mm. Regarding the higher-order boundary conditions, the first gradient of strain normal to the boundary is prescribed to zero. The results of mesh sensitivity analysis and effect of characteristic length scale are presented below

4.3.1) Mesh Sensitivity analysis:

Mesh sensitivity analysis is a process of refining mesh size to achieve a converged solution. The plots of structure of crack tip, local stress and effective stress are presented for four different meshes as shown in the Fig. 40(a)-(d), with mesh1 being coarse and mesh4 being the finest, in the Figs. 40-44.

4.3.1.1) Structure of the crack tip:

The following graph shows the plot of vertical displacement of the crack face along the crack face. The structure of crack tip is plotted for four different meshes as shown in the Fig. 40(a)-(d), and compared with the classical solution. As can be seen from the Fig. 40(e), the response is almost independent of the mesh size.

(a)   (b)   (c)   (d)
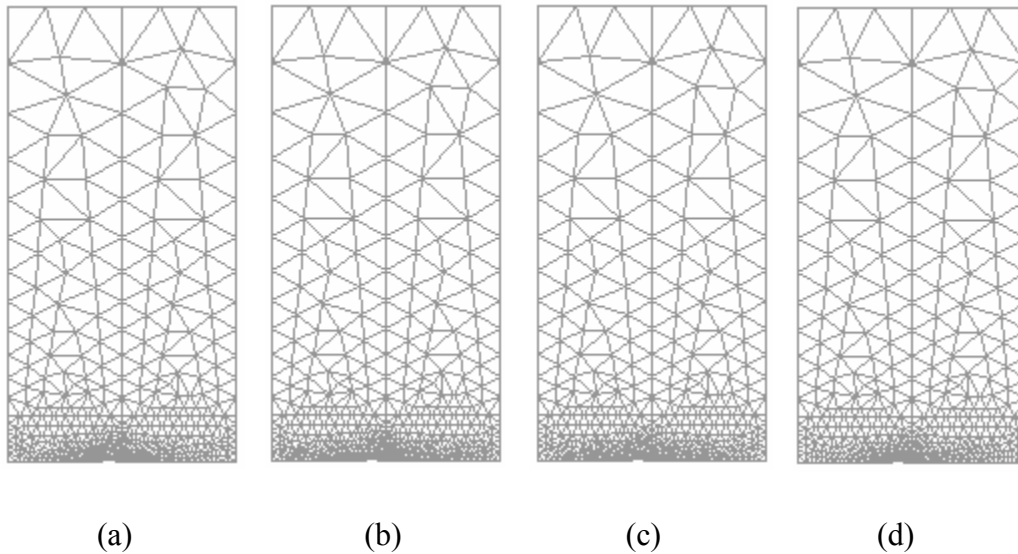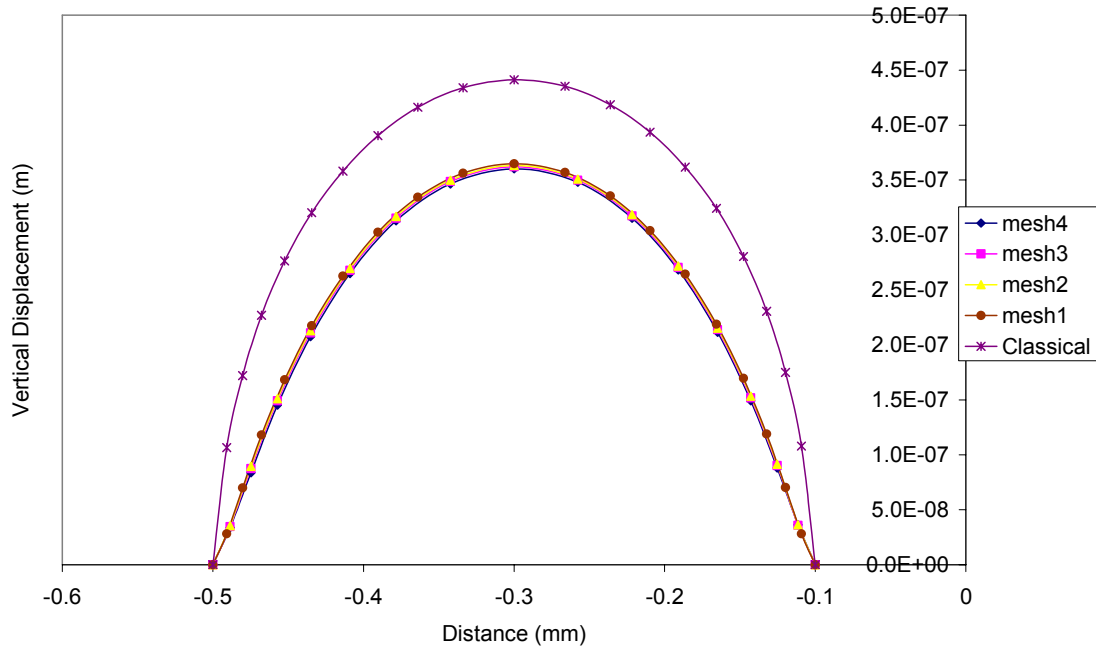
(e)
Fig 40 (a) mesh1 (b) mesh2 (c) mesh3 (d) mesh4
(e) Mesh sensitivity of structure of crack tip

4.3.1.2) Local Stress plots:

The term local stress represents the first term of the constitutive law (see equation (4.1a)) as described in the homogeneous case. The Fig. 41(a) is a plot of local σ_{22} stress component along the boundary line CD of the specimen (see Fig. 39 above) for four different meshes as shown in Fig. 40(a)-(d). It can be observed that the response is independent of mesh size. Fig. 41(b) shows the magnified view of Fig. 41(a) near the crack tip.
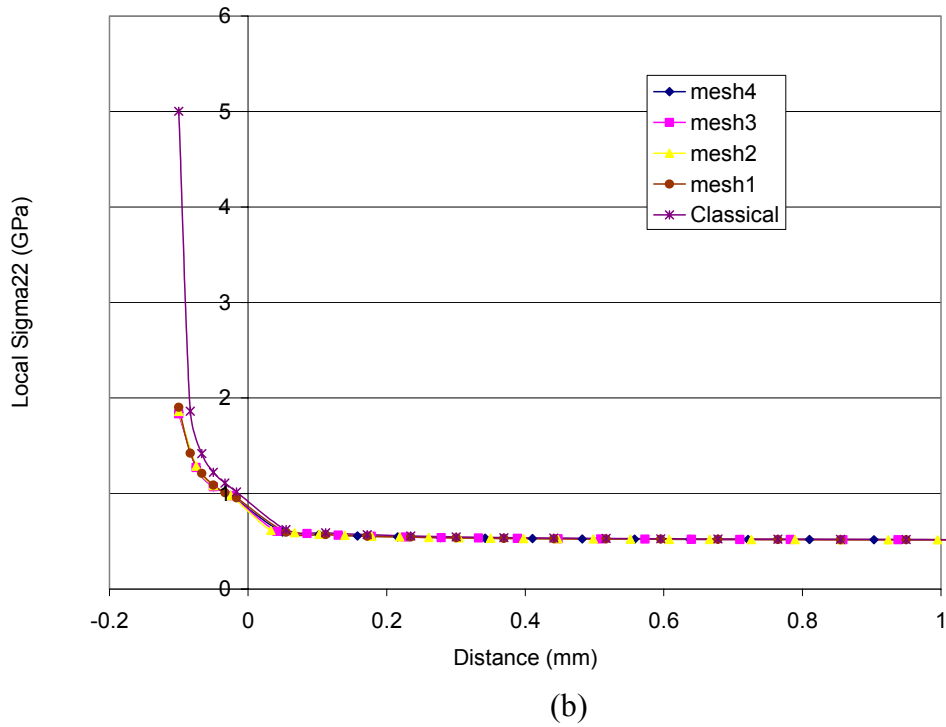
(a)

(b)

Fig 41 (a) Mesh Sensitivity of Local σ_{22} stress component
(b) Magnified image of the plot near the crack tip

The Fig. 42(a) show the plots of local σ_{22} stress component along the boundary line BA of the specimen (see Fig. 39 above) for four different meshes as shown in Fig. 40(a)-(d) . It can be observed that the response is independent of mesh size. Fig. 42(b) shows the magnified view of Fig. 42(a) near the crack tip.
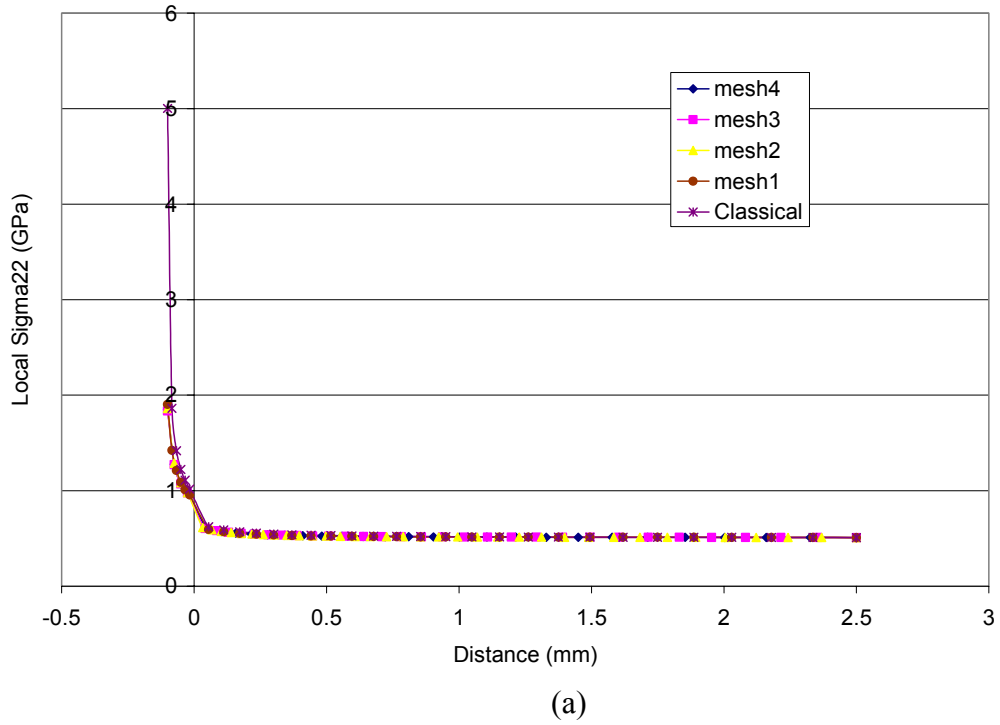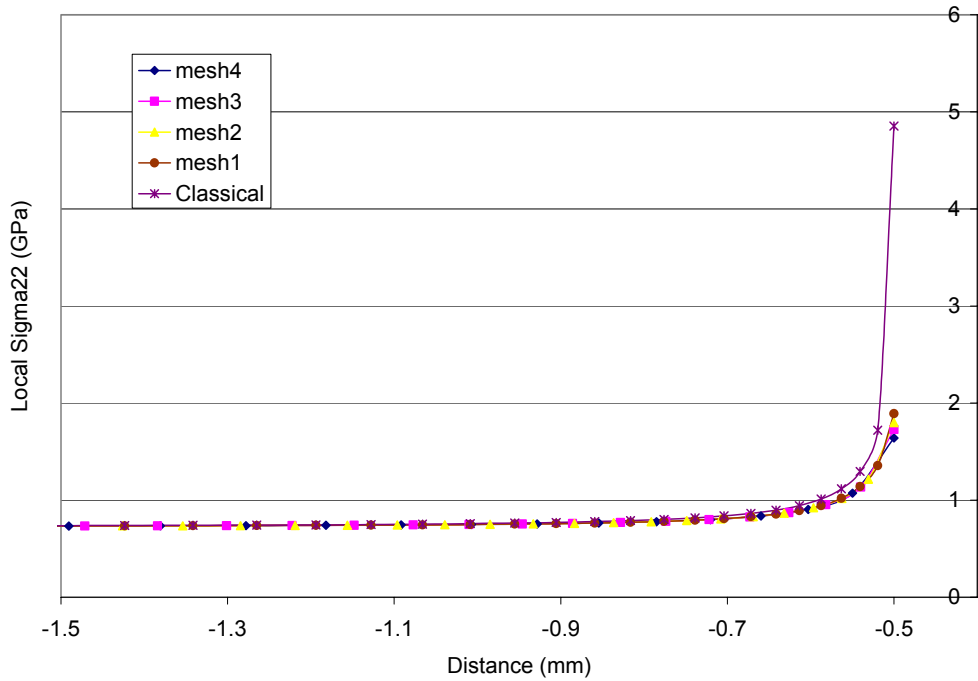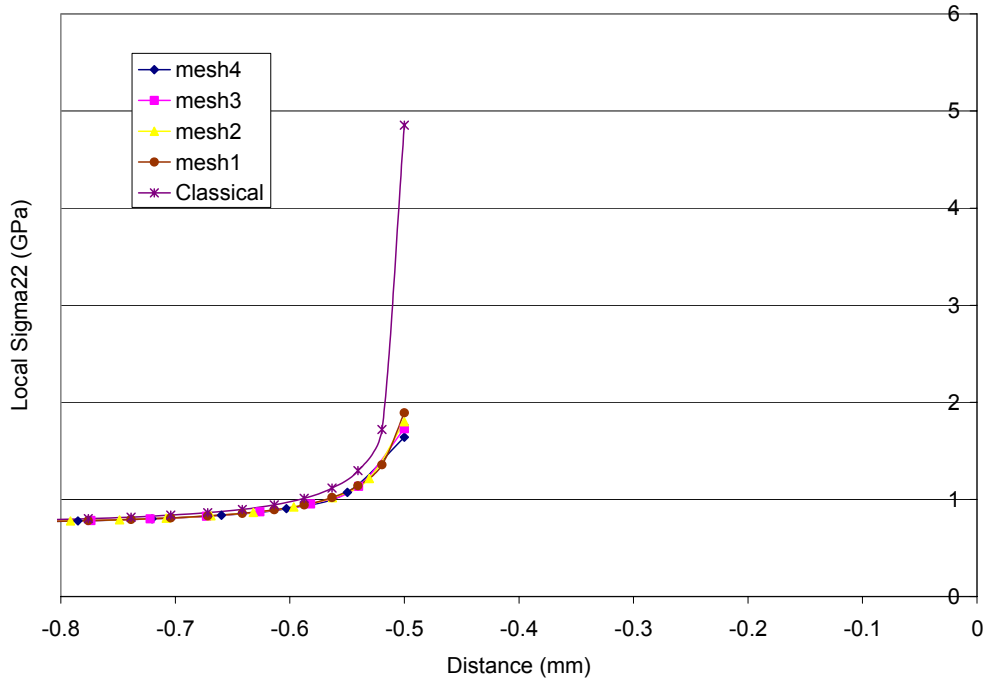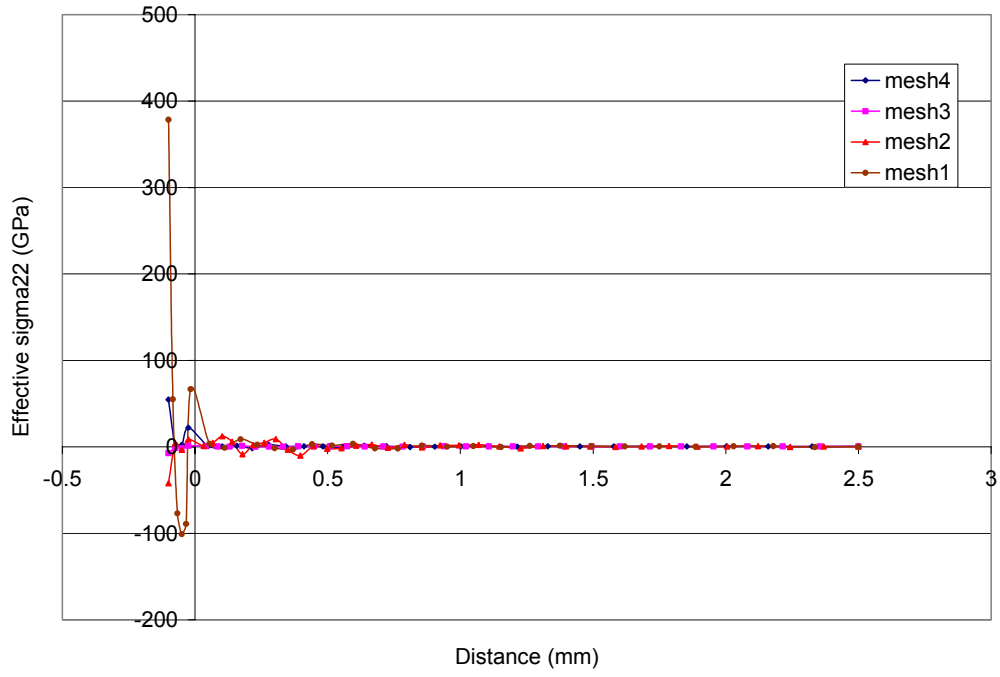

(a)

91

(b)
Fig 42 (a) Mesh Sensitivity of Local σ_{22} stress component
(b) Magnified image of the plot near the crack tip

4.3.1.3) Effective Stress plots:

The term effective stress represents the stress computed from the equation (4.1a) as described in the homogeneous case. The following Fig. 43 show the plots of effective σ_{22} stress component plotted along the boundary line CD (see Fig. 39 above) for four different meshes as shown in the Fig. 40(a)-(d). It can be seen that the response neither converges nor have a particular trend. Fig. 43(b) is a magnified view of the Fig. 43(a) near the crack tip.

(a)
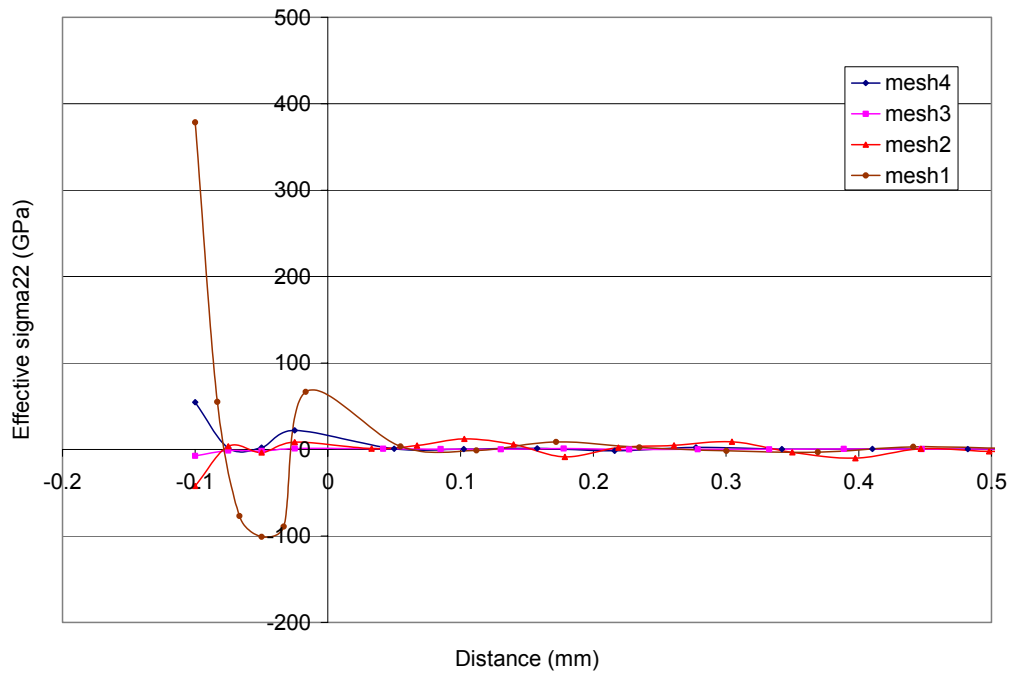
(b)

Fig 43 (a) Mesh Sensitivity of Effective σ_{22} stress component
(b) Magnified image of the plot near the crack tip

The following Fig. 44 show the plots of effective σ_{22} stress along the boundary line BA of the specimen (see Fig. 39 above) for four different meshes as shown in Fig. 40(a)-(d). It can be observed that the effective stress is not a converging.

(a)

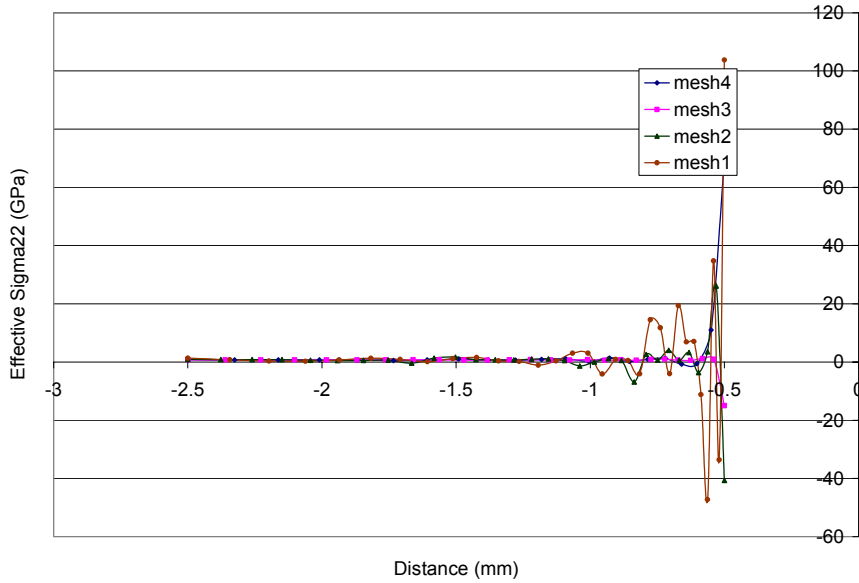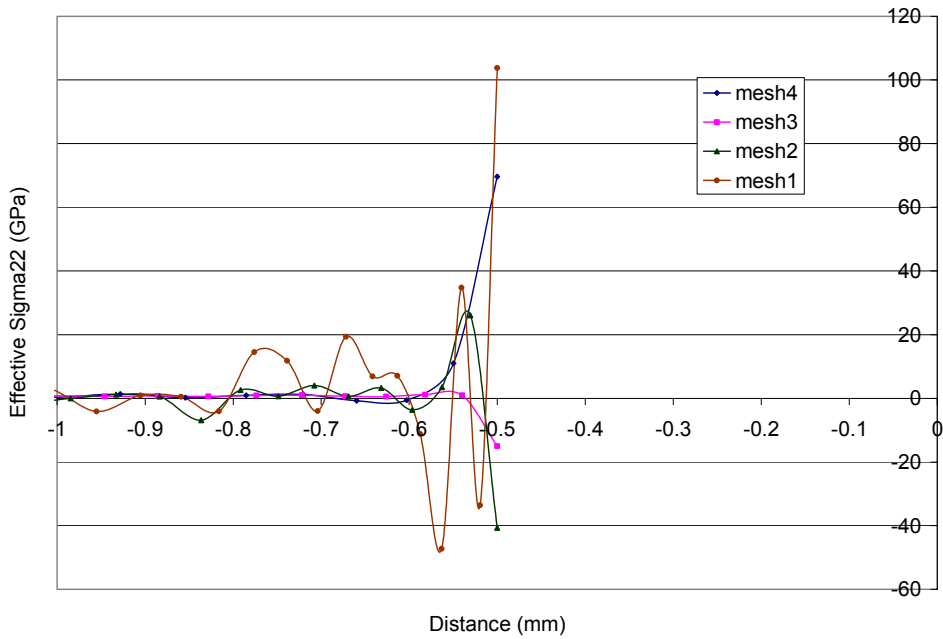(b)

Fig 44 (a) Mesh Sensitivity of Effective σ_{22} stress component
(b) Magnified image of the plot near the crack tip

4.3.2) Effect of Characteristic length scale (l):

The length scale is considered as the spatial span over which non-local interactions are considered. The effect of characteristic length scale on the structure of crack tip, local stress and effective stress are shown in the Figs. 45-51. The unit of the length scale shown in the legend of the following graphs is micrometers.

4.3.2.1) Structure of Crack tip:

The Fig. 45 below shows the effect of length scale on the structure of crack tip. The graph is plotted for four different length scales 20, 30, 50 & 70 micrometers and compared with the classical solution.
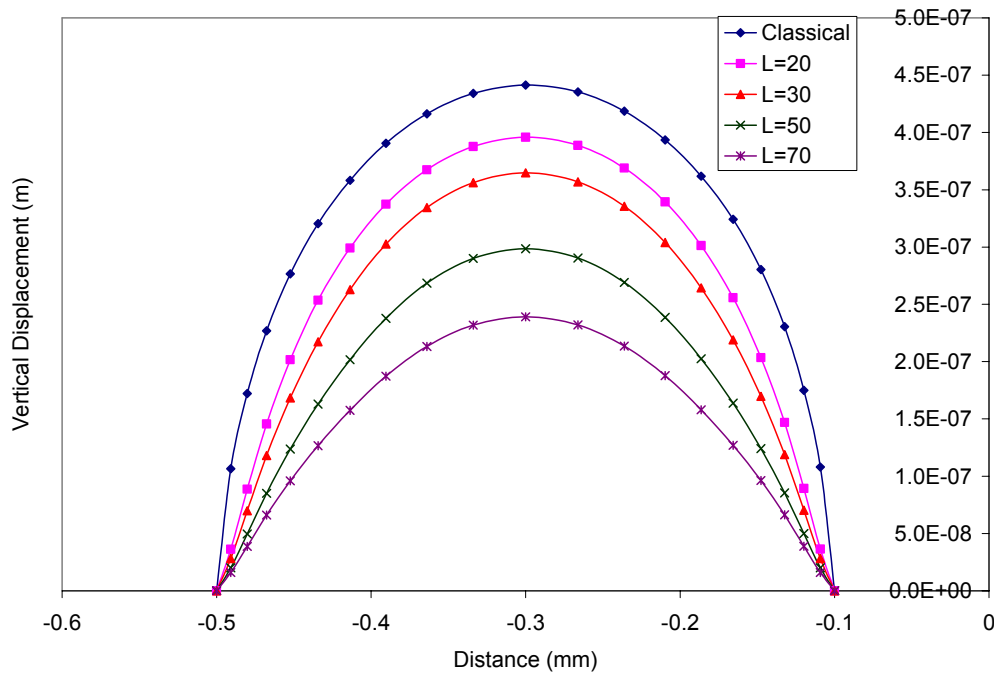

Fig 45: Effect of length scale (l) on Structure of Crack tip

4.3.2.2) Local Stress plots:

The following Fig. 46 shows the plot of local σ_{22} stress along the boundary line BA (see Fig. 39) for four different length scales 20, 30, 50 & 70 micrometers and compared with the classical solution. Fig. 46(b) shows the magnified image of the Fig. 46(a) near the crack tip.

(a)

(b)
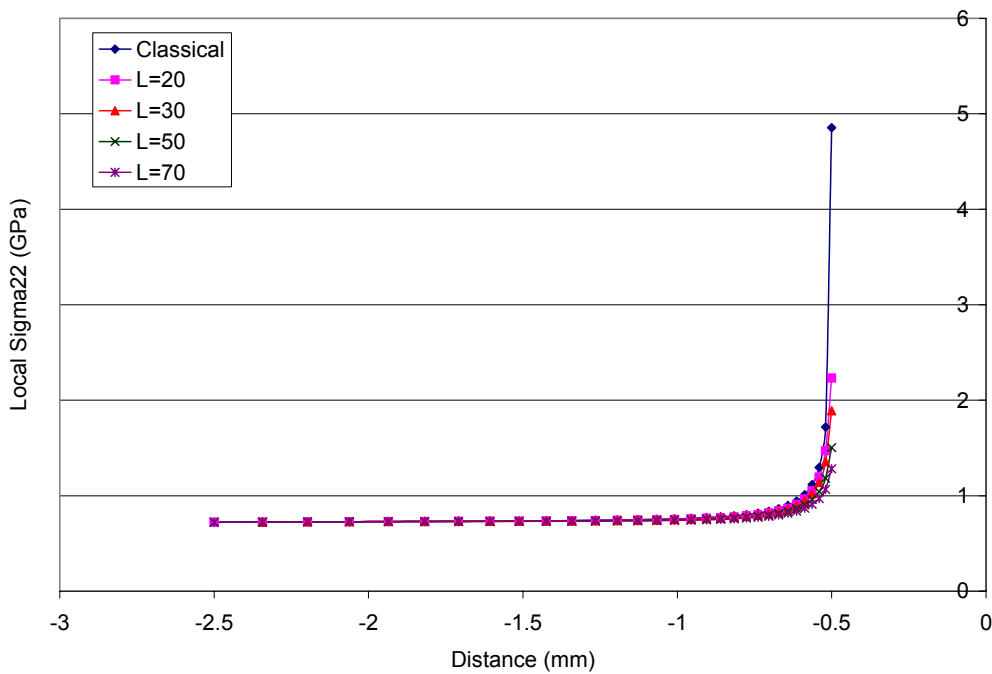
Fig 46 (a) Effect of length scale (l) on Local σ_{22} stress component
(b) Magnified image of the plot near the crack tip

The following Fig. 47 shows the plot of local σ_{22} stress along the boundary line CD (see Fig. 39) for four different length scales 20, 30, 50 & 70 micrometers and compared with the classical solution. Fig. 47(b) shows the magnified image of the Fig. 47(a) near the crack tip.

(a)

(b)

Fig 47 (a) Effect of length scale (*l*) on Local σ_{22} stress component
(b) Magnified image of the plot near the crack tip

4.3.2.3) Effective Stress plots:

The following Fig. 48 shows the plots of effective σ_{22} stress along the boundary line BA (see Fig. 39) for 20, 30, 50&70 micrometers. It can be observed that the effective stress has many fluctuations without any particular trend. Fig. 48(b) shows the magnified image of the Fig. 48(a) near the crack tip.
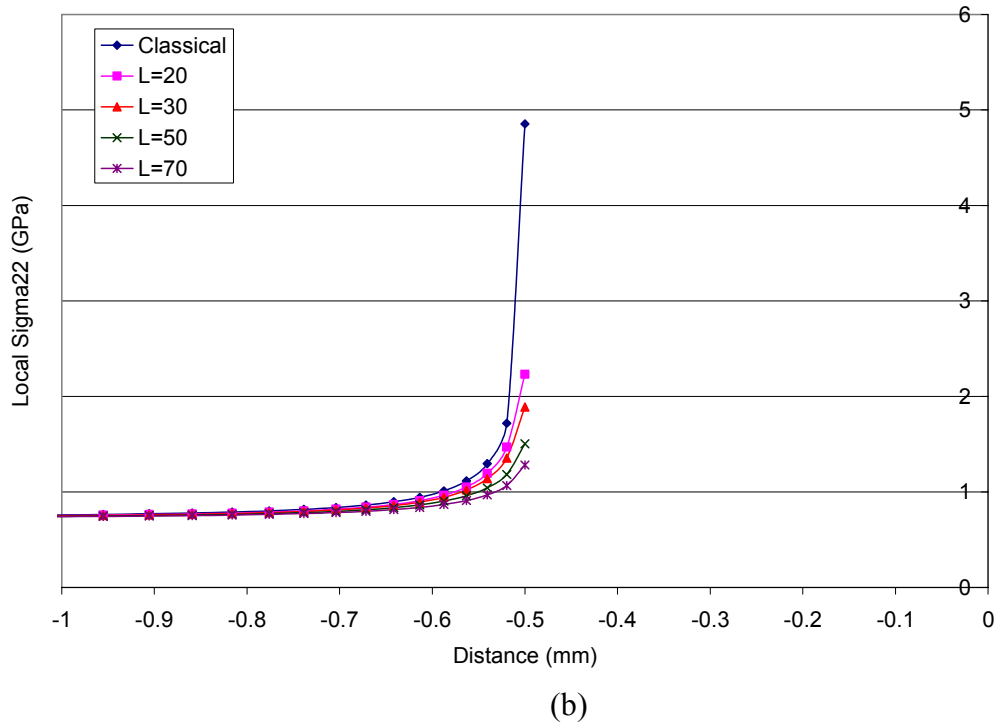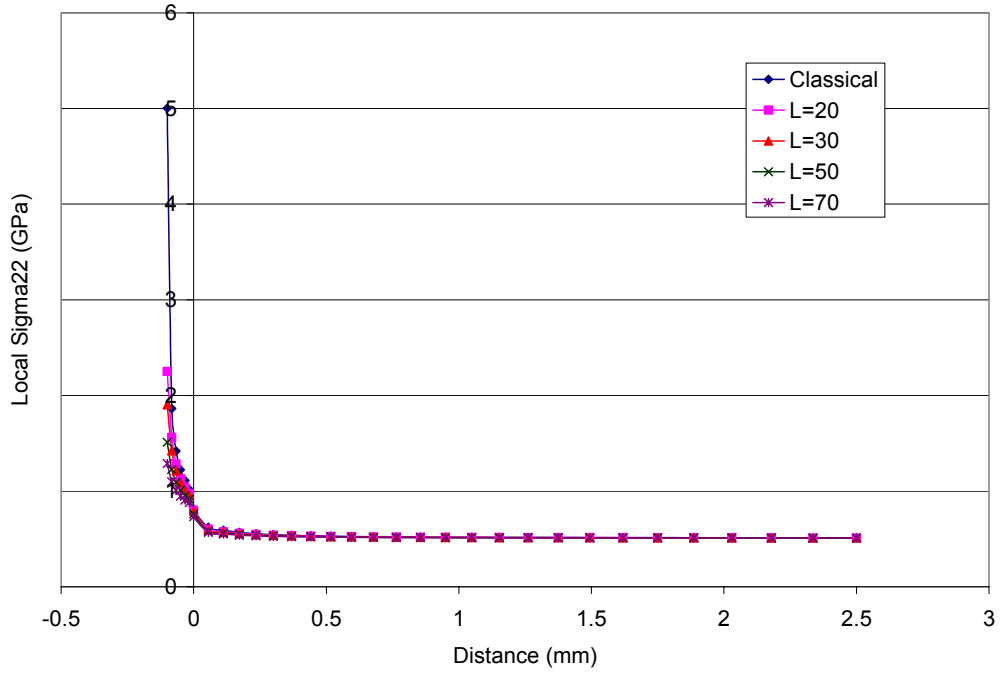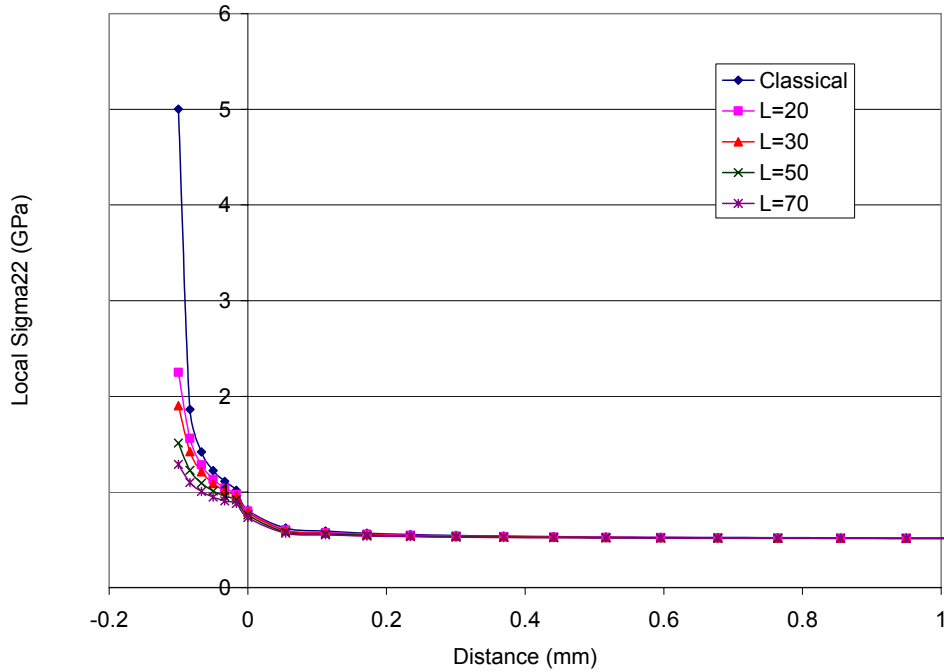

(a)

(b)
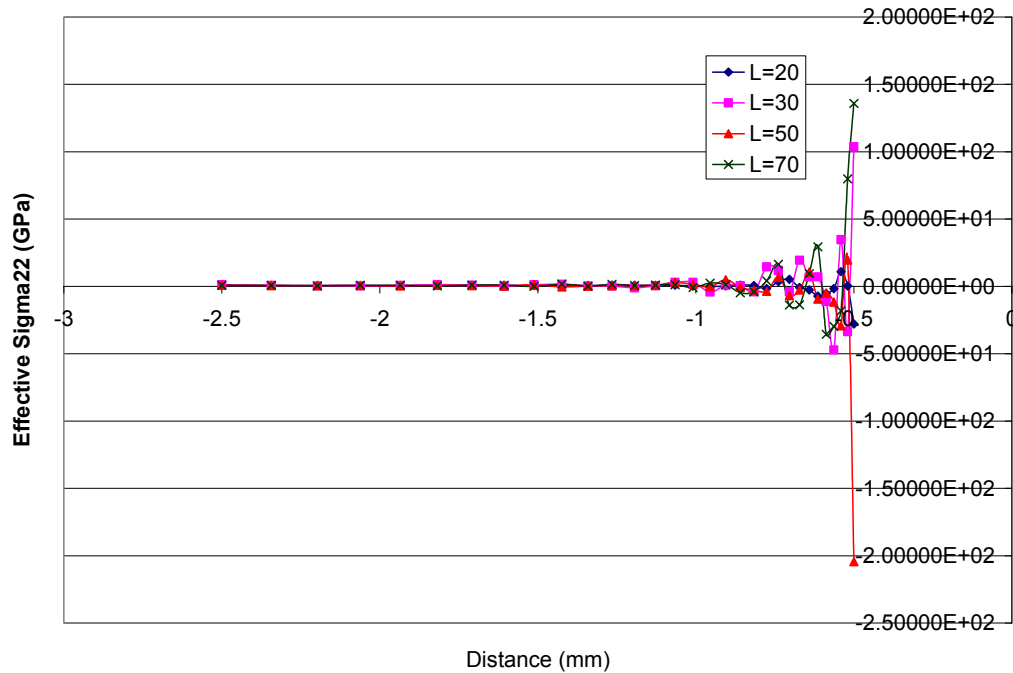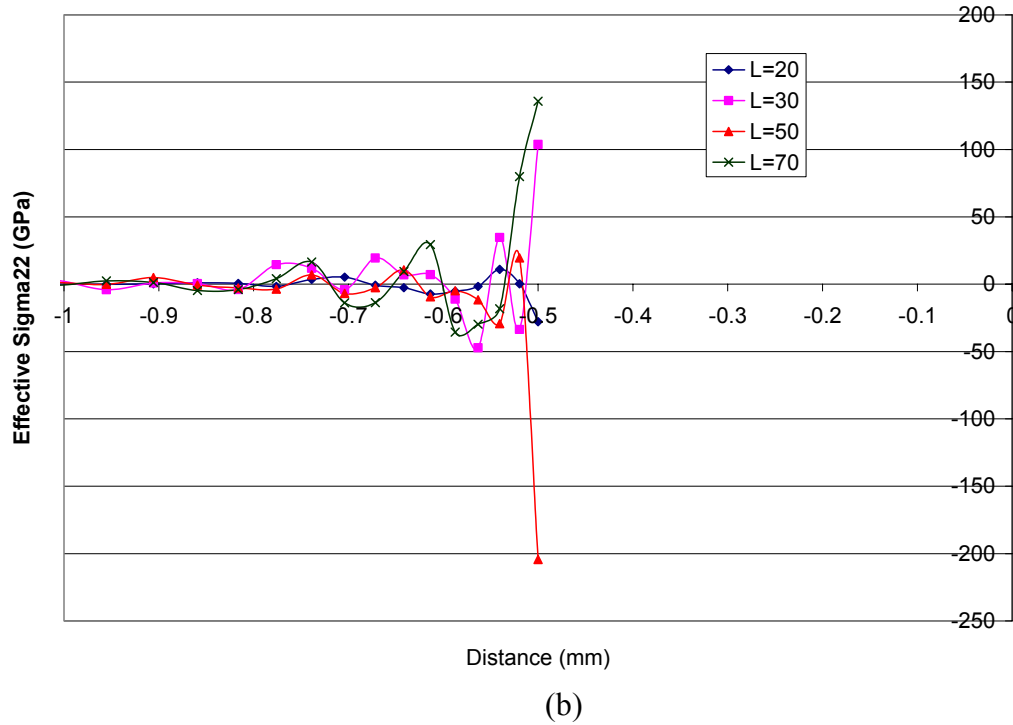
Fig 48 (a) Effect of length scale (l) on Effective σ_{22} stress component
(b) Magnified image of the plot near the crack tip

The following Fig. 49 shows the plots of effective σ_{22} stress along the boundary line BA (see Fig. 39) for 20, 30, 50&70 micrometers. It can be observed that the effective stress has many fluctuations without any particular trend. Fig. 49(b) shows the magnified image of the Fig. 49(a) near the crack tip.

100
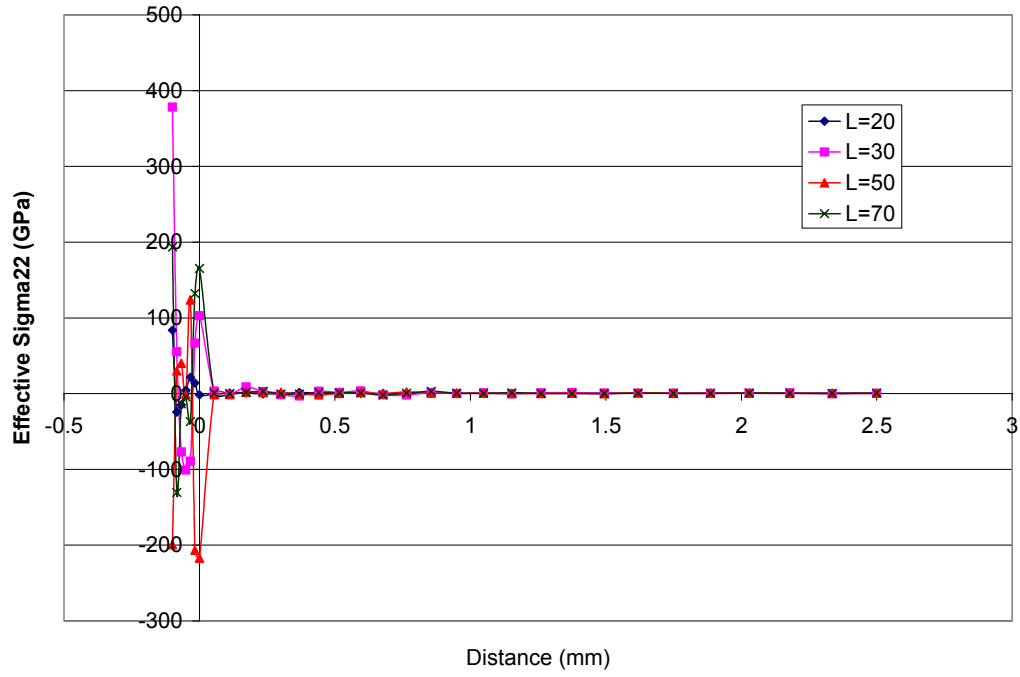
(a)
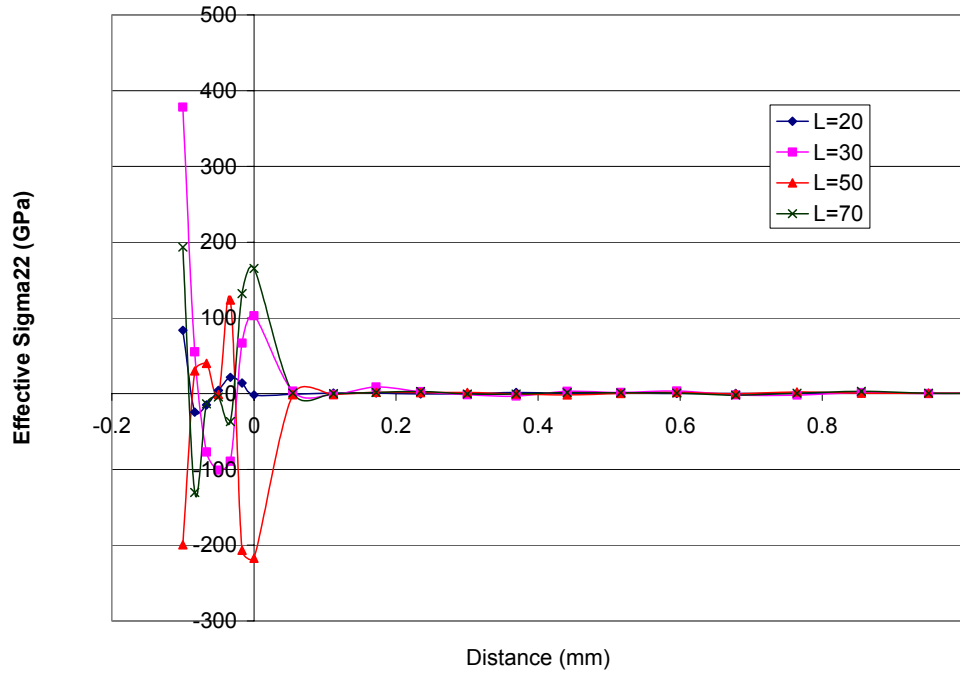
(b)

Fig 49 (a) Effect of length scale (*l*) on Effective σ_{22} stress component
(b) Magnified image of the plot near the crack tip

Local Shear stress plots:

As the specimen is made up of two different materials, there exists a conflict in deformation in the transverse direction which results in shear stress and Mode-II type deformation. The local shear stress plots for four different length scales 20, 30, 50&70 micrometers are shown in Figs. 50(a)-(b) and 51(a)-(b). The Fig. 50 shows the plot of local shear stress along the boundary line BA of the specimen (see Fig. 39 above).

(a)

102
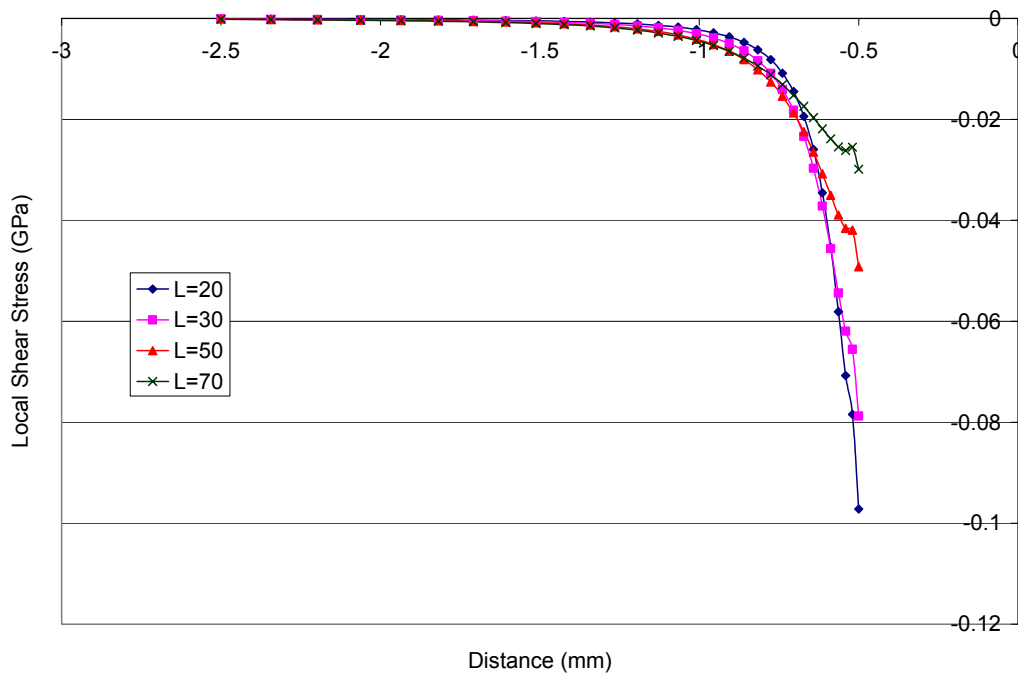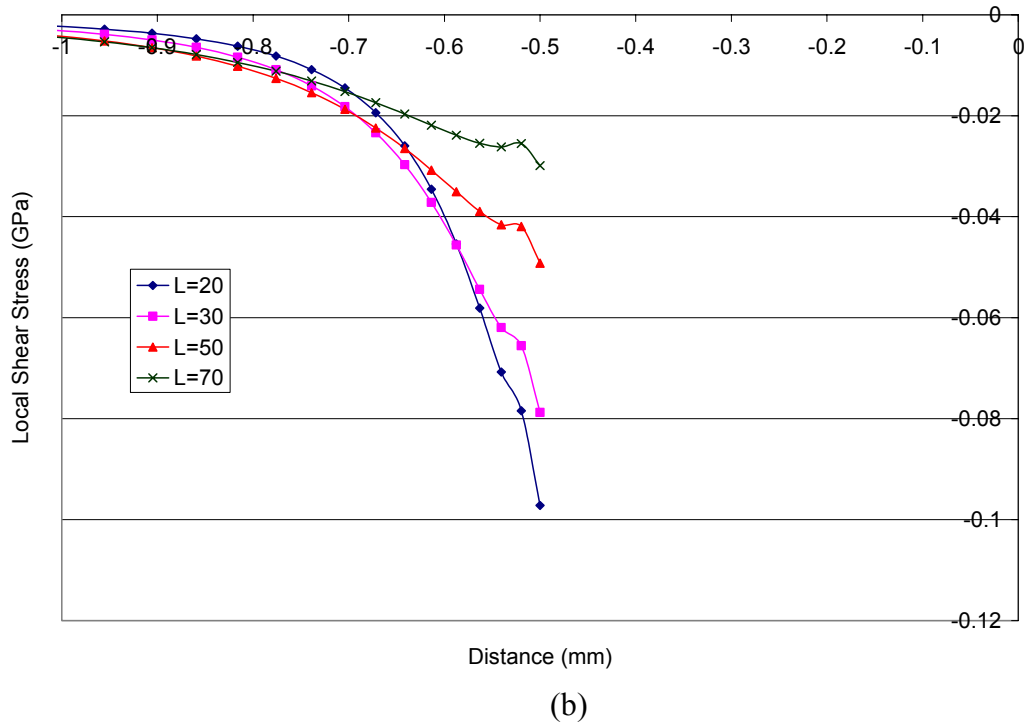
Fig 50 (a) Effect of length scale (*l*) on Local shear stress component
(b) Magnified image of the plot near the crack tip

The Fig. 51 shows the local shear stress plots along the boundary line CD of the specimen (see Fig. 39 above) for 20, 30, 50&70 micrometers. Fig. 51(b) shows the magnified image of Fig. 51(a) near the crack tip.
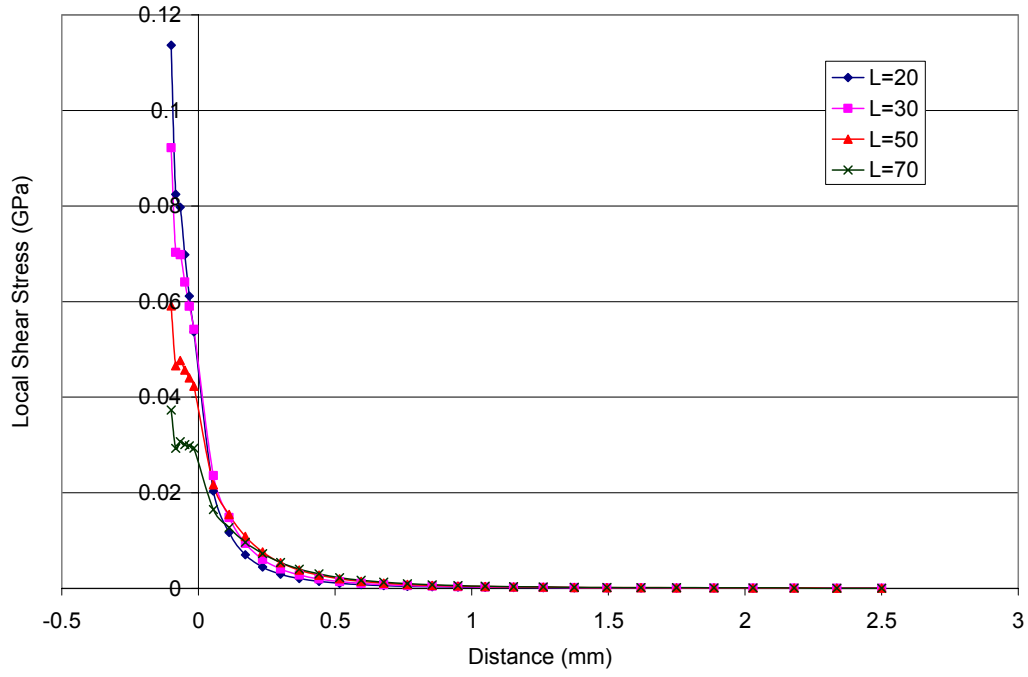
(a)
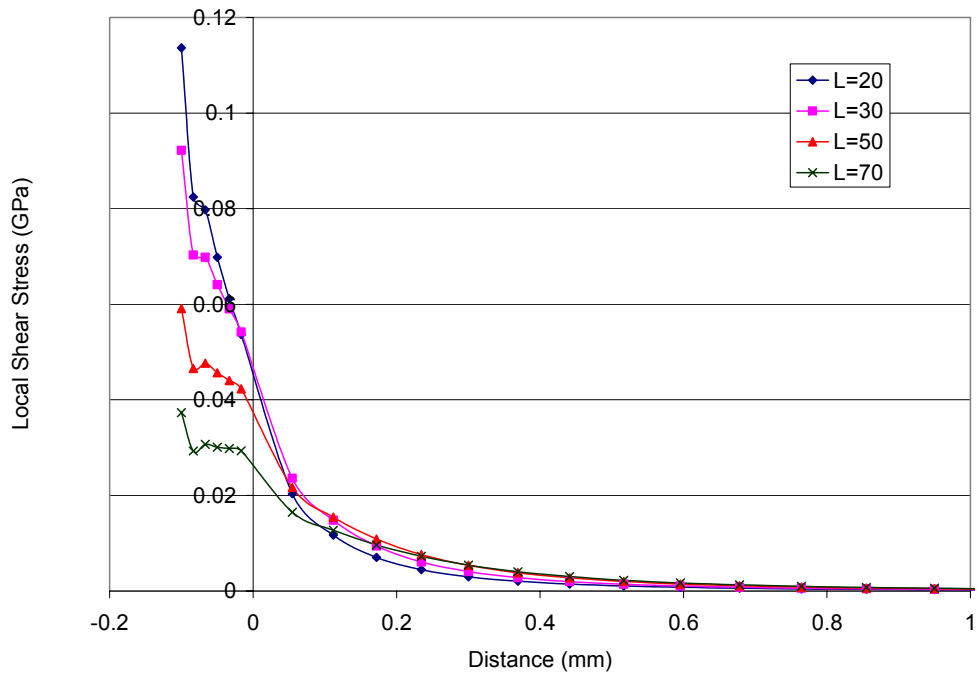
(b)

Fig 51 (a) Effect of length scale (*l*) on Local shear stress component
(b) Magnified image of the plot near the crack tip

Contour plots:

In this sub-section, the contour plots of local σ_{22} stress for various length scales. The Fig. 52 shows the contour plots for characteristic length scale 20, 30, 50&70 micrometers.

(a)

(b)

(c)

(d)
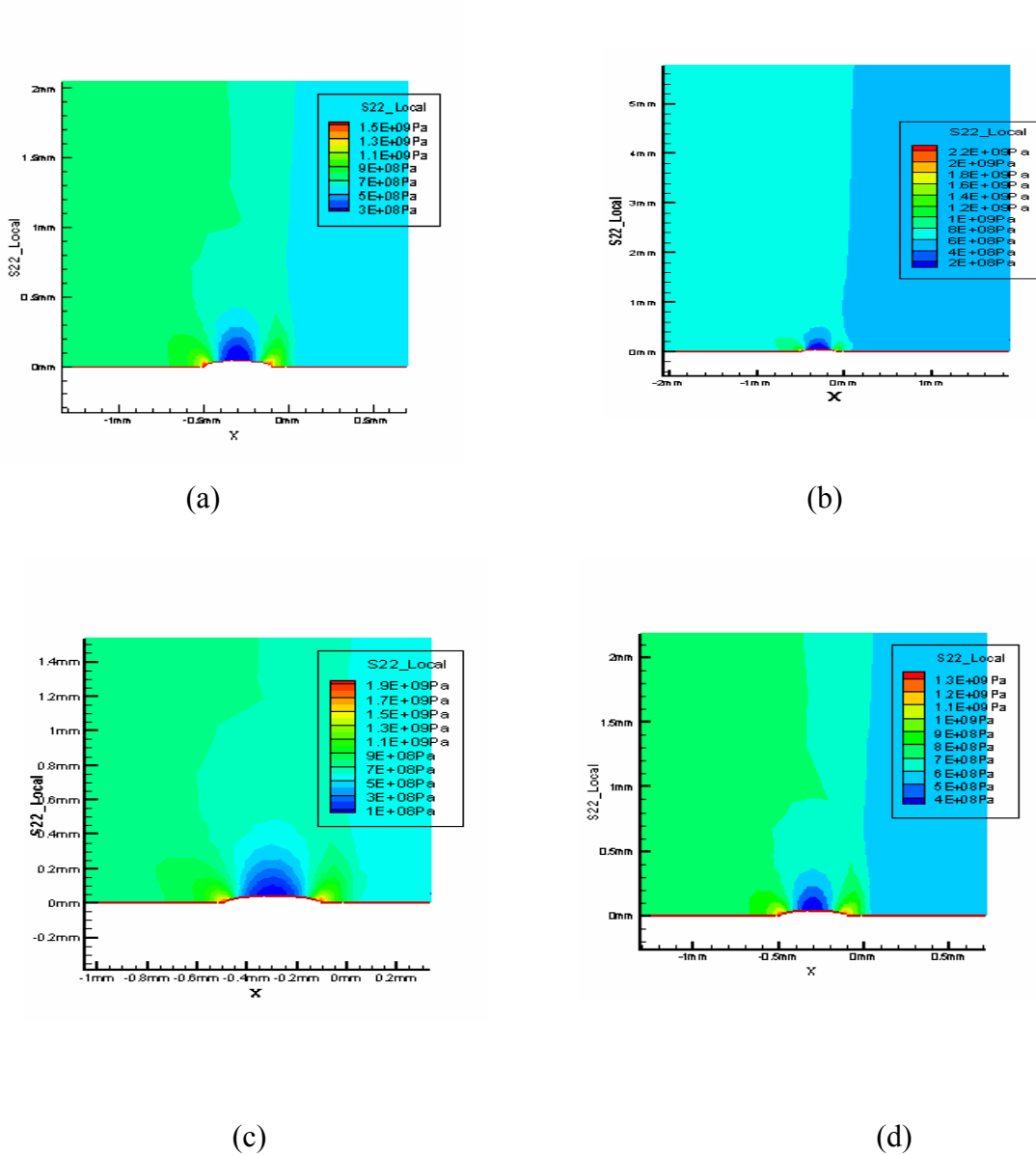
Fig 52: Contour plots of local σ_{22} stress for characteristic length scale (a) 20 microns (b) 30 microns (c) 50 microns (d) 70 microns

CHAPTER 5

DISCUSSION OF RESULTS

5.1) Crack in a homogeneous material:

The results obtained from the simulation of a crack in a homogeneous elastic brittle material are presented for six meshes (mesh1 to mesh6) with mesh1 being the coarse and mesh6 the finest as shown in the Fig. 4(a)-(f). Fig. 4(g) shows the mesh sensitivity analysis of the structure of the crack tip. It can be easily seen from the graph that the response is independent of mesh size. Fig. 5 shows the mesh sensitivity analyses of the local σ_{22} stress component plotted along the boundary line BC (see Fig. 3) which also elucidates the mesh insensitivity of the local stress solution. The curves of the Effective σ_{22} stress component vs. distance along the boundary line BC (see Fig. 3) for different meshes are shown in Fig. 6. Upon mesh refinement from mesh 1 to mesh6, the nature of the solution converges to the one shown by mesh5 & mesh6 at the crack tip.

The effect of characteristic length scale on the structure of crack tip and stress field are shown in the Figs. 7-9. The length scale embedded in the theory is considered as the spatial span over which non-local interactions are taken in account. The length scale choice has been made such that at least more than one element is covered. Fig. 7 shows the effect of characteristic length scale on the structure of crack tip. It can be noticed from the graph that the closure of the crack tip is smoothened with the increase in length scale. This can be appreciated more clearly from the graph plotting the slope change of Fig. 6 shown below.

106
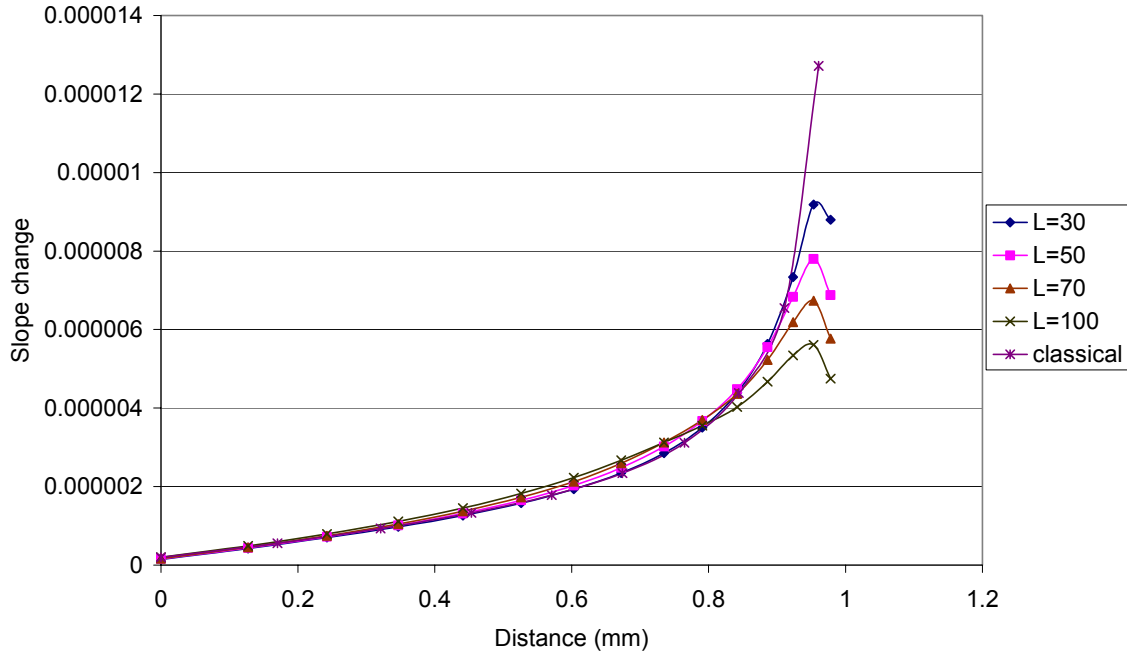
Fig 53: Slope change of the structure of crack tip

The curves of the Local σ_{22} stress component vs. distance along the boundary line BC (see Fig. 3) for different length scales are shown in the Fig. 8. It can be observed from the graph that the crack tip stress and the rate at which it dies out as moved away from the tip is decreased. Recalling that the classical stress solution varies as $\frac{1}{\sqrt{r}}$ with r being the distance from the crack tip, we propose the variation of local stress field as

$$\sigma \propto \frac{1}{r^n} \qquad\qquad \text{----------- (5.1)}$$

The order of singularity (n) of the local stress decreases as the length scale is increased as shown in Fig. 54. Fig. 9 shows the effect of length scale on the Effective σ_{22} stress component plotted along the boundary line BC (see Fig. 3). As it can be seen from the graph, the crack tip stress still persists but the nature of the solution is different from that of classical in the neighborhood of the crack tip. Although the crack tip stress is singular,

the stress approaches a finite value near the crack tip. There is a hump in the stress very near the tip and the height of the hump decreases as the length scale is increased. It can be observed more clearly in the Fig. 55. The hump in the effective stress is occurred at about 72.5 microns from the crack tip.
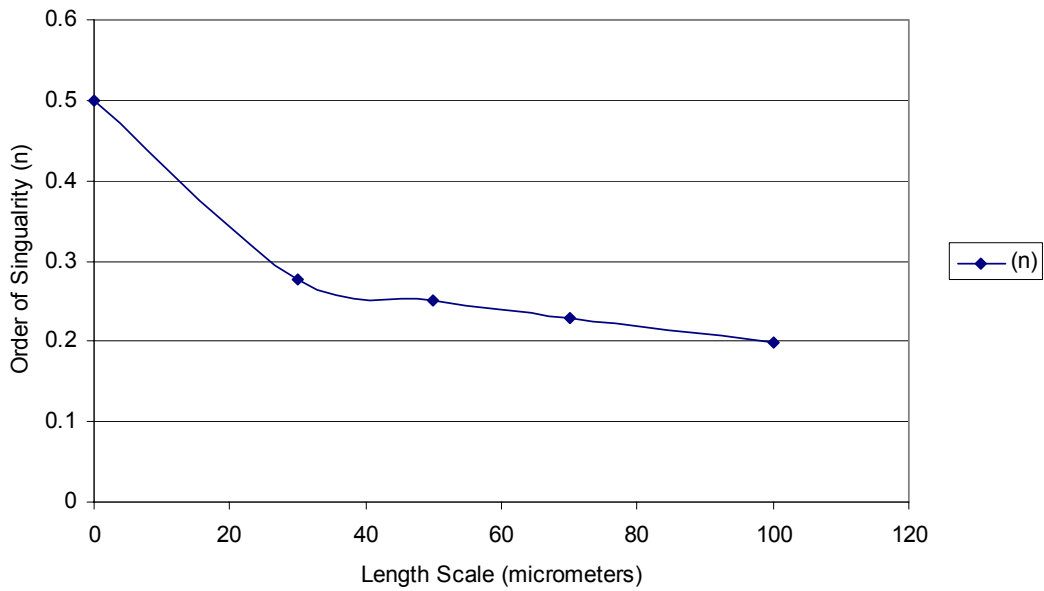
Fig 54: Change in the order of singularity with length scale
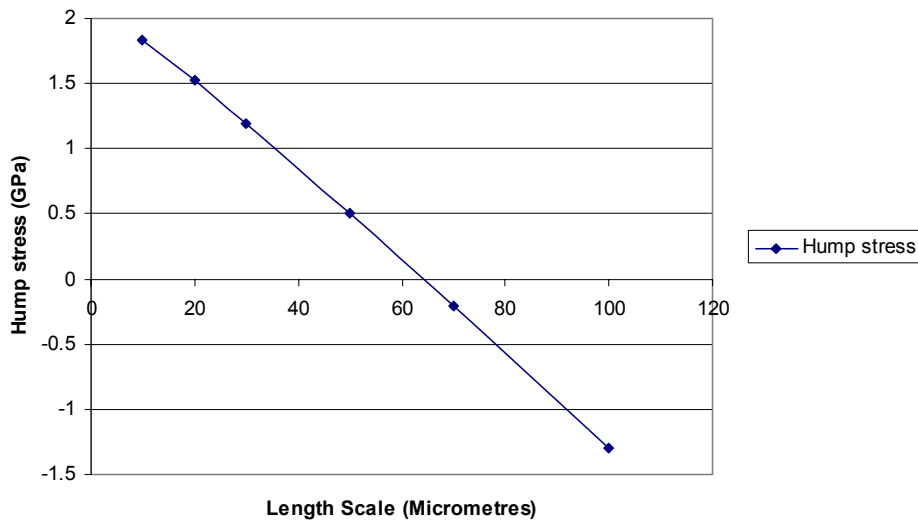
Fig 55: Change in the Hump stress with characteristic length scale

Mode-I Stress intensity factor:

The stress intensity factor is a parameter which is used to quantify the state of stress at the crack tip. The Mode-I stress intensity factor is calculated using the formula

$$K_I = \lim_{r \to 0} \left\{ \sqrt{2\pi r} \, \sigma_{22}(r,0) \right\} \qquad \text{---------- (5.2)}$$

The effect of crack length on the Mode-I stress intensity factor using both classical and gradient elasticity is shown in the graph below.
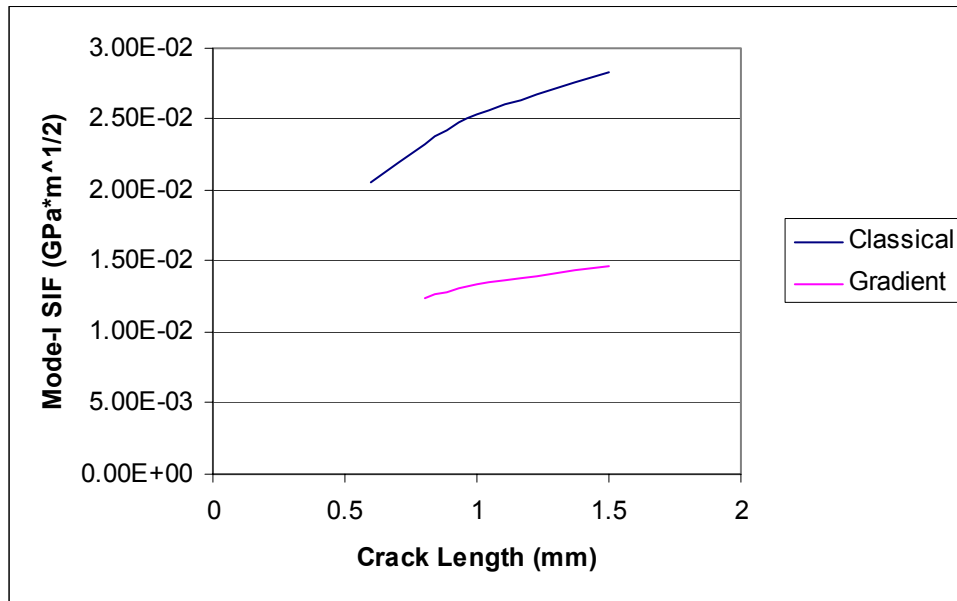
Fig 56: Effect of crack length on the stress intensity factor

5.2) Bi-material interface crack:

Theoretical investigations of bi-material interface crack are dated back to late fifties. Williams [17] was the first to solve the problem of bi-material interface crack from a LEFM perspective. He found that the stress and displacement fields at the crack tip are

highly oscillatory. From the Williams asymptotic analysis, stresses and displacements behave as

$$\sigma \approx r^{-\frac{1}{2}}(\sin, \cos)(\varepsilon \log r) \qquad\qquad \text{--------------- (5.3)}$$

$$u \approx r^{-\frac{1}{2}}(\sin, \cos)(\varepsilon \log r) \qquad\qquad \text{--------------- (5.4)}$$

$$\varepsilon = \frac{1}{2\pi} \log\left(\frac{1-\beta}{1+\beta}\right) \qquad\qquad \text{-------------- (5.5)}$$

where β is a dimensionless composite parameter dependent on material properties introduced by Dundurs given by equation (4.2). Erdogan [18] considered non-homogeneous plane with cracks and found that the extent of oscillatory behavior is of the order of 10^{-6} of the crack length. The oscillatory solution implies that the upper and lower faces of the crack wrinkle and overlap at the tips, which is physically inadmissible. The classical solution found from the finite element analysis is given in Fig. 57.
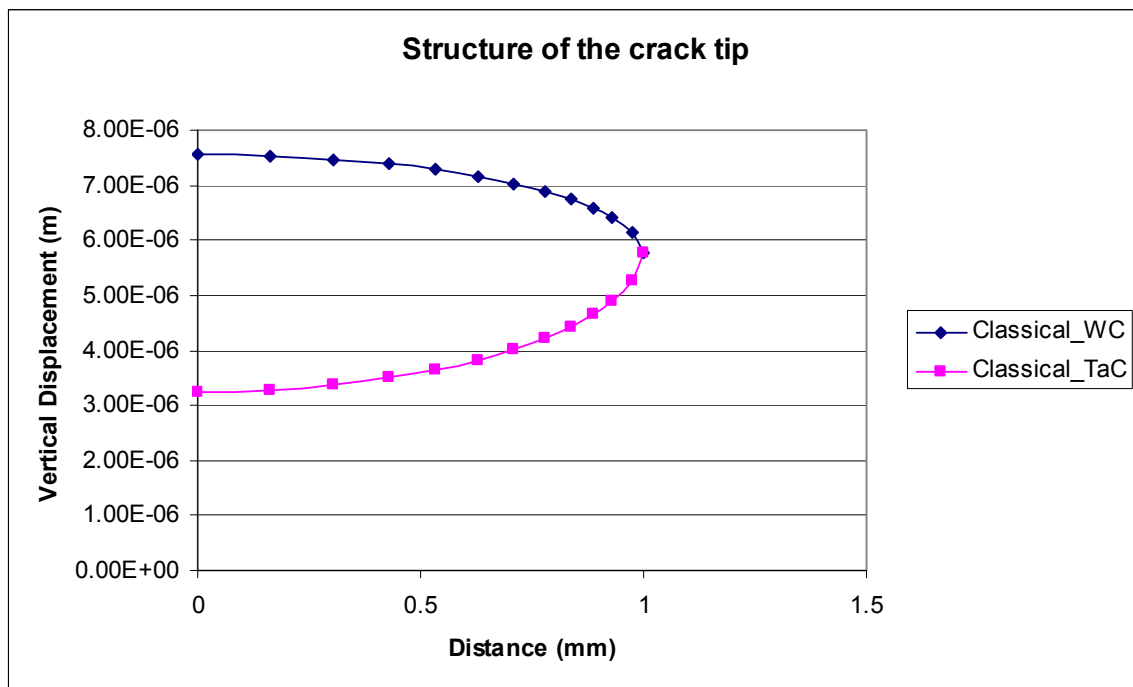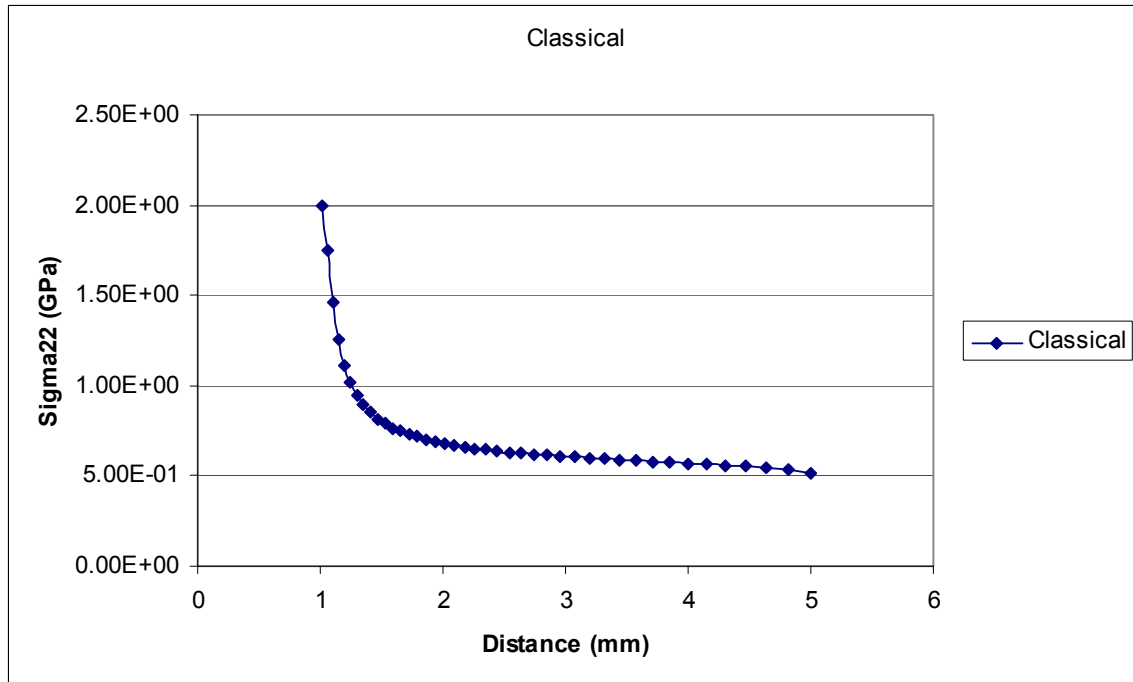
Fig 57: Classical solution of bi-material interface crack problem

The length of the bi-material interface crack in the present work is 1mm. Therefore, the span of oscillation in the solution is around 0.1 Angstroms. To capture the oscillatory

behavior which is over a spatial span of the order of 10^{-8}, the finite element size around the crack tip must be in this order.

The mesh sensitivity analysis results of the bi-material interface crack problem are presented from Figs.17–22. The results for the mesh sensitivity analysis are presented for four meshes (mesh1 to mesh4) as shown in Fig. 17(a)-(d), with mesh1 being the coarse and mesh4 is being the finest. Fig. 17(e) shows the structure of the crack tip for four different meshes. It is apparent from the graph that the response is independent of the mesh size. As the bi-material interface FH belongs to different materials, local and effective stresses are plotted on the lines F'H' and F''H'' as shown in the Fig. 58 below. These two plot lines are very close to the bi-material interface.

Fig 58: Problem Description

Figs. 19 and 20 show the local stress plotted on F'H' and F''H'' respectively. It can be clearly seen from the graph that the response is independent of mesh size. Figs. 21and 22 show the effective stress plotted on F'H' and F''H'' respectively. As can be observed from the graph, the nature of the solution converges for mesh3 and mesh4.

Fig. 23 depicts the effect of characteristic length scale on the structure of the bi-material interface crack. The closure of structure of the crack tip is smoothened as the length scale is increased. This can be elucidated pictorially from the slope change graph shown in Fig. 59.

Fig 59: Slope change of the structure of bi-material interface crack tip with characteristic length scale.

Figs. 24 and 25 show the change in the local stress field with a change in the characteristic length scale. As it can be observed from the graphs, the crack tip stress is

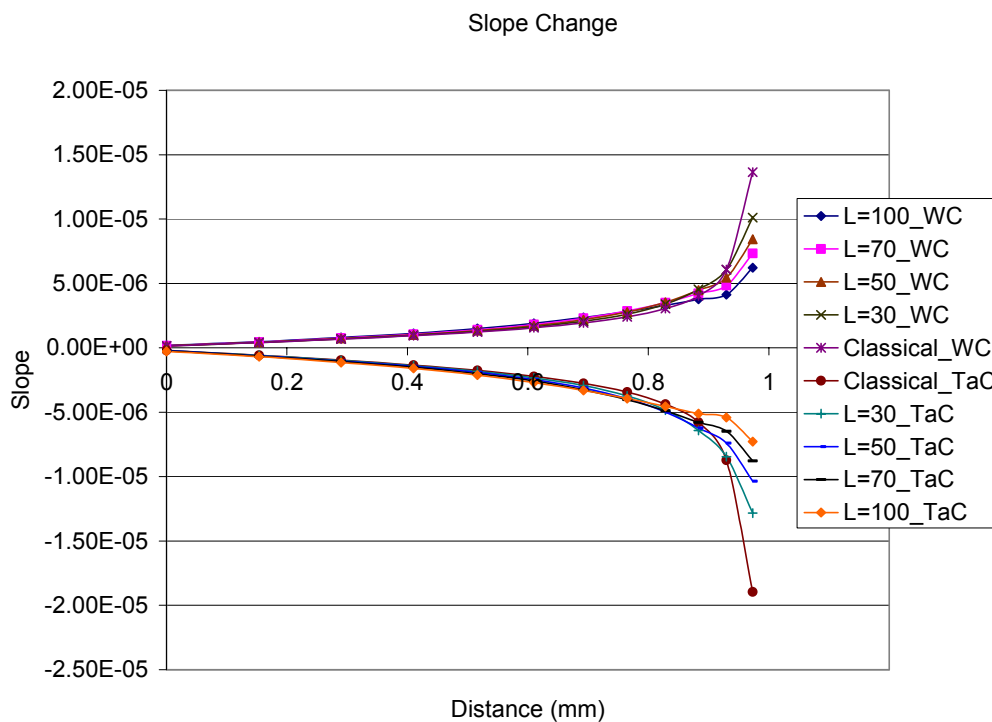decreased and the rate at which it decays as moved away from the tip also decreases, with increase in the characteristic length scale. Figs. 26 and 27 show the effect of length scale on the effective stress field. The crack tip singularity still persists but the nature of the solution is different from the classical one. Although the crack tip stress is singular, a finite stress is approached very close to the crack tip. Such a physically meaningful solution at least in the neighborhood of crack tip is a consequence of incorporation of non-local interactions by length scale. The effective stress has a hump in the curve very near the crack tip and the peak stress of the hump decreases as the length scale is increased.
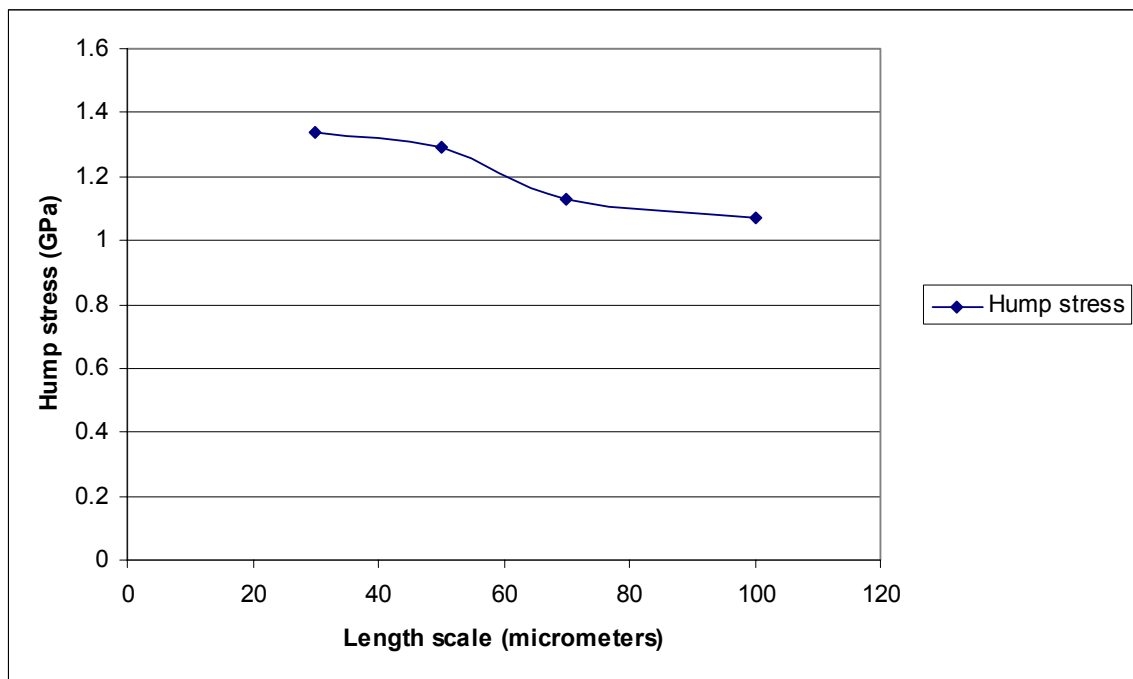

Fig. 60: change in hump stress with length scale

Effect of characteristic length scale on the stress intensity factor:

The stress intensity factor in classical linear theory (which is local) is parameter which quantifies the state of stress at the crack tip. However, in the current non-local theory, the

effective stress field is oscillatory near the crack tip. Nonetheless in order to compare the two theories, we adopt similar definitions as in classical theory for the stress intensity factors K-I and K-II as

$$K_I = \lim_{r \to 0}\left\{\sqrt{2\pi r}\,\sigma_{22}(r,0)\right\} \ \& \ K_{II} = \lim_{r \to 0}\left\{\sqrt{2\pi r}\,\sigma_{12}(r,0)\right\} \qquad \text{------------ (5.6)}$$

with σ_{22} and σ_{12} being the local stresses evaluated from equation 4.1b.

As the specimen is made up of two different materials, Mode-I and Mode-II stress intensity factors are calculated separately approaching the crack tip along lines F'H' and F''H'' in WC and TaC respectively. Figs. 61 and 62 show the effect of length scale on K-I and K-II calculated separately for two different materials.
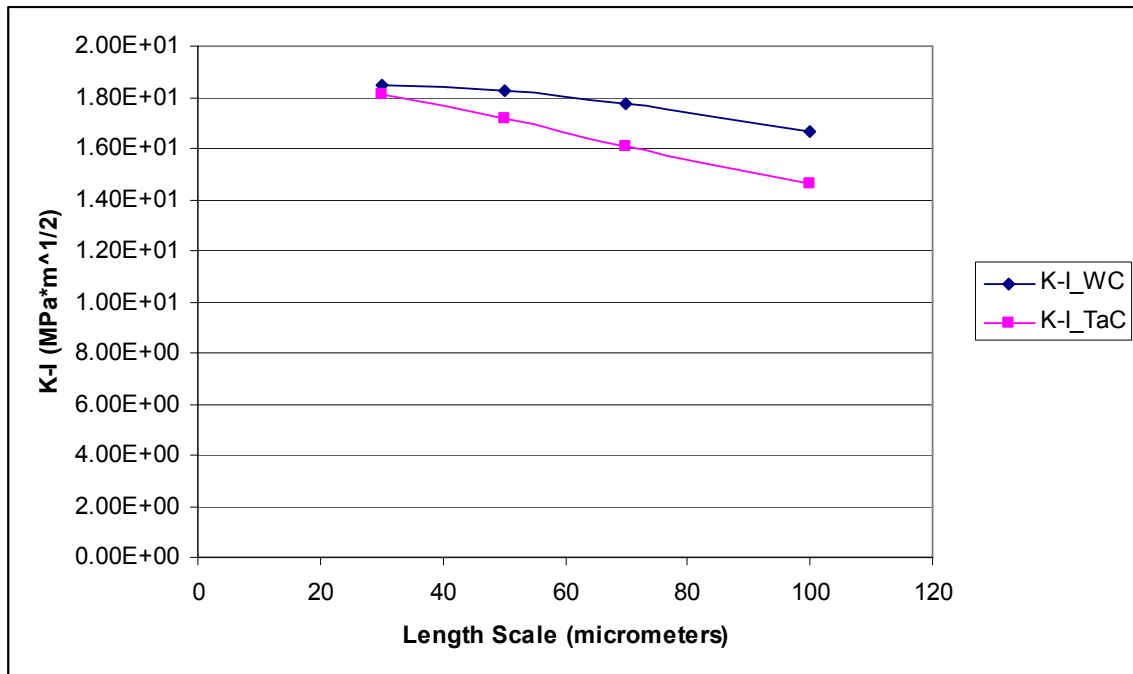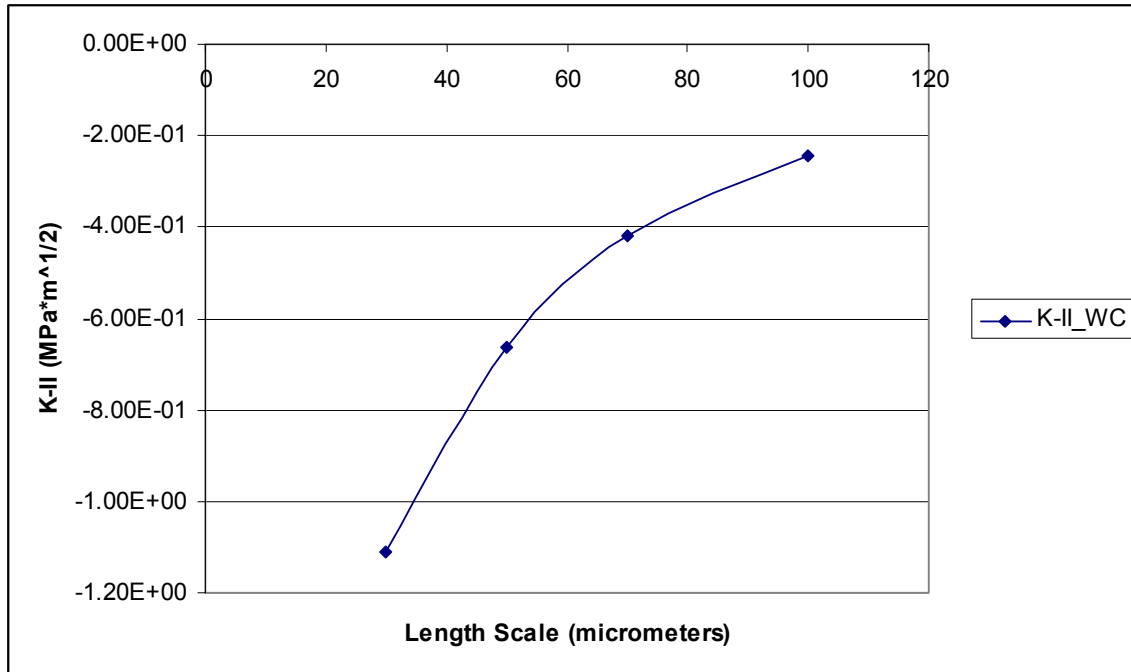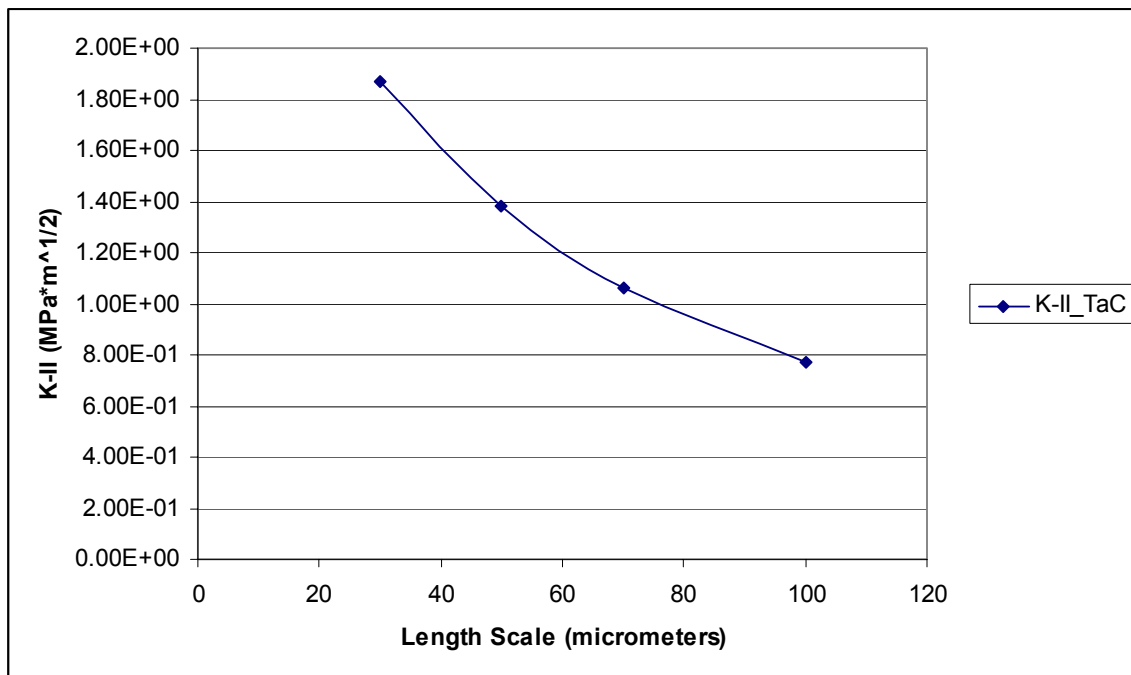

Fig 61: Variation of Mode-I stress intensity factor (K-I) with length scale.

(a)

(b)

Fig 62 (a) Effect of length scale (*l*) on the K-II_WC
(b) Effect of length scale (*l*) on the K-II_TaC

116

As it can be observed from the above graphs, the Mode-I stress intensity factor decreases with increase in length scale. As the length scale is increased, the non-local interactions have increased as a result of which there is a smooth closure at the tip leading to a decrease in K-I with length scale. Analytically, a complex stress intensity factor K^* is employed by Rice [19] and Hutchinson *et al* [20] which include both K-I and K-II.

5.3) Crack Normal to Bi-material Interface and 100 microns away:

The problem of a crack normal to the interface of a structurally non-homogeneous ceramic bi-material is solved and the results for four different meshes as shown in Fig. 40(a)-(d), with mesh 4 being the coarse and mesh1 being the finest, are presented. The structure of the crack tip for four different meshes is shown in the Fig. 40(e). It can be seen that the response is almost independent of the mesh size. The local σ_{22} stress component is plotted along the boundaries AB (see Fig. 39) and CD (see Fig. 39). Figs. 41 and 42 show the Local σ_{22} stress plots on the boundaries CD and AB respectively. The response can be noticed to be almost independent of the mesh. Figs 43 and 44 show the Effective σ_{22} stress plots on the boundaries CD & AB respectively. The response is highly oscillatory near the tip and does not have a particular trend.

The effect of characteristic length scale on the structure of the crack tip and stress is explored. The change in the structure of the crack tip with characteristic length scale is presented in the Fig. 45. It can be observed that the closure at the tip is smoothened as the

length scale is increased. This can be elucidated clearly from the slope change of the structure of the crack tip as shown in Fig. 63.
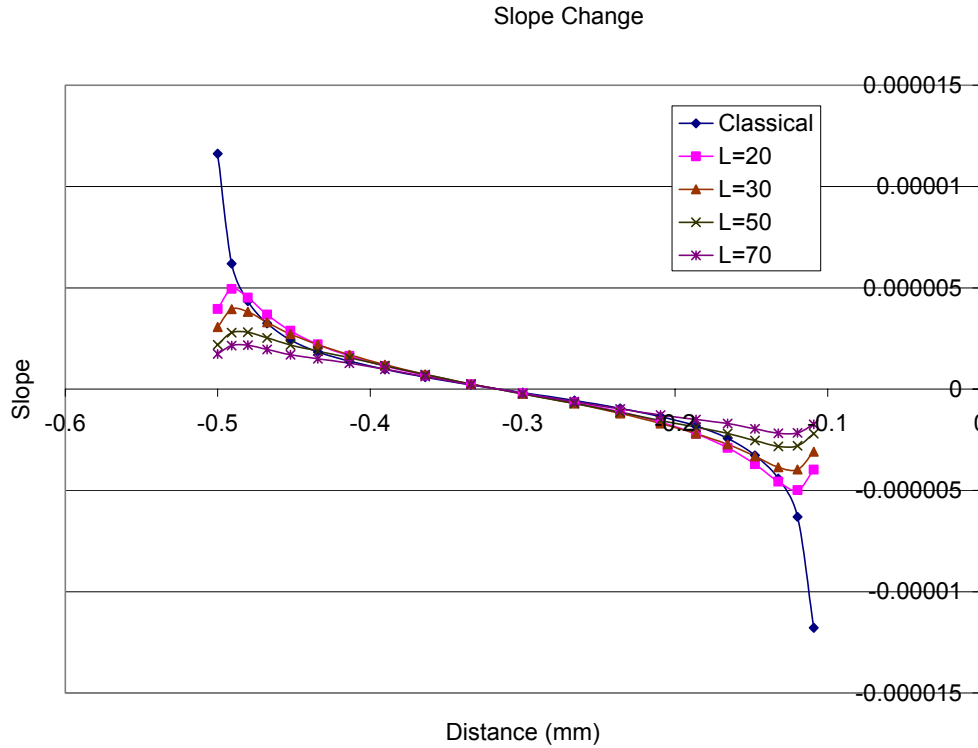
Fig 63: Slope change of the structure of crack

The effect of length scale on the local stress is presented in Figs. 46 and 47 for boundary portions AB and CD (see Fig. 39) respectively. The nature of solution near the crack tip B, which is far away from the bi-material interface, is same as the nature of solution shown by homogeneous case. But the nature of the stress field near the crack tip C which is near the bi-material is entirely different from the homogeneous case. This difference in nature can be attributed to the influence of TaC material on WC material. It can also be observed that the crack tip stress is decreased as the length scale is increased. As it can be seen from the Fig. 47, the heterogeneity in deformation is not entirely captured near the bi-material interface as the element size is in the order of length scale used. The further

refinement of mesh near the bi-material interface could capture the nature of the deformation. Figs. 48 and 49 shows the effect of length scale on effective stress which is highly fluctuating without a particular trend.

Effect of the characteristic length scale on the stress intensity factor:

As the specimen is composed of two different materials, even in Mode-I loading, Mode-II phenomena exists. The Mode-I and Mode-II stress intensity factors are calculated using the equation 5.6.

The effect of length scale on both Mode-I stress intensity factor (K-I) and Mode-II stress intensity factor (K-II) are shown below for both crack tips B and C. The following graph shows the change in K-I with length scale for the both crack tips B and C. (see Fig. 41).
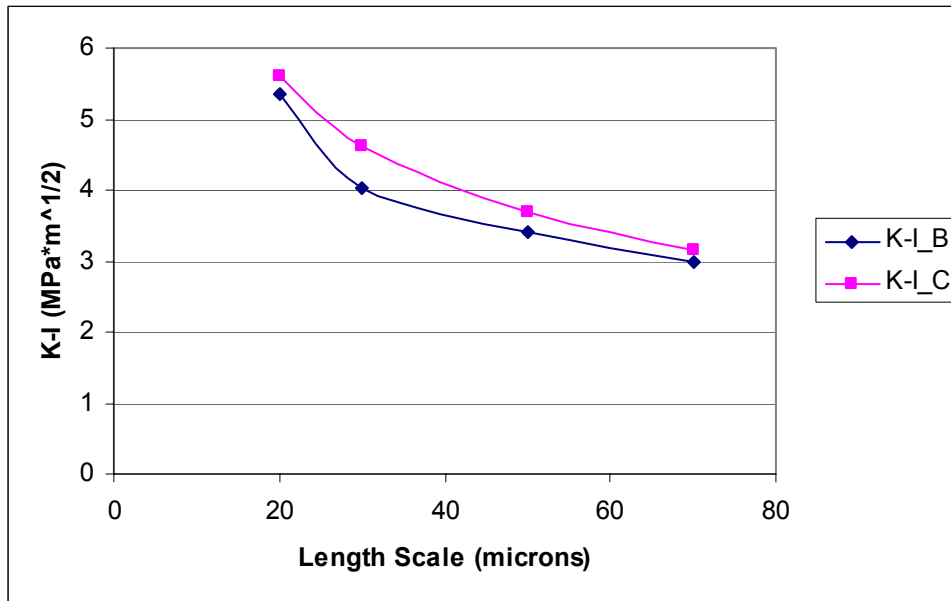
Fig 64: Effect of length scale on K-I for crack tip B and C

It can be observed from the Fig. 64 that the Mode-I stress intensity factor decreases with increase in length scale. Fig. 65 below shows that change in the Mode-II stress intensity factor of the crack tips B and C with the characteristic length scale.
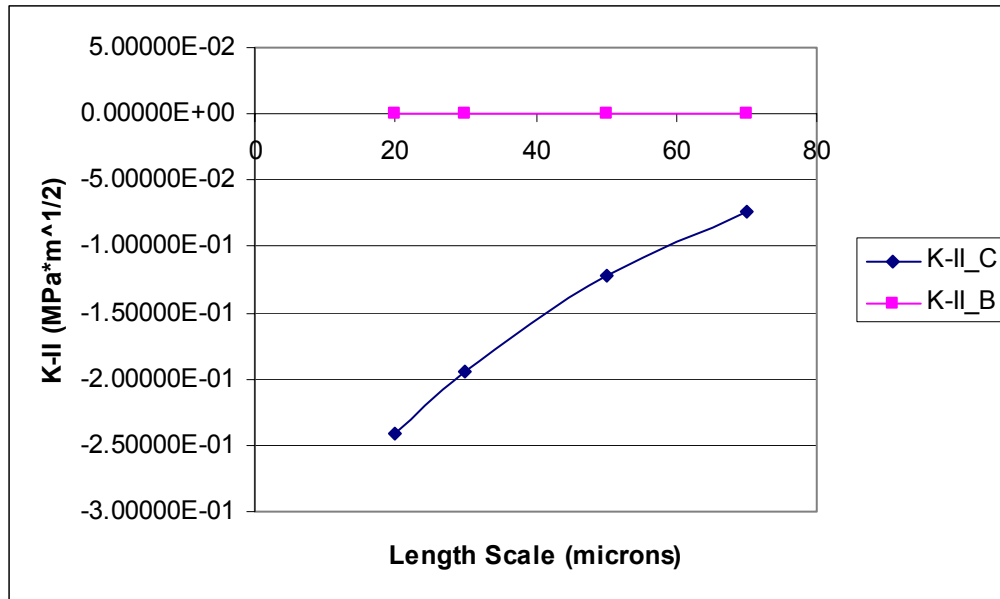
Fig 65: Effect of length scale on K-II for crack tips B and C

It can be seen that K-II for the crack tip B is almost constant with length scale and equal to zero. This behavior of K-II of the crack tip B can be attributed to the fact that it is in the homogeneous region far away from the bi-material interface. The graph shows the Mode-II stress intensity factor (K-II) for the crack tip C (see Fig. 25) increases with increase in length scale.

CHAPTER 6

CONCLUSIONS

The classical solution of stress around the crack tip using linear classical theory of elasticity is singular and the structure of crack tip is closed abruptly at the tip. To capture the heterogeneity of deformation at the tip, Aifantis modified the classical Hooke's law with higher order gradients of strain and proposed gradient elasticity. The theory of gradient elasticity is presented as a special case of Mindlin's first order strain gradient theory and also as derived from gradient enhanced formulations.

A C^1 finite element with 36 degrees of freedom is used to interpolate the displacement field. The results of FE simulation of a crack in homogeneous material, of a bi-material interface crack and of a crack normal to the bi-material interface and 100 micrometers away from it are presented. Mesh sensitivity analysis is demonstrated by presenting the response for different meshes. The effect of characteristic length scale on the nature of the solution is also studied.

Mesh sensitivity analysis results show that the structure of crack tip and local stress are independent of mesh size. Although the effective stress is not converging completely, the nature of the solution is converging. A smooth closure of the structure of the crack tip is achieved which shows that gradient elasticity with an embedded characteristic length scale could to some extent capture the heterogeneity in the deformation around the crack tip. But the theory could not regularize the crack tip stress singularity and it persisted as

before. Although there is crack singularity, the nature of obtained solution is such that it approaches a finite value near the crack tip unlike predicted by classical theory.

For further investigations in the same lines, one can probe into problems such as (a) investigation of stress field when the crack normal to the bi-material interface is moved further away (b) interaction between a bi-material interface crack and a crack parallel to the interface lying in single material (c) interaction between a bi-material interface crack and a void lying in single material (d) investigation of stress field of a crack parallel to the bi-material interface lying in single material when one crack tip rotated about the other away from the interface.

REFERENCES

[1] Barenblatt G.I, " The Mathematical theory of equilibrium cracks in brittle materials", *Advanced Applied Mechanics , 7, 55,1962.*

[2] Goodier, J.N and Kanninen, M, "Crack Propagation in a continuum model with non-linear atomic separation laws", *Technical Report No 165, Division of Engineering Mechanics , Stanford University*, 1966.

[3] Gehlen, P.C and Kanninen, M.F, "Inelastic Behavior of Solids", *(edited by Kanninen, M. F., Adler, W.F., Rosenfield, A. R. and Jaffe, R. I.), p. 587. McGraw-Hill, New York*, 1969.

[4] Weiner, J, H. and Sanders, W. T., *Phys. Rev.*134, A1007-1015, 1964.

[5] Eringen A. C. and Edelen D.G.B, "On Non-Local Elasticity", *Int. J. Engng. sci., Vol. 10, pp. 233-248, 1972.*

[6] Kroner, "Mechanics of Generalized Continua" , *IUTAM Symposium Freudenstadt. Stuttgart 1967.*

[7] Cosserat, E. et F., "Theorie des Corps Deformables", *Paris: A. Hermann & Fils 1909.*

[8] Sternberg and Muki., "The effect of couple-stresses on the stress concentration around a crack", *Int. J. Solids Struct., Vol 3, pp. 69-95, 1967*

[9] Mindlin R. D., "Microstructure in Linear Elasticity" *Arc. Rat. Mech. Anal.* 16. pp. 51-78, 1964.

[10] Mindlin R. D. and Eshel N. N., "On first strain-gradient theories in linear elasticity", *Int. J. Solids Struct., Vol 4, Issue 1, Pages 109-124, 1968.*

[11]

   (a) Altan, B and Aifantis E. C., " On the structure of the mode III crack tip in gradient elasticity", *Scripta Met*. 26, 319, 1992.

   (b) Ru, C. Q. and Aifantis, E. C., " A simple approach to solve boundary-value problems in gradient elasticity", *Acta. Mech.*, 101, 59, 1993.

   (c) Exadaktylos G. E. and Aifantis E. C., " Two and Three Dimensional Crack Problems in Gradient Elasticity" , *Journal of the Mechanical Behavior of Materials,* 7, No. 2, 1996.

[12] Toupin R. A. and Gazis D. C., " Surface effects and initial stress in continuum and lattice models of elastic crystals", *Lattice Dynamics , Proceedings of an international conference, edited by R.F.Wallis.*

[13] Dasgupta S. and Sengupta D., "A Higher-order triangular plate bending element revisted", *Int. J. Num. Meth. Engng.* 30, 419-430, 1990.

[14] Peerlings, R.H.J., de Borst, R., Brekelmans, W.A.M., de Vree, J.H.P., "Gradient enhanced damage for quasi-brittle materials", *Int. J. Numer. Meth. Eng.* 17, 3391–3403 1996.

[15] Eisenberg, M. A. and Malvern, L. E., "On finite element integration in natural coordinates" , *Int. J. Num. Meth. Eng.,* 7, 574 1973.

[16] Dundurs, J., "Effect of Elastic Constants on Stress in a Composite under Plane Deformation," *Journal of Composite Materials*, **1**, pp. 310-322 1967.

[17] Williams M. L., "The stresses around a fault or crack in dissimilar media*", Bull. Seismological Soc. America* 49, 199-204 1959.

[18] Erdogan F., "Stress distribution in a non-homogeneous elastic plane with cracks", *J. Appl. Mech.* 30, 232-237, 1963.

[19] Rice J., "Elastic fracture mechanics concepts for interfacial cracks", *J. Appl. Mech., vol 55, pp 98-103, 1988.*

[20] Hutchinson J. W., Mear M. and Rice J. R., "Crack paralleling the interface between dissimilar materials", *J. Appl. Mech .,vol 54, pp 828-832, 1987.*

[21] Zienkiewicz O. C. and Taylor R.L. " The Finite Element Method: Solid and Fluid Mechanics Dynamics and Non-Linearity" ,*Mc Graw-Hill International Editions, Fourth Edition ,vol 2, Pg.23.*

[22] Reddy J. N., "An Introduction to the Finite Element Method", *Mc Graw-Hill International Editions, Second Edition-1993, Pg.515.*

[23] Zienkiewicz O. C. and Taylor R.L. " The Finite Element Method: Solid and Fluid Mechanics Dynamics and Non-Linearity" ,*Mc Graw-Hill International Editions, Fourth Edition ,vol 2, Pg.14.*

[24] A. Zervos, P. Papanastasiou and I. Vardoulakis, "A Finite element displacement formulation for gradient elastoplasticity", *Int. J. Numer. Meth. Engng, vol 50,pp 1369-1388 ,2001.*

APPENDIX

The shape functions of the element used are

$$N_1 = L_1^5 + 5L_1^4L_2 + 5L_1^4L_3 + 10L_1^3L_2^2 + 10L_1^3L_3^2 + 20L_1^3L_2L_3 + 30r_{21}L_1^2L_2L_3^2 + 30r_{31}L_1^2L_3L_2^2$$

$$N_2 = c_3L_1^4L_2 - c_2L_1^4L_3 + 4c_3L_1^3L_2^2 - 4c_2L_1^3L_3^2 + 4(c_3 - c_2)L_1^3L_2L_3 - (3c_1 + 15r_{21}c_2)L_1^2L_2L_3^2$$
$$+ (3c_1 + 15r_{31}c_3)L_1^2L_3L_2^2$$

$$N_3 = -b_3L_1^4L_2 + b_2L_1^4L_3 - 4b_3L_1^3L_2^2 + 4b_2L_1^3L_3^2 + 4(b_2 - b_3)L_1^3L_2L_3 + (3b_1 + 15r_{21}b_2)L_1^2L_2L_3^2$$
$$- (3b_1 + 15r_{31}b_3)L_1^2L_3L_2^2$$

$$N_4 = \frac{c_3^2}{2}L_1^3L_2^2 + \frac{c_2^2}{2}L_1^3L_3^2 - c_2c_3L_1^3L_2L_3 + \left(c_1c_2 + \frac{5}{2}r_{21}c_2^2\right)L_2L_3^2L_1^2 + \left(c_1c_3 + \frac{5}{2}r_{31}c_3^2\right)L_3L_2^2L_1^2$$

$$N_5 = -b_3c_3L_1^3L_2^2 - b_2c_2L_1^3L_3^2 + (b_2c_3 + b_3c_2)L_1^3L_2L_3 - (b_1c_2 + b_2c_1 + 5r_{21}b_2c_2)L_2L_3^2L_1^2$$
$$- (b_1c_3 + b_3c_1 + 5r_{31}b_3c_3)L_3L_2^2L_1^2$$

$$N_6 = \frac{b_3^2}{2}L_1^3L_2^2 + \frac{b_2^2}{2}L_1^3L_3^2 - b_2b_3L_1^3L_2L_3 + \left(b_1b_2 + \frac{5}{2}r_{21}b_2^2\right)L_2L_3^2L_1^2 + \left(b_1b_3 + \frac{5}{2}r_{31}b_3^2\right)L_3L_2^2L_1^2$$

where,

$$b_i = y_j - y_k$$
$$c_i = x_k - x_j$$

with i, j, k being cyclic permutations of 1,2 and 3.

$$r_{ij} = -\frac{b_ib_j + c_ic_j}{b_i^2 + c_i^2}$$

The remaining twelve components of the shape function, N_7 to N_{18}, corresponding to the degrees of freedom at nodes 2 and 3 are obtained by the cyclic permutations of the suffixes.